University of Rhode Island
DigitalCommons@URI

Open Access Master's Theses

2015

Mechanics Framework of Pad Scratching in Chemical-Mechanical Planarization

David C. Ponte
University of Rhode Island, dcp1191@verizon.net

Follow this and additional works at: https://digitalcommons.uri.edu/theses

Terms of Use
All rights reserved under copyright.

Recommended Citation
Ponte, David C., "Mechanics Framework of Pad Scratching in Chemical-Mechanical Planarization" (2015). *Open Access Master's Theses.* Paper 676.
https://digitalcommons.uri.edu/theses/676

This Thesis is brought to you by the University of Rhode Island. It has been accepted for inclusion in Open Access Master's Theses by an authorized administrator of DigitalCommons@URI. For more information, please contact digitalcommons-group@uri.edu. For permission to reuse copyrighted content, contact the author directly.

MECHANICS FRAMEWORK OF PAD SCRATCHING IN CHEMICAL-MECHANICAL PLANARIZATION

BY

DAVID C. PONTE

A THESIS SUBMITTED IN PARTIAL FULFILLMENT OF THE

REQUIREMENTS FOR THE DEGREE OF

MASTER OF SCIENCE

IN

MECHANICAL ENGINEERING AND APPLIED MECHANICS

UNIVERSITY OF RHODE ISLAND

2015

MASTER OF SCIENCE THESIS

OF

DAVID C. PONTE

APPROVED:

Thesis Committee:

Major Professor DML Meyer

Arun Shukla

Godi Fischer

Nasser H. Zawia
DEAN OF THE GRADUATE SCHOOL

UNIVERSITY OF RHODE ISLAND
2015

ABSTRACT

Chemical-Mechanical Planarization (CMP) is a crucial intermediate process in integrated circuit (IC) fabrication. As the average IC feature size decreases each year, scratches produced on wafers from polishing pads during CMP have become a prominent issue. These scratches can be much larger than features on the circuits, which results in an increase of damaged and discarded wafers after CMP. To determine the mechanisms of CMP pad scratching, an analytical model based in thermomechanics was constructed. This model accounted for potential sources of energy dissipation, which are important in properly understanding and accounting for processes which produce damage on the wafer. Multiple forms of energy dissipation were investigated through experimental analyses that include strain energies, energy flux through material removal, and internal energy dissipation. Mechanical characterization of CMP pad material and planarization experiments were performed.

Porous polyurethane polishing pad material was mechanically characterized in compression and in tension to properly model its constitutive behavior during CMP. Stress relaxation experiments of the pad material in compression were performed to construct a stress relaxation model. The results showed that viscoelastic strain energy is significant in CMP processes. Additionally, the polishing pad relaxation behavior varied depending on whether the pad was loaded in tension or compression. The viscoelastic relaxation rate of the pad material increased after being soaked in distilled water and CMP slurry. This result suggests pad scratching can be reduced with proper soaking of the pad material. Measurements of pad compressibility were also performed by optically

tracking pad samples which were under compressive stresses. This analysis quantified the significance of the pad material's compressibility with regard to its internal stresses.

Planarization experiments were performed to gather experimental information on mechanical and topographical changes of the pad and wafer materials through the CMP process. Generally, the coefficient of friction between the pad and wafer material decreased with increasing polishing time. From the constructed contact stress analysis, a smaller coefficient of friction resulted in the reduction of von Mises stress in the wafer material. The surface of a polishing pad became smoother with increasing polishing time. Experimental planarization results showed that roughness of the pad surface may have an influence on the coefficient of friction, while both of these variables relate to the scratching ability of the pad material. Plastic smoothing of the pad surface also indicated that the plastic strain energy dissipated into the pad material is important for the CMP thermomechanical model.

Differential scanning calorimetry (DSC) of worn pad material was conducted to observe potential energy dissipation into the pad's polymer structure during planarization. Polishing pad calorimetry results showed a measurable increase in the computed enthalpies of reaction of pad samples with an increase in the number of wafers polished. These results suggest energy is dissipated into the pad's material structure during CMP and may have an influence on scratch production.

ACKNOWLEDGMENTS

I would like to thank my advisor, Prof. D.M.L. Meyer, who has provided me with an incredible amount of guidance throughout my undergraduate career and through the completion of this current body of work. She has taught me valuable skills that I will carry with me throughout my engineering career. I would like to thank my laboratory colleagues Greg Turner, Jim Byrnes, Joe Gomez, and David Ferreria for their time spent working with me and their invaluable advice in resolving various issues throughout the course of this project. I would like to thank Prof. Carl-Ernst Rousseau and Dr. Jahn Torres for lending equipment that was utilized in the completion of this work. I would also like to thank Prof. Geoffrey Bothun and Prof. Michael Greenfield for their expert advice in an unfamiliar topic. Special thanks to the igus® Young Engineers Support Program for the donation of equipment used to conduct experiments essential for this project. I would also like to thank the University of Rhode Island Mechanical Engineering department and its department chair Prof. David Taggart for the financial support that allowed me to complete my master's degree.

Finally, I would like to thank my family and friends for supporting and encouraging me throughout the course of obtaining my bachelor's and master's degrees.

TABLE OF CONTENTS

ABSTRACT ii

ACKNOWLEDGMENTS iv

TABLE OF CONTENTS v

LIST OF TABLES vii

LIST OF FIGURES xii

INTRODUCTION 1

1.1 Integrated Circuit Fabrication 1

1.2 Chemical-Mechanical Planarization 4

1.3 Wafer Damage from Chemical-Mechanical Planarization 6

REVIEW OF LITERATURE 9

2.1 Selection of CMP for Integrated Circuit Fabrication 9

2.2 General Mechanical Modeling of CMP 13

2.3 CMP Scratching by Abrasive Particles and Wear Debris 17

2.4 CMP Scratching by Pad Asperities 21

METHODOLOGY 27

3.1 Thermomechanical Modeling of Wafer Damage 28

3.2 CMP Stress Analysis 35

3.2.1 Wafer Material Constitutive Modeling 36

3.2.2 Polishing Pad Constitutive Modeling 39

3.2.2.1 IC1000 Pad Compressive Stress Relaxation 42

3.2.2.1 IC1000 Pad Compressibility 49

3.2.2.2 Tensile Characterization of IC1000 Pad 56

3.2.3 Contact Stresses in Scratch Generation 60

3.3 Chemical-Mechanical Planarization Experiments 62

3.3.1 Planarization Experiments 63

3.3.1.1 Dimensional Analysis 68

3.3.1.2 Experimental Procedure 80

3.3.2 CMP Material Topographical Evolution 82
3.3.3 Polishing Pad Differential Scanning Calorimetry 84

FINDINGS 91

4.1 Results of Polishing Pad Constitutive Modeling 91
4.1.1 Compressive Stress Relaxation Experiments 91
4.1.1.1 Polishing Pad Compressive Relaxation with Soaking 95
4.1.1.2 Polishing Pad Compressive Relaxation with Stress Magnitude 111
4.1.2 IC1000 Pad Compressibility Results 117
4.1.3 IC1000 Pad Tensile Stress Relaxation Results 125
4.1.4 Quasi-static Tensile Testing of IC1000 Pad Material 132
4.2 Pad and Wafer Contact Stress Analysis 133
4.3 Chemical-Mechanical Planarization Experimental Results 140
4.3.1 Planarization Experimental Results 142
4.3.1.1 Forces of Contact 145
4.3.1.2 Topographical CMP Surface Evolution 154
4.3.1.3 Energy of Material Removal 163
4.3.1.4 Differential Scanning Calorimetry of IC1000 Pad Material 170
4.3.1.1 Dimensional Analysis of CMP Planarization Results 186

CONCLUSIONS 188

5.1 Conclusions 188
5.2 Future Work 192

APPENDICES 196

6.1 MATLAB Code for Strain and Stress Analysis of Compression Relaxation .. 196
6.2 MATLAB Code for Compressibility Measurements of the IC1000 Pad 198
6.3 Differential Scanning Calorimetry Thermograms of IC1000 Pad Samples 202

BIBLIOGRAPHY 205

LIST OF TABLES

Figure 1: Multilevel Interconnect Cross Section (Li 2008, 734) 2

Figure 2: Intel Wafer with 45 nm Feature Size Chips (Intel 2006) 3

Figure 3: Typical Chemical-Mechanical Planarization Setup 5

Figure 4: Wafer Cross Section after Metal Deposition....................11

Figure 5: Layer Representation of an IC Fabricated without Planarization (Li 2008, 734)....................11

Figure 6: Levels of IC Planarization (Li 2008, 734)....................12

Figure 7: Dual Damascene Process 13

Figure 8: Material Removal Process (Bastaninejad and Ahmadi 2005, G720-G730) 16

Figure 9: Abrasive Slurry Particle Polishing a Wafer Surface (Saka, Eusner, and Chun 2008, 341-344) 19

Figure 10: Scratches Produced from Pad Asperities during CMP (Kim et al. 2013, 307-310) 22

Figure 11: IC1000 Polishing Pad Surface....................42

Figure 12: Compression Test Setup....................45

Figure 13: Example Image of Block Edges. 47

Figure 14: Grayscale Image of Pad Sample before Compression....................51

Figure 15: Binary Image of Isolated Pad Sample with Linear Regression for Rotation....................51

Figure 16: Rotated Binary Images of Pad Sample. Left: Uncompressed. Right: Fully Compressed.......53

Figure 17: Pad Sample for Compressibility....................54

Figure 18: Load versus Crosshead Extension for Tensile Compliance Testing....................57

Figure 19: Tensile Experimental Setup for the IC1000 Pad 59

Figure 20: Evolution of Pad Asperity and Wafer Contact 61

Figure 21: Reciprocating Linear Tribometer 64

Figure 22: Polishing Pad Tribometer Fixture 65

Figure 23: Arc Length of Pad and Wafer Contact through a Single Rotation 71

Figure 24: Mahr Federal Perthometer....................83

Figure 25: Differential Scanning Calorimetry Heating Cell 85

Figure 26: Percent Change in Block Edge Displacement with Time....................95

Figure 27: Normalized Stress Relaxation of Pad Material in Compression at 4 psi 99

Figure 28: Reduced Trials of Normalized Stress Relaxation of Pad Material in Compression at 4 psi...99

Figure 29: Normalized Stress Relaxation of Pad Material in Compression with Logarithmic Scale of t/t_o + 1 at 4 psi 101

Figure 30: Reduced Trials of Normalized Stress Relaxation of Pad Material in Compression with Logarithmic Scale of t/t_o + 1 at 4 psi 102

Figure 31: Short Time Compressive Relaxation Curve Fitting of Pad Material at 4 psi 106

Figure 32: Long Time Compressive Relaxation Curve Fitting of Pad Material at 4 psi 106

Figure 33: Full Time Compressive Relaxation Curve Fitting of Pad Material at 4 psi 107

Figure 34: Normalized Stress Relaxation of Pad Material in Compression at a Range of Initial Stresses 112

Figure 35: Normalized Stress Relaxation of Pad Material in Compression with Logarithmic Scale of t/t_o + 1 at a Range of Initial Stresses 112

Figure 36: Short Time Compressive Relaxation Curve Fitting of Pad Material at a Range of Initial Stresses 115

Figure 37: Long Time Compressive Relaxation Curve Fitting of Pad Material at a Range of Initial Stresses 115

Figure 38: Full Time Compressive Relaxation Curve Fitting of Pad Material at a Range of Initial Stresses 116

Figure 39: Compression of Pad Sample (Trial 5) 119

Figure 40: IC1000 Jacobian versus Axial Compressive Strain Data and its Linear Regression (Trial 5) 119

Figure 41: Transverse Strain versus Axial Strain Linear Regression for the IC1000 Pad Poisson's Ratio (Trial 5)....................122

Figure 42: Unit Volume Change of an IC1000 Pad Sample (Trial 5) 124

Figure 43: Average Stress Relaxation of IC1000 Pad in Tension over Time 126

Figure 44: Normalized Stress Relaxation of IC1000 Pad in Tension with Time 127

Figure 45: Normalized Stress Relaxation of IC1000 Pad in Tension with Logarithmic Scale of $t/t_o + 1$ 127

Figure 46: Instron Testing Machine Overshoot of the Set Held Strain..128

Figure 47: Regression Model of Tensile Stress Relaxation of IC1000 Pad Material. 130

Figure 48: Quasi-static Tensile Test of IC1000 Pad 132

Figure 49: Pad and Wafer Contact Geometry and Coordinate System 134

Figure 50: F_z and F_x with Travel Time for Copper Wafer and Pad Planarization Experiments 146

Figure 51: F_z and F_x with Travel Time for Silicon Dioxide Wafer and Pad Planarization Experiments 146

Figure 52: Coefficient of Friction and Average Pad Roughness with Time Traveled for Pad on Copper Wafer Experiments. Top: CLL (Copper, Low Pressure, Low Velocity), CHL (Copper, High Pressure, Low Velocity). Bottom: CLH (Copper, Low Pressure, High Velocity), CHH (Copper, High Pressure, High Velocity). 148

Figure 53: Coefficient of Friction and Average Pad Roughness with Time Traveled for Pad on Silicon Dioxide Wafer Experiments. Top: SLL (SiO_2, Low Pressure, Low Velocity), SHL (SiO_2, High Pressure, Low Velocity). Bottom: SLH (SiO_2, Low Pressure, High Velocity), SHH (SiO_2, High Pressure, High Velocity). 149

Figure 54: Coefficient of Friction versus Distance Traveled. Top: Copper and Pad Wafer Trials. Bottom: Silicon Dioxide and Pad Wafer Trials. 153

Figure 55: Copper Plate with Wear Tracks after High Pressure and High Velocity Planarization 155

Figure 56: Friction Force of a Planarization Experiment through Two Complete Cycles 155

Figure 57: Pad Sample Surfaces from Planarization Experiments 157

Figure 58: Average Surface Roughness of Pad Samples 158

Figure 59: Root Mean Squared Roughness of Pad Samples 158

Figure 60: Wafer Surface Average Roughness from Before and After Planarization 160

Figure 61: Wafer Surface Root Mean Squared Roughness from Before and After Planarization 160

Figure 62: Average Waviness of Wafer Surfaces Perpendicular to Direction of Travel 162

Figure 63: Waviness Profile Perpendicular to Travel Direction from Silicon Dioxide at Low Pressure and High Velocity (SLH), After Planarization 163

Figure 64: Wear Track Geometry for Material Removal Analysis...165

Figure 65: Differential Scanning Calorimetry Thermogram of a New Pad Sample (Trial 3)................172

Figure 66: Calorimetry Results from New Pad Samples 175

Figure 67: Calorimetry Results from Copper Wafer, High Pressure, High Velocity Pad Samples with New Pad Results of Trial 1 175

Figure 68: Calorimetry Results from Silicon Dioxide Wafer, High Pressure, High Velocity Pad Samples with New Pad Results of Trial 1 176

Figure 69: Specific Heat with Wafer Count at 65°C. Top: First Heating. Bottom: Second Heating. 178

Figure 70: Specific Heat with Wafer Count at 220°C. Top: First Heating. Bottom: Second Heating. ..179

Figure 71: Cooling of Pad Sample from Copper Wafer, High Pressure, High Velocity Pad at 100 Wafer Count 182

Figure 72: Calorimetry Results of IC1000 Pad Samples to 400°C 183

Figure 73: Specific Enthalpy of Reaction from IC1000 Pad Irreversible Reactions 185

Figure 74: Planarization Experiment Pi Group..187

Figure 75: Calorimetry Results from Copper Wafer, High Pressure, Low Velocity Pad Samples with New Pad Results of Trial 1 202

Figure 76: Calorimetry Results from Copper Wafer, Low Pressure, High Velocity Pad Samples with New Pad Results of Trial 1 202

Figure 77: Calorimetry Results from Copper Wafer, Low Pressure, Low Velocity Pad Samples with New Pad Results of Trial 1 203

Figure 78: Calorimetry Results from Silicon Dioxide Wafer, High Pressure, Low Velocity Pad Samples with New Pad Results of Trial 1 203

Figure 79: Calorimetry Results from Silicon Dioxide Wafer, Low Pressure, High Velocity Pad Samples with New Pad Results of Trial 1 204

Figure 80: Calorimetry Results from Silicon Dioxide Wafer, Low Pressure, Low Velocity Pad Samples with New Pad Results of Trial 1 204

LIST OF FIGURES

Figure 1: Multilevel Interconnect Cross Section (Li 2008, 734) 2

Figure 2: Intel Wafer with 45 nm Feature Size Chips (Intel 2006) 3

Figure 3: Typical Chemical-Mechanical Planarization Setup 5

Figure 4: Wafer Cross Section after Metal Deposition....11

Figure 5: Layer Representation of an IC Fabricated without Planarization (Li 2008, 734)....11

Figure 6: Levels of IC Planarization (Li 2008, 734)....12

Figure 7: Dual Damascene Process 13

Figure 8: Material Removal Process (Bastaninejad and Ahmadi 2005, G720-G730) 16

Figure 9: Abrasive Slurry Particle Polishing a Wafer Surface (Saka, Eusner, and Chun 2008, 341-344) 19

Figure 10: Scratches Produced from Pad Asperities during CMP (Kim et al. 2013, 307-310) 22

Figure 11: IC1000 Polishing Pad Surface....42

Figure 12: Compression Test Setup....45

Figure 13: Example Image of Block Edges. 47

Figure 14: Grayscale Image of Pad Sample before Compression....51

Figure 15: Binary Image of Isolated Pad Sample with Linear Regression for Rotation....51

Figure 16: Rotated Binary Images of Pad Sample. Left: Uncompressed. Right: Fully Compressed. 53

Figure 17: Pad Sample for Compressibility....54

Figure 18: Load versus Crosshead Extension for Tensile Compliance Testing....57

Figure 19: Tensile Experimental Setup for the IC1000 Pad 59

Figure 20: Evolution of Pad Asperity and Wafer Contact 61

Figure 21: Reciprocating Linear Tribometer 64

Figure 22: Polishing Pad Tribometer Fixture 65

Figure 23: Arc Length of Pad and Wafer Contact through a Single Rotation 71

Figure 24: Mahr Federal Perthometer....83

Figure 25: Differential Scanning Calorimetry Heating Cell 85

Figure 26: Percent Change in Block Edge Displacement with Time....95

Figure 27: Normalized Stress Relaxation of Pad Material in Compression at 4 psi 99

Figure 28: Reduced Trials of Normalized Stress Relaxation of Pad Material in Compression at 4 psi...99

Figure 29: Normalized Stress Relaxation of Pad Material in Compression with Logarithmic Scale of $t/t_o + 1$ at 4 psi 101

Figure 30: Reduced Trials of Normalized Stress Relaxation of Pad Material in Compression with Logarithmic Scale of $t/t_o + 1$ at 4 psi 102

Figure 31: Short Time Compressive Relaxation Curve Fitting of Pad Material at 4 psi 106

Figure 32: Long Time Compressive Relaxation Curve Fitting of Pad Material at 4 psi 106

Figure 33: Full Time Compressive Relaxation Curve Fitting of Pad Material at 4 psi 107

Figure 34: Normalized Stress Relaxation of Pad Material in Compression at a Range of Initial Stresses 112

Figure 35: Normalized Stress Relaxation of Pad Material in Compression with Logarithmic Scale of $t/t_o + 1$ at a Range of Initial Stresses 112

Figure 36: Short Time Compressive Relaxation Curve Fitting of Pad Material at a Range of Initial Stresses 115

Figure 37: Long Time Compressive Relaxation Curve Fitting of Pad Material at a Range of Initial Stresses 115

Figure 38: Full Time Compressive Relaxation Curve Fitting of Pad Material at a Range of Initial Stresses 116

Figure 39: Compression of Pad Sample (Trial 5) 119

Figure 40: IC1000 Jacobian versus Axial Compressive Strain Data and its Linear Regression (Trial 5) 119

Figure 41: Transverse Strain versus Axial Strain Linear Regression for the IC1000 Pad Poisson's Ratio (Trial 5)....122

Figure 42: Unit Volume Change of an IC1000 Pad Sample (Trial 5) 124

Figure 43: Average Stress Relaxation of IC1000 Pad in Tension over Time 126

Figure 44: Normalized Stress Relaxation of IC1000 Pad in Tension with Time 127

Figure 45: Normalized Stress Relaxation of IC1000 Pad in Tension with Logarithmic Scale of $t/t_o + 1$ 127

Figure 46: Instron Testing Machine Overshoot of the Set Held Strain... 128

Figure 47: Regression Model of Tensile Stress Relaxation of IC1000 Pad Material. 130

Figure 48: Quasi-static Tensile Test of IC1000 Pad 132

Figure 49: Pad and Wafer Contact Geometry and Coordinate System 134

Figure 50: F_z and F_x with Travel Time for Copper Wafer and Pad Planarization Experiments 146

Figure 51: F_z and F_x with Travel Time for Silicon Dioxide Wafer and Pad Planarization Experiments 146

Figure 52: Coefficient of Friction and Average Pad Roughness with Time Traveled for Pad on Copper Wafer Experiments. Top: CLL (Copper, Low Pressure, Low Velocity), CHL (Copper, High Pressure, Low Velocity). Bottom: CLH (Copper, Low Pressure, High Velocity), CHH (Copper, High Pressure, High Velocity). 148

Figure 53: Coefficient of Friction and Average Pad Roughness with Time Traveled for Pad on Silicon Dioxide Wafer Experiments. Top: SLL (SiO_2, Low Pressure, Low Velocity), SHL (SiO_2, High Pressure, Low Velocity). Bottom: SLH (SiO_2, Low Pressure, High Velocity), SHH (SiO_2, High Pressure, High Velocity). 149

Figure 54: Coefficient of Friction versus Distance Traveled. Top: Copper and Pad Wafer Trials. Bottom: Silicon Dioxide and Pad Wafer Trials. 153

Figure 55: Copper Plate with Wear Tracks after High Pressure and High Velocity Planarization........ 155

Figure 56: Friction Force of a Planarization Experiment through Two Complete Cycles 155

Figure 57: Pad Sample Surfaces from Planarization Experiments 157

Figure 58: Average Surface Roughness of Pad Samples 158

Figure 59: Root Mean Squared Roughness of Pad Samples 158

Figure 60: Wafer Surface Average Roughness from Before and After Planarization 160

Figure 61: Wafer Surface Root Mean Squared Roughness from Before and After Planarization 160

Figure 62: Average Waviness of Wafer Surfaces Perpendicular to Direction of Travel 162

Figure 63: Waviness Profile Perpendicular to Travel Direction from Silicon Dioxide at Low Pressure and High Velocity (SLH), After Planarization 163

Figure 64: Wear Track Geometry for Material Removal Analysis...165

Figure 65: Differential Scanning Calorimetry Thermogram of a New Pad Sample (Trial 3)................172

Figure 66: Calorimetry Results from New Pad Samples 175

Figure 67: Calorimetry Results from Copper Wafer, High Pressure, High Velocity Pad Samples with New Pad Results of Trial 1 175

Figure 68: Calorimetry Results from Silicon Dioxide Wafer, High Pressure, High Velocity Pad Samples with New Pad Results of Trial 1 176

Figure 69: Specific Heat with Wafer Count at 65°C. Top: First Heating. Bottom: Second Heating. 178

Figure 70: Specific Heat with Wafer Count at 220°C. Top: First Heating. Bottom: Second Heating. ..179

Figure 71: Cooling of Pad Sample from Copper Wafer, High Pressure, High Velocity Pad at 100 Wafer Count 182

Figure 72: Calorimetry Results of IC1000 Pad Samples to 400°C...183

Figure 73: Specific Enthalpy of Reaction from IC1000 Pad Irreversible Reactions 185

Figure 74: Planarization Experiment Pi Group...187

Figure 75: Calorimetry Results from Copper Wafer, High Pressure, Low Velocity Pad Samples with New Pad Results of Trial 1 202

Figure 76: Calorimetry Results from Copper Wafer, Low Pressure, High Velocity Pad Samples with New Pad Results of Trial 1 202

Figure 77: Calorimetry Results from Copper Wafer, Low Pressure, Low Velocity Pad Samples with New Pad Results of Trial 1 203

Figure 78: Calorimetry Results from Silicon Dioxide Wafer, High Pressure, Low Velocity Pad Samples with New Pad Results of Trial 1 203

Figure 79: Calorimetry Results from Silicon Dioxide Wafer, Low Pressure, High Velocity Pad Samples with New Pad Results of Trial 1 204

Figure 80: Calorimetry Results from Silicon Dioxide Wafer, Low Pressure, Low Velocity Pad Samples with New Pad Results of Trial 1 204

CHAPTER 1

INTRODUCTION

Chemical-mechanical planarization (CMP) is a necessary step in the fabrication of state-of-the-art integrated circuits (ICs). With a process that requires accuracy and precision down to the nanoscale, CMP does not come without its issues. It has only recently been discovered that an unexpected source of IC wafer defects can result from polishing (Eusner, Saka, and Chun 2010). Relatively soft polishing pads can induce scratches on harder wafers that are large enough to greatly reduce manufacturing yields. A mechanical and thermodynamic understanding of polishing pad scratching is required to recognize the origins of defect production.

1.1 Integrated Circuit Fabrication

Integrated circuits (ICs) are the central part of nearly all electronic devices manufactured today. These circuits function as the computing centers of smartphones, computers, and nearly all other digital instruments. Fundamentally, ICs are patterned layers of conducting and insulating materials deposited onto a semiconducting wafer (Yanda, Heynes, and Miller 2005). Built onto the semiconducting material are millions of discrete electrical components such as transistors, resistors and capacitors. The electrical components are wired together into the desired circuit with layers of patterned conducting and insulating materials. The result is a complex electrical circuit in which

all of its components are integrated into a single package. Figure 1 shows a scanning electron microscope (SEM) image of an integrated circuit cross section, where the metal is shown lighter in color among the darker-colored dielectric layers. With the most complex ICs in current production, an integrated circuit consists of over a billion electrical components in a single chip (Mack 2011, 202-207). Such circuits allow for the high computing power of today's electronic devices in small packages.

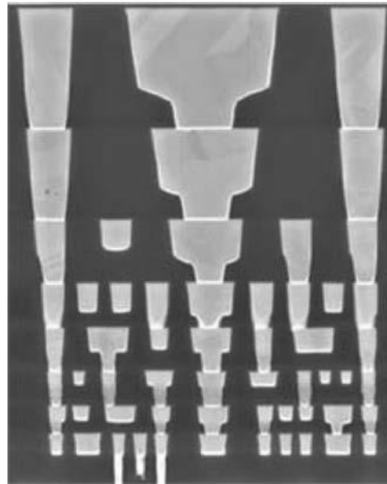

Figure 1: Multilevel Interconnect Cross Section (Li 2008, 734)

Fabrication of integrated circuits requires numerous intricate processes that are performed under strict environmental conditions. Manufacture of an IC begins with a thin wafer of semiconducting material that is typically silicon in most circuits today. Multiple individual circuits are built onto a single wafer at once for the increase of manufacturing productivity. An image of an Intel wafer with constructed integrated circuits can be seen in Figure 2. Layering of patterned materials to construct electrical components and interconnects are performed with photolithography and several layer

deposition processes (Yanda, Heynes, and Miller 2005). Fabrication of interconnects utilize photolithography to transfer the desired pattern into a previously deposited material layer by etching processes. Layer deposition techniques, such as physical vapor deposition (PVD), are applied to deposit a second material to fill in the trenches formed by etching. The result of layer deposition onto the etched surface is an uneven layer of the new material. Material fills in the trenches and also builds up on flat portions of the surface. If new layers of materials are successively deposited on patterned surfaces, the surface roughness rises with each layer (Li 2008, 734). Additional surface roughness causes issues in photolithography as the pattern transferred to the photoresist becomes increasingly inaccurate. With these inaccuracies of pattern transfer, the circuit features are out of specification and ultimately results in failure of the IC. Planarization of the wafer is thus a crucial process in integrated circuit manufacture and is the process of main concern in the current work.

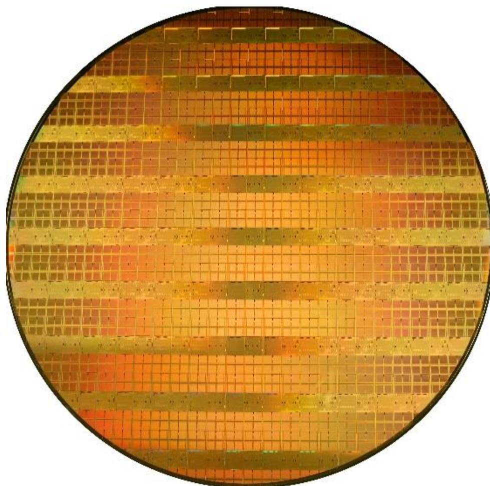

Figure 2: Intel Wafer with 45 nm Feature Size Chips (Intel 2006)

1.2 Chemical-Mechanical Planarization

The current method utilized for wafer planarization is the process of chemical-mechanical planarization (CMP). The main objective of CMP is to obtain flat uniform wafer surfaces from deposited patterned layers of material. The planarization process is also used to remove excess material, such as barrier layers between conducting and insulating materials that prevent the migration of atoms which can contaminate the circuit's transistors. Barrier layers must be removed so that interconnects are not all connected together since they can be made of conductive materials (Yanda, Heynes, and Miller 2005). CMP is a polishing process that utilizes a circular polishing pad that is loaded and rotated against the wafer to be planarized, as seen in Figure 3. A wet abrasive slurry is dispensed between the pad and wafer contact. The slurry consists of chemicals to soften the wafer material and hard abrasive particles to wear away the material. The main mechanism of planarization results from the loading of nano-sized abrasive particles onto the wafer surface by the polishing pad asperities (Luo and Dornfeld 2001, 112-133). Material removal is aided by softening of the wafer surface with slurry chemicals along with the carrying away of worn wafer material with the flow of fluid. The nanoscale particle abrasions produce nanoscale scratches which provide the required smooth surface for photolithography.

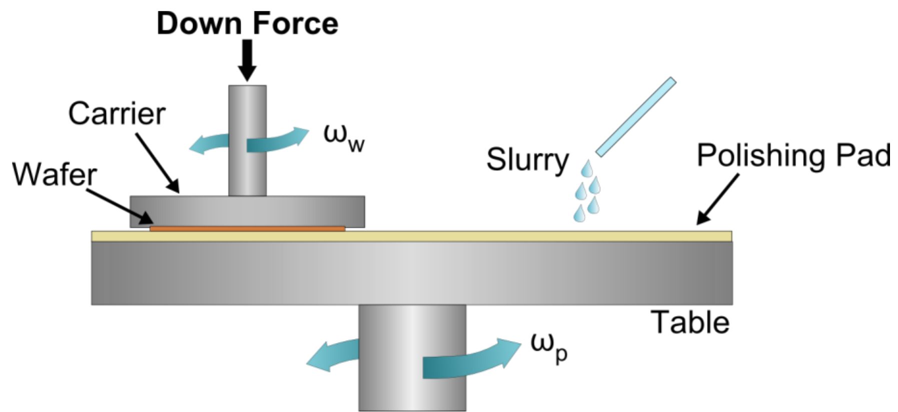

Figure 3: Typical Chemical-Mechanical Planarization Setup

The CMP process is customized for planarization of specific wafer materials by setting proper rotation speeds, wafer pressures, along with ideal polishing pad and slurry materials. The polishing pad material is selected to effectively transfer load onto the hard abrasive particles, yet not cause abrasions by the pad asperities themselves. The typical interconnect materials of today's integrated circuits consist of copper and silicon dioxide, as well as numerous other dielectrics. To reduce abrasions from large polishing pad asperities, pads are typically made of polymers since they are much softer than wafer materials (Kim, Saka, and Chun 2011, 393-404). A common polishing pad material is made of cast polyurethane foam (Steigerwald, Murarka, and Gutmann 1997). The porous and relatively rough nature of the pad has been shown to aid in transport of slurry into and out of the pad and wafer contact (Bajaj et al. 1994, 637-644; Choi et al. 2010, H806-H809; Kim, Seo, and Lee 2006, 362-370; Han et al. 2007, H525-H529). High roughness and pores on the pad surface allow for higher contact pressure per pad asperity, slurry circulation, and removal of wafer particles to increase material removal

and reduce defects. Over time, the pad's surface asperities can become flattened due to plastic deformation and pores also become clogged with slurry and worn wafer particles. The process of reducing pad surface roughness and clogging of pores is known as "glazing" of the pad. When "glazing" of the pad occurs, CMP experiments show a noticeable decrease in material removal rate and an increase in the potential for defects on the wafer. A process called pad conditioning is employed to roughen up the pad to reduce these issues. Pad conditioners consist of tools with diamond abrasives to cut into the pad surface. Conditioning the pad introduces a new rough pad surface with unfilled pores and has been experimentally shown to stabilize material removal rate (Steigerwald, Murarka, and Gutmann 1997; Li et al. 1995, 601-606; Prasad et al. 2011, H394-H400).

1.3 Wafer Damage from Chemical-Mechanical Planarization

It has been noted in the literature that wafer defects caused by the CMP process have become more prevalent with the decrease in IC feature sizes and implementation of new materials (Eusner et al. 2009, H528-H534; Teo et al. 2004, 65-69; Chandra et al. 2008, 559-562). Since the first integrated circuit was commercially introduced in the late 1950s, there has been an approximate exponential increase in the number of components on an integrated circuit over time (Mack 2011, 202-207). The increase in component quantity results from the combination of increased chip area from layering, intelligent IC layout design, and decreasing feature size. The desire to increase the computing performance of integrated circuits drives the decrease in component size. As

feature size decreases, defects that are produced on the wafer surface through CMP become more problematic. Today, the smallest representative feature size produced in commercially available ICs is 14 nm in width (ITRS 2013). Defects produced on the nanoscale can now be detrimental to wafer yield. To achieve high manufacturing yields, the CMP process has to be properly controlled so that material removal of the wafers is completed at a small enough length scale.

Another contribution to the increasing prevalence of defects from CMP is the shift to softer or more porous materials for the interlayer dielectric (ILD). These ILD materials are the insulating materials that separate the interconnecting patterned wires within the IC. The standard ILD in integrated circuits that is still widely used today is silicon dioxide. The switch to different insulators stems from the desire to reduce capacitance, which results in increasing the rate that electricity flows throughout the chip (Yanda, Heynes, and Miller 2005; Steigerwald, Murarka, and Gutmann 1997). An insulator between metal interconnects with a higher dielectric constant, or *k*-value, will store more electrical charge and will behave as a larger capacitor. Thus, use of insulators in the ILD with a lower *k*-value will greatly speed up the circuit as there is less capacitance throughout the metal interconnects, giving a shorter delay time. Low-*k* dielectrics also provide a decrease in crosstalk between metal wires and less power dissipation. The issue comes into play with CMP as these low-*k* materials are generally softer than silicon dioxide (Thagella 2004, G205-G215; Chandrasekaran et al. 2004, G882-G889). Many also have a porous solid structure that additionally decreases the strength of the material. With decreased material strength, low-*k* films are easier to scratch and damage during CMP than previously used dielectrics.

As the continuous desire for faster integrated circuits progresses, conditions of the CMP process are becoming more stringent. These challenges require revised mechanical modeling of the process to understand the cause of wafer damage. The wafer defects of main concern in this work are the scratches produced by the softer polishing pad material on harder wafer materials. The nanoscale abrasive particles in the slurry remove material through small enough abrasions to be the ideal method of material removal in CMP. Material removal by pad asperities can destroy wafers as these asperities have radii of curvature on the microscale. Scratches that are produced by these asperities can also be on the microscale, which are larger than some IC features. These "killer" scratches will destroy any features on the wafer that are smaller than the defects produced.

Previous work that has investigated CMP scratching provides criteria which can predict scratching and presents methods to reduce it (Eusner, Saka, and Chun 2011, H379-H389; Kim et al. 2013, 307-310). Scratching is not completely eliminated from the process with these suggestions to better CMP. The research at hand will add to past work by determining the mechanisms which result in wafer damage. A complete understanding of the thermomechanical processes which produce scratches is essential to prevent wafer damage in CMP. The obtained model of CMP will provide insight into preventing the scratches by redesigning the process or altering its operational conditions to remove these mechanisms which result in pad scratching of IC wafers.

CHAPTER 2

REVIEW OF LITERATURE

To further explain the importance of chemical-mechanical planarization, issues with pad scratching as well as significance of the current work, a review of the literature on these subjects is provided. A discussion on the reasons for implementation of chemical-mechanical planarization (CMP) is first delivered, providing the reader with a better understanding of why CMP is used and the process requirements. Before a discussion on CMP scratch mechanics, a presentation of some of the first mechanical models of CMP is given. More recent mechanical models which aim to describe material removal processes are presented next. Inclusion of these topics provides a general understanding of the mechanics of the process, laying the foundation for CMP modeling. Next is a transition into a discussion on the different ways that wafer defects can be produced. Finally, a discussion on the work which has been completed to model wafer scratching from pad asperities is presented. Based on the presented literature, the reasons for the completion of the current research is discussed.

2.1 Selection of CMP for Integrated Circuit Fabrication

The mainstream implementation of CMP for integrated circuit (IC) wafer production came about from new design requirements for next generation chips. With the need to construct more powerful circuits, new designs require smaller features and

larger numbers of electrical components. The minimum half-pitch between IC features was approaching 0.5 um for new chip designs in the early-1990s. As a result, a requirement for a planarization technique of metal interconnects emerged (Li 2008, 734; Steigerwald, Murarka, and Gutmann 1997; Banerjee and Rhoades 2008, 1-19). The first implementation of CMP occurred in 1990 for multilevel metallization. Planarization of wafers would allow for smaller feature sizes combined with multilevel interconnects. Smaller component sizes on multiple levels would allow support of the growing number of transistors and increasing complexity of the chips. Construction of multilevel interconnects requires deposition of a new material layer onto a patterned wafer. Material deposition onto the patterned wafer results in an uneven surface corresponding to the patterns, as in Figure 4. With multiple layers of interconnects, non-planar topography will accumulate which would cause issues in the photolithography of interconnect patterns for the following layer, as represented in Figure 5. The depth of focus for photolithography for sub-0.5 um circuit fabrication is on the nanoscale (Steigerwald, Murarka, and Gutmann 1997; Murarka, Steigerwald, and Gutmann 1993, 46). A photolithographic stepper is used to expose interconnect patterns on a photoresist coating for etching. The flatness of the wafer needs to be on the nanoscale within the stepper's field of view, which is on the order of at least 100 mm^2. To properly expose and etch the interconnect patterns, global planarization of the wafer is necessary.

Figure 4: Wafer Cross Section after Metal Deposition

Figure 5: Layer Representation of an IC Fabricated without Planarization (Li 2008, 734)

Chemical-mechanical planarization was chosen as the required planarization technique for a number of reasons. It is the only available technique that achieves desired global planarization across a wafer of varying topographical features (Li 2008, 734; Steigerwald, Murarka, and Gutmann 1997). Other potential planarization techniques that are used in IC fabrication include spin on glass deposition, silicon dioxide flow from high temperature annealing, and various etching methods. These techniques only provide local planarization or smoothing of the surfaces. Local planarization occurs when the surface is flat only among an array of circuit features as shown in Figure 6, which is not sufficient for the required photolithographic processes.

Other reasons for why CMP was chosen as the planarization process include its versatility and relatively low cost. With a proper selection of polishing pad, slurry, and polishing boundary conditions, CMP can be utilized to sufficiently polish almost any material. The process also allowed for the switch from aluminum interconnects to the less resistive copper interconnects through the use of the dual damascene process (Li 2008, 734; Steigerwald, Murarka, and Gutmann 1997; Steigerwald et al. 1995, 217-217). Etching of copper is impractical in IC fabrication with its inability to form volatile compounds in the required manufacturing environment. CMP and dual damascene allow for etching of the lines and vias in the dielectric only, thus avoiding copper etching. The dielectric is etched twice with different patterns, as represented in Figure 7. The dual damascene process is currently used to fabricate multilevel interconnects in the most advanced circuits.

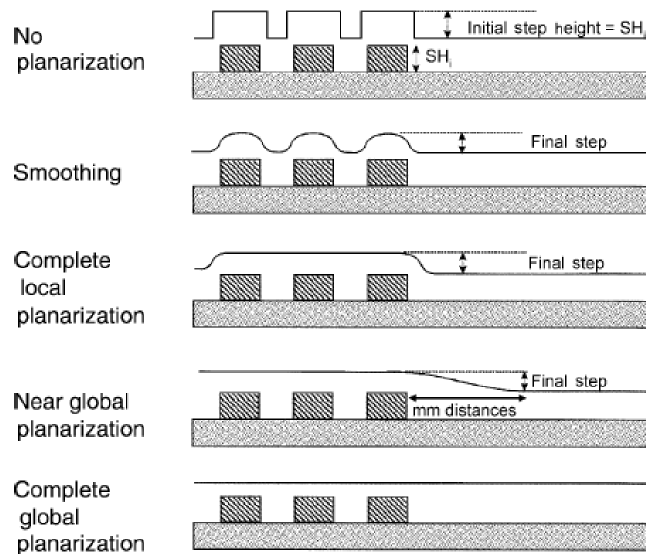

Figure 6: Levels of IC Planarization (Li 2008, 734)

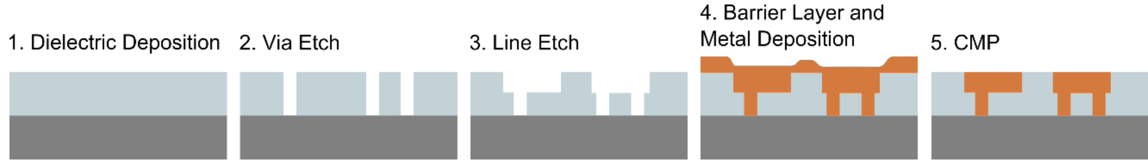

Figure 7: Dual Damascene Process

2.2 General Mechanical Modeling of CMP

Many of the first mechanical models constructed in the literature describe the mechanical interactions of the polishing pad, wafer, and abrasive slurry to predict the material removal rate (MRR) and with-in wafer non-uniformity (WIWNU) of material removal. Proper prediction and understanding of material removal offers a greater knowledge to properly design CMP processes for specific materials and conditions. Physical knowledge of CMP is indispensable in improving issues such as non-uniformities and defect generation. Some of the more basic mechanical models in the literature aim to correlate contact stress distributions, on the scale in size of the wafer diameter, to non-uniformities of material removal (Wang et al. 1997, 1121-1127; Srinivasa-Murthy et al. 1997, 533-537; Lin, Chen, and Ma 2009, 6027-6033; Timoney, Ahearne, and Byrne 2010, 155-160; Wang et al. 2013, 1974-1979). Work on elementary CMP models began to be published approximately two years after the mainstream implementation of CMP. Using a basic wafer-scale finite element model, the contact and von Mises stresses on the wafer were computed from a uniform applied traction onto a polishing pad. In each study, all materials were modeled as flat, smooth, linearly

elastic materials. The resulting von Mises stress profile across the wafer was found to correlate with experimental MRR wafer profiles. An increase in stress at the edges of the wafer was found to cause an increase in MRR at the corresponding wafer radii, where the height of the wafer decreases (Wang et al. 1997, 1121-1127; Srinivasa-Murthy et al. 1997, 533-537; Timoney, Ahearne, and Byrne 2010, 155-160; Wang et al. 2013, 1974-1979).

Additional work has been performed to include the influences of slurry fluidic pressure on wafer-scale contact stress models (Tichy et al. 1999, 1523-1528; Shan et al. 2000, 539-543). These macroscopic models of CMP mechanics were created with assumptions of the wafer as a rigid flat surface and the pad as a flat elastic surface. Models that include wafer deformation and curvature due to wafer film stress have also been constructed (Tseng, Wang, and Chin 1999, 4273-4280; Wu 2009, 929-939). Information on material removal rates and non-uniformities based on contact stresses from wafer curvature were obtained. From these works, a greater physical understanding of the process was acquired with calculations of contact pressure, pad surface displacement, slurry fluid pressure, and slurry film thickness distributions across the wafer. This knowledge provides a general understanding of the trends in important parameters with different velocities and applied loads, laying the groundwork for CMP mechanics modeling.

Models that predict material removal during CMP have been formulated at different length scales in the literature. Most models exist on the scale of the wafer diameter or the size of the pad surface asperity. The wafer scale models on their own can only describe the basic trends of material removal with the overall behavior of

mechanical parameters. Modeling CMP material removal on the scale that it occurs is necessary for a complete understanding of the planarization process. It is widely accepted in the literature that the principal material removal mechanism in CMP is through the abrasion of slurry particles (Luo and Dornfeld 2001, 112-133; Qin, Moudgil, and Park 2004, 277-286; Fu et al. 2001, 406-417; Wang et al. 2005, 309-312; Seok et al. 2004, 496-508; Kim, Saka, and Chun 2014, 431-442; Bastawros et al. 2002, 1022-1031; Bozkaya and Muftu 2009, H890-H902). Abrasive particles are loaded onto the wafer by the moving pad asperities and plough through the chemically softened wafer surface. A basic depiction of the process is seen in Figure 8 from a research paper which models this nanoscale removal process (Bastaninejad and Ahmadi 2005, G720-G730). Other mechanisms of material removal that have been discussed are three-body abrasion and adhesion by rolling particles, yet they have not been widely covered in CMP modeling (Luo and Dornfeld 2001, 112-133; Bozkaya and Muftu 2009, H890-H902; Bastaninejad and Ahmadi 2005, G720-G730; Seok et al. 2003, 307-320; Ahmadi and Xia 2001, G99-G109). One of the first comprehensive models of material removal accounted for material removal rate based on the volume removed per time of a single rigid abrasive particle (Luo and Dornfeld 2001, 112-133). The volume removal rate was determined based on estimates of the applied force, indentation depth, and projected contact area after plastic indentation of a particle into the wafer. The size distribution of slurry particles and number of active abrasive particles was estimated to account for the material removal of all abrasive particles. The outcome is a model for material removal as a function of pad and wafer mechanical properties, abrasive size and geometry, applied pressure, and relative velocity.

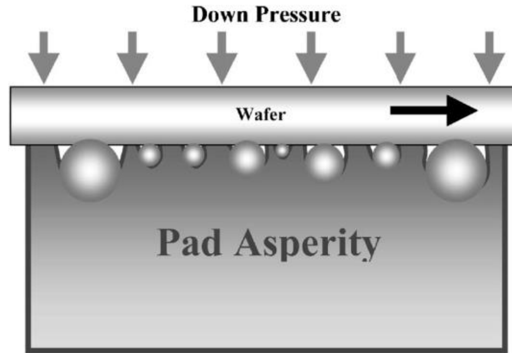

Figure 8: Material Removal Process (Bastaninejad and Ahmadi 2005, G720-G730)

Recently, a material removal model has included the influences of pad topography and plastic deformation of pad asperities to further advance the mechanical understanding of CMP (Kim, Saka, and Chun 2014, 431-442). Since the abrasive slurry particles are much smaller in scale and harder than pad asperities or the wafer surface, the material removal model also accounted for indentation of rigid spherical slurry particles into the pad asperities. The material removal from a single slurry particle was determined based on the particle radius, wafer hardness, and applied load. Based on single slurry particle material removal, a function for material removal of an assumed spherical pad asperity was determined as a function of slurry volumetric particle concentration.

The model also accounted for the roughness and varying pad asperity heights (Kim, Saka, and Chun 2014, 431-442). Pad roughness was accounted for by determining the load that a pad asperity places on abrasive slurry particles depending on how much the pad asperity is deflected and its mode of deformation. Assuming an exponential distribution of pad asperity heights, integral relations summing up the material removal

rate of all asperities on a pad provided the material removal rate model. The integrals were separated into pad asperities which are either under elastic, elastic-plastic, or fully plastic deformation. Roughness was accounted for by the varying amounts of load each slurry particle will see depending on how much the pad asperity is being deflected. The final material removal rate model was presented as a function of nominal pressure, relative velocity, pad and wafer hardness, pad asperity radius, pad asperity height distribution, and slurry particle concentration, among other parameters. It is one of the more inclusive material removal models as it considers important contributions from pad topography, which has shown to be an important factor during CMP (Steigerwald, Murarka, and Gutmann 1997; Bajaj et al. 1994, 637-644; Li et al. 1995, 601-606; Prasad et al. 2011, H394-H400). A greater understanding of material removal mechanisms in CMP and their effective modeling methods was obtained.

2.3 CMP Scratching by Abrasive Particles and Wear Debris

As IC feature sizes become smaller and dielectric materials become more compliant, scratching of wafers is becoming a greater issue during chemical-mechanical planarization (Eusner et al. 2009, H528-H534; Teo et al. 2004, 65-69; Chandra et al. 2008, 559-562). The issue of scratching has attracted a lot of attention in the literature and several types of scratches and defects have been stated to occur during CMP. The first type of scratching that is presented here are the scratches produced by single abrasive slurry particles through the applied load from pad asperities. As discussed previously for material removal mechanisms, the wear of abrasive slurry particles to

achieve nanoscale material removal is the desired result for polishing. Work has been done to determine the maximum scratch width and depth produced by an abrasive slurry particle in CMP (Eusner et al. 2009, H528-H534; Saka, Eusner, and Chun 2008, 341-344; Eusner, Saka, and Chun 2010, 22-37). This scratching process is shown in Figure 9. Assuming a rigid spherical slurry particle indenting a fully plastic pad asperity and wafer, relations for the upper-bound scratch width and depth of a particle were found. These scratch size bounds were a function of the particle diameter and hardness ratio of pad to wafer materials. Based on maximum hardness values of a typical IC1000 polishing pad and the average hardness of copper, the maximum scratch width was found to be a quarter diameter of the abrasive slurry particle. Also, the maximum scratch depth was found to be smaller than the scratch width. It was shown that with properly controlled material hardness and slurry particle size, the maximum scratch size of a single slurry particle can be limited to achieve the desired polishing. Slurry particle diameters in CMP are generally on the order of 10 nm to 100 nm (Zhang, Liu, and Song 2010, 5480-5485; Krishnan, Nalaskowski, and Cook 2010, 178-204). When designed properly, this type of single slurry particle polishing provides smooth and flat surfaces relative to the features on the circuit.

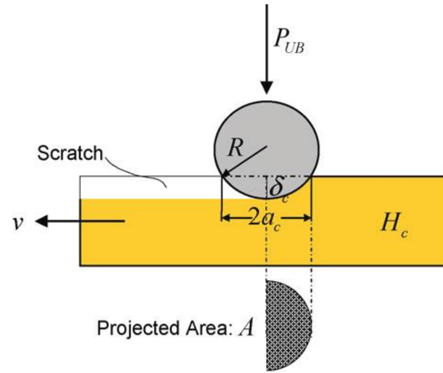

Figure 9: Abrasive Slurry Particle Polishing a Wafer Surface (Saka, Eusner, and Chun 2008, 341-344)

Origins of scratches that result in defects of the wafer and thus reduce integrated circuit yields in manufacture have been commonly covered in the literature. The most widely covered type of CMP scratching has been found to result from relatively large particles. Certain types of particles can form during the planarization process that are larger than the intended slurry abrasive particle. The most common examples of large particles which result in defects are particles fractured from the wafer, pad debris, diamond conditioner particles, and slurry particle agglomerates (Prasad et al. 2011, H394-H400; Teo et al. 2004, 65-69; Chandrasekaran et al. 2004, G882-G889; Ring et al. 2007, H239-H248; Choi et al. 2010, H186-H191; Chandra, Karra, and Bastawros 2010, 9-20; Sung, Kim, and Yeo 2012, 8298-8306; Kwon et al. 2013, 169-175). Particles from the wafer itself were found to be introduced into the slurry through brittle fracture or flaking of the surface (Chandrasekaran et al. 2004, G882-G889; Ring et al. 2007, H239-H248). These particles, if large enough, can cause additional damage if loaded onto the wafer. Also, it has been found experimentally that an increase in pad debris in CMP increases scratch generation (Prasad et al. 2011, H394-H400; Sung, Kim,

and Yeo 2012, 8298-8306; Kwon et al. 2013, 169-175). Pad debris is generated primarily from conditioning of the pad. A mechanism for scratching from the relatively soft polymer pad debris has not been presented in the literature. It has been suggested that the scratching is the result of a physical interaction between the pad debris and abrasive slurry particles. Additionally, a potential cause of scratching is the release of microscale diamond particles from diamond pad conditioners (Kwon et al. 2013, 169-175). The very hard diamond particles easily produce scratches when loaded on the wafer surface.

One of the more common sources of wafer scratching results from agglomeration of slurry particles. These clusters of particles can reach diameters an order of magnitude greater than that of a single particle (Ihnfeldt and Talbot 2006, G948-G955). Particle agglomerates effectively act as a large abrasive particle, thus producing scratches on the wafer which are large enough to destroy circuit features. It has been experimentally shown that the number of "killer" scratches that form exponentially increases with agglomerate size (Li 2008, 734). Conditions in which agglomerates form generally have to do with the chemistry of the slurry. When the pH of the slurry is near the iso-electric point of the abrasive particles, they begin to adhere to one another (Chandra et al. 2008, 559-562; Ihnfeldt and Talbot 2006, G948-G955). This adhesion is a result of zero surface charge on the particles' surfaces, so that there is then no barrier to repel each other. Particle agglomeration is also a function of temperature and viscosity of the slurry, among other parameters. This clustering can be prevented with proper chemical additives to shift the pH away from the particles' iso-electric point (Ihnfeldt and Talbot 2006, G948-G955). Submicron filtering of slurry is

employed during CMP to remove larger agglomerates of particles from the slurry as it is dispensed to help prevent scratching (Li 2008, 734).

2.4 CMP Scratching by Pad Asperities

Though it is mainly understood that scratching in CMP only results from hard abrasive slurry particles, recent work has shown that the relatively soft pad asperities can produce scratches on wafers (Eusner, Saka, and Chun 2010; Kim, Saka, and Chun 2011, 393-404; Eusner, Saka, and Chun 2011, H379-H389; Kim et al. 2013, 307-310; Saka, Eusner, and Chun 2010, 329-332; Kim, Saka, and Chun 2014, P169-P178). Pad scratching has only recently been observed and treated as an issue in the literature. Experiments in the literature have shown that scratches in CMP can occur without slurry particles and conditioning of the pad. Since these pad asperities are on the microscale in radius, a scratch produced by the pad can easily destroy nanoscale features of the most current circuits in production. So-called “killer” scratches from pad asperities can be seen in Figure 10. It is desired to understand the conditions under which these defects can occur. With a physical understanding of the pad scratching process, methods for the prevention of pad scratches may be employed.

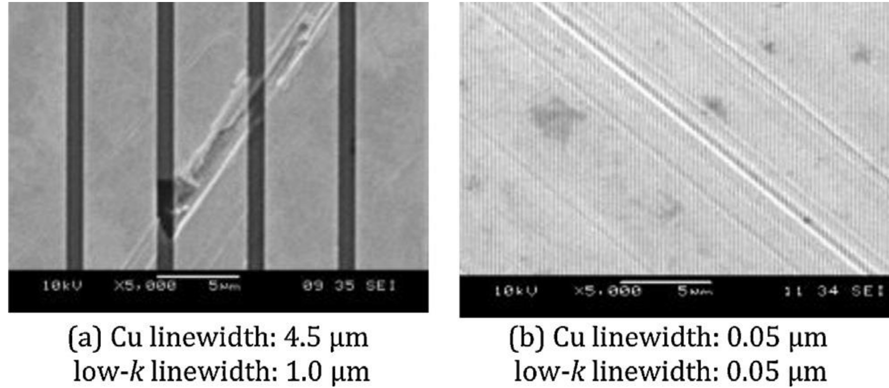

Figure 10: Scratches Produced from Pad Asperities during CMP (Kim et al. 2013, 307-310)

In the literature, a contact mechanics model that describes the general mechanics of soft pad scratching has recently been constructed (Eusner, Saka, and Chun 2010; Kim, Saka, and Chun 2011, 393-404; Kim et al. 2013, 307-310; Saka, Eusner, and Chun 2010, 329-332; Kim, Saka, and Chun 2014, P169-P178). The model is based on mathematical relations to describe the contact pressure distribution of a single spherical pad asperity loaded onto a flat wafer surface. The mode of asperity deformation was shown to affect its contact pressure. With this, the amount of pad asperity deflection determines if the asperity is elastically or plastically deformed. The levels of deflection of the asperity at the onset of yielding, and at which it is fully plastically deformed, were theoretically modeled. These deflection levels separated the deformation modes into elastic, elastic-plastic, and fully plastic deformation. The average contact pressure of the asperity on the wafer surface for each mode of deformation was determined from a range of theoretical, numerical, and experimentally-based models.

Tresca and von Mises yield criteria were utilized to achieve the average asperity contact pressure at which the wafer surface would yield, and thus produce scratches

(Saka, Eusner, and Chun 2010, 329-332; Kim, Saka, and Chun 2014, P169-P178). These relations for maximum shear stress or von Mises stress also included shear stresses along with the applied normal tractions. This shearing stress is induced from the frictional sliding contact of the pad asperity and wafer. Stress distributions in the wafer were developed theoretically as well as through finite element analysis, modeling wafer stresses from the sliding pad asperity tractions. These relations provide the means to construct scratching criteria for single asperities. Ultimately, the wafer scratch criterion for a single asperity was put into a function of the ratio of pad hardness to wafer hardness, coefficient of friction, and mode of pad asperity deformation.

A multi-asperity model for pad scratching was constructed using the relations for single asperities (Kim, Saka, and Chun 2014, P169-P178). This model assumed all pad asperities have the same radius of curvature, the asperities do not interact with each other, and that the asperity heights are exponentially distributed. The probability density of pad asperity heights was used to predict the number of pad asperities in contact with the wafer surface, as well as the number of asperities in each mode of deformation. This was done by integrating the probability density of pad asperity heights in between the levels of deflection at the onset of yielding and at fully plastic deformation. Ratios for the number of pad asperities in contact with the wafer surface that are elastically deformed and plastically deformed were given. The deformation mode ratios allowed for application of single pad asperity scratch criteria for a multi-asperity contact.

From the scratch criteria, it was shown that plastically deformed pad asperities can scratch the wafer more easily than those that are elastically deformed (Eusner, Saka, and Chun 2010; Kim, Saka, and Chun 2011, 393-404; Kim et al. 2013, 307-310; Saka,

Eusner, and Chun 2010, 329-332; Kim, Saka, and Chun 2014, P169-P178). Ratio of elastic to plastic pad asperities was given as a function of pad elastic modulus, pad hardness, pad asperity radius, and standard deviation of asperity height. This work conducted experiments on two CMP pads to acquire these mechanical and topographical values. Based on the model and experimental values, it was found that over 92% of pad asperities contacting the wafer surface were plastically deformed for each pad (Kim, Saka, and Chun 2014, P169-P178). In this case, the plastically deformed scratch criteria was utilized in experimental validation.

Scratching experiments were conducted on multiple wafer materials to validate the model (Kim, Saka, and Chun 2014, P169-P178). These experiments measured the coefficient of friction between pad asperities and wafer surfaces through the CMP process. Also, production of scratches was observed after each experiment. The scratching model was shown to fit the data well when extreme values of hardness were used for the scratch criteria. In other words, the maximum measured hardness of the pad asperities and the minimum measured hardness of the wafers were used for the best scratch prediction results. The model and experimental results showed that pad scratches can be mitigated by reducing the value for the ratio of pad to wafer hardness. In addition, the coefficient of friction between the pad and wafer can be reduced to mitigate scratches. The model also suggested that since it is easier for plastic pad asperities to scratch a wafer surface, the number of plastically deformed pad asperities in contact with the wafer surface should also be reduced to mitigate scratching. Reducing pad scratches can be done by decreasing the ratio of pad elastic modulus to

hardness, as well as reducing the ratio of pad asperity height standard deviation to pad asperity radius of curvature.

Sliding experiments were conducted which effectively observed the effect of lowering the coefficient of friction to prevent scratching (Saka, Eusner, and Chun 2010, 329-332). Work has also been done to demonstrate the mentioned effects of pad topography on pad scratching. Polishing experiments have shown that a broken-in pad produces less scratches on a wafer than a new pad (Eusner, Saka, and Chun 2011, H379-H389). Reduced scratches with a broken-in pad is a result of an increase in the radius of curvature of asperities and a decrease in the asperity height standard deviation, as suspected from the theoretical models. This same method of reducing scratching by alteration of pad topography was more recently investigated (Kim et al. 2013, 307-310). This work presented methods of flattening pad asperities to prevent pad scratching. Flattening the pads increases the asperity radius of curvature, as well as decreases the standard deviation of height. Thus, fewer asperities are plastically deformed on the wafer in contact. Scratching experiments showed that there is less scratching with flattening of pad asperities, as the pad scratching model predicted.

The literature has found that relatively soft polishing pads can scratch wafers during CMP without abrasive particles or pad conditioning. Physically understanding CMP pad scratching is crucial to its prevention. The work that has been done to model pad scratching accurately predicted when these defects can occur. Methods of pad scratching mitigation were also presented based on the findings of the model and experimental results. Yet, the experimental results showed that scratching is not completely eliminated from the process with the suggested alterations to the pad and

wafer materials. The current research will add to past work by constructing a comprehensive mechanistic model for the process of pad scratching. A complete understanding of the thermomechanical processes which produce scratches is essential to prevent wafer damage in CMP. Thorough analysis into the mechanical behavior of the pad material will be included to improve upon contact mechanics modeling. This constitutive pad modeling will be accomplished by accounting for mechanical behaviors such as pad compressibility and time-dependent deformation. Thermodynamic processes which occur through the CMP process and pad scratching will be observed and taken into account. This theoretical analysis combined with information obtained from experimental data will aid in the construction of a thermomechanical model to determine the physical mechanisms that cause and influence pad scratching. With a complete thermomechanical model, the specific CMP conditions which allow for the scratching process to occur will be understood and thus may be altered to prevent scratching.

CHAPTER 3

METHODOLOGY

Preventing scratches from occurring in chemical-mechanical planarization (CMP) requires a thorough understanding of the scratching mechanisms. The physical processes that induce damage onto the wafer are of a mechanical and thermodynamic nature. During CMP, the wafer and polishing pad are pressed together providing the mechanical tractions which induce stress fields in both materials. Energy is input to the CMP system through the mechanical work of pad tractions onto the wafer surface. Part of this input energy is dissipated through several processes that include damaging the wafer surface. In this work, a thermomechanical model is constructed to appropriately describe the physical processes at work in CMP pad scratching. Thermodynamically partitioning each form of dissipation provides an understanding of how the energy is transferred between the pad and wafer. Determination of the different forms of dissipation requires proper mechanical and thermodynamic analysis that is aided with experimental data. The results explain mechanisms of CMP pad scratching for damage prevention in integrated circuit (IC) fabrication.

The current analysis applies physical principles with appropriate models of mechanics and thermodynamics to explain the scratching process. Thermodynamic modeling of the pad scratching process involves the application of the Clausius-Duhem inequality, also known as the second law of thermodynamics. Applying this inequality provides an analytical description of how energy is dissipated during pad scratching.

The contributions of each form of energy dissipation uncover the mechanisms of polishing pads that scratch the IC wafers. The pad scratching model considers variables that influence the occurrence of scratches as well as the resulting scratch severity. Acquiring this information requires conducting experiments that replicate the CMP process. The obtained experimental contact forces, topography, wear and internal energy changes of CMP materials provide information necessary to determine the relative contributions of dissipation processes.

Proper mechanical modeling of the polishing pad and wafer contact require constitutive models to describe the deformation resulting from the applied loading conditions. The mechanical behavior of typical wafer materials is well known in the literature as they are common engineering materials. Polymeric polishing pads are studied less often since these materials are specific to CMP and much information on the material fabrication processes and properties of these pads is proprietary. As a result, mechanical characterization of polishing pad material is conducted experimentally. The resulting constitutive models for the pad and wafer materials are applied to the loading conditions and material geometries of CMP. The resulting contact mechanics model provides information about strain energy in the pad and wafer materials from the applied tractions.

3.1 Thermomechanical Modeling of Wafer Damage

To understand the mechanisms of scratching by the softer pad on the harder wafer material, mechanical and thermal processes that occur during CMP are analyzed.

A thermomechanical model of the scratching process is constructed to uncover information about the conditions through which pad scratching can transpire. Analysis of these conditions requires computation of stress associated with the pad and wafer contact, as well as tracking the energy dissipation processes of CMP.

Developing a method to account for the damage induced on a wafer from pad scratching is key to understanding the mechanisms of the process. When the wafer has yielded due to tractions applied from the pad surface, damage is produced on the wafer through scratching. Damage is represented as a plastic deformation of the wafer surface, a dissipation of energy and an increase in entropy. To account for damage produced by pad scratching, laws of thermodynamics are applied. All energy that is input into the system is accounted for using the first law of thermodynamics, also known as the law of conservation of energy. This law states that all energy of a system cannot be destroyed and must be conserved, all due to the interconvertibility of the energy processes. In the case of chemical-mechanical planarization, the system of interest includes the polishing pad, wafer, and slurry. For the dynamic process of CMP, the first law of thermodynamics in the form of the time rate change of energy is used. The relation for the conservation of the time rate of change of energy at any point in a continuum is given in Equation 1 (Lai, Rubin, and Krempl 2010),

$$\rho \frac{Du}{Dt} = \boldsymbol{\sigma} : \boldsymbol{D} - div\ \bar{q} + \rho r \qquad \text{Equation 1}$$

ρ is the mass density, u is the internal energy per unit mass, $\boldsymbol{\sigma}$ is the Cauchy stress tensor, **D** is the rate of deformation tensor, $\bar{q}$ is the heat flux vector, and r is the heat supply per unit mass. Subtraction of the divergence of $\bar{q}$ accounts for the heat that is being fluxed

into the system. $\frac{D}{Dt}$ is the Lagrangian rate of change which describes the time derivative of a material particle itself, as opposed to the time derivative with respect to a spatial location. This energy equation is for a material for which the stress state provides a symmetric Cauchy stress tensor **σ**, where there are no body moments per unit volume. Body forces are not considered in this analysis, so this assumption is acceptable.

From the first law of thermodynamics, the energy input into the pad and wafer contact must be conserved. In CMP, all of the energy that is input to the wafer is from the pad's applied tractions. This energy is the mechanical work of the pad sliding against the wafer, which is measureable through force and distance information. Part of this energy is dissipated through damaging the wafer material from scratching and other potential dissipation processes. This energy cannot be directly measured as energy dissipation is represented by an increase in entropy. To account for the dissipation, the second law of thermodynamics in the form of the Clausius-Duhem inequality is applied for any point in a continuum, given in Equation 2 (Lai, Rubin, and Krempl 2010),

$$\rho \frac{D\eta}{Dt} \geq -div\left(\frac{\bar{q}}{\Theta}\right) + \frac{\rho r}{\Theta} \qquad \text{Equation 2}$$

η is the entropy per unit mass and Θ is the absolute temperature. Also known as the second law of thermodynamics, this inequality states that the rate of entropy increase of a system is greater than or equal to the entropy that fluxes into the system, plus entropy that is formed within the system. Entropy that fluxes into the system may be in the form of sensible heat, mass, and acoustics, among other forms, as represented by $-div\left(\frac{\bar{q}}{\Theta}\right)$. The entropy that is formed within the system is known as configurational entropy,

represented by $\frac{\rho r}{\Theta}$. Part of the configurational entropy changes of the material result from plastic deformation among other potential dissipation processes. Thus, part of the configurational entropy changes account for the dissipation that results from material damage through plastic deformation. The main goal is the decomposition of the individual processes contributing to the configurational entropy changes of the CMP process to determine exactly how the wafer is being deformed from the applied tractions of the polishing pad.

To decompose the configurational entropy changes further, the energy equation is combined with the Clausius-Duhem inequality. Equation 1 is first rearranged to solve for the heat supply in the system, which makes up the configurational entropy changes,

$$\rho r = \rho \frac{Du}{Dt} - \boldsymbol{\sigma} : \boldsymbol{D} + div\, \bar{q} \qquad \text{Equation 3}$$

Applying the derivative quotient rule for the divergence of the heat flux vector over absolute temperature gives the two terms in Equation 4,

$$div\left(\frac{\bar{q}}{\Theta}\right) = \bar{\nabla} \cdot \left(\frac{\bar{q}}{\Theta}\right) = \frac{div(\bar{q})}{\Theta} - \frac{\bar{q} \cdot \bar{\nabla}\Theta}{\Theta^2} \qquad \text{Equation 4}$$

$\bar{\nabla}$ is the vector differential operator del. Substituting Equation 3 and Equation 4 into Equation 2 results in a new form of the Clausius-Duhem inequality presented in Equation 5,

$$\rho\Theta\dot{\eta} \geq \rho\dot{u} + \frac{1}{\Theta}(\bar{q} \cdot \bar{\nabla}\Theta) - \boldsymbol{\sigma} : \boldsymbol{D} \qquad \text{Equation 5}$$

The dot accent represents the material derivative with respect to time. When applied to chemical-mechanical planarization, all of the terms in Equation 5 provide the means to

account for each individual dissipation process that occurs in pad scratching. It is with this equation that no assumptions are made to remove potential sources of dissipation.

For the pad scratching process, $\rho\dot{u}$ represents the rate of change of internal energy of the CMP materials. The polishing pad and wafer represent the system being considered. For this model, internal energy changes of the polyurethane polishing pad are a function of the change of chemical structures in the material, if they occur. New phases or chemical forms of the polyurethane may arise due to energy input from the stresses or sensible heat of the process. In this work, differential scanning calorimetry (DSC) is conducted on the pad material to extract information on internal chemical changes of the IC1000 pad through CMP. For the wafer material, internal energy changes occur through plastic deformation of the material as it is damaged. This plastic energy dissipation is not accounted for with the internal energy term, but with strain energy, to be discussed.

The flux term $\frac{1}{\Theta}(\bar{q} \cdot \bar{\nabla}\Theta)$ symbolizes the flux of energy dissipation. Energy dissipation is fluxed from the system though mass, acoustic, and sensible heat fluxes, among others. This work focuses on the energy fluxes due to loss of wafer mass as it is worn away during the CMP process. This mass loss is related to the energy required to form new surface area of the wafer material. The worn mass is fractured from the wafer surface through wear, and thus surface energy or a critical energy release rate of the material is used to estimate the energy. The critical energy release rate of the material coupled with mass loss and topographical changes allow for an estimation of this dissipated energy.

The term $\boldsymbol{\sigma} : \mathbf{D}$, that includes the Cauchy stress tensor and the rate of deformation tensor, represents the rate of strain energy in the pad and wafer materials. This term can be assembled into different forms of strain energy by decomposing the stress and rate of deformation terms. The Cauchy stress tensor can be described by its elastic and plastic components by a relation from Maugin given in Equation 6 (Maugin 1992, 38),

$$\boldsymbol{\sigma} = \boldsymbol{\sigma}^{e} + \boldsymbol{\sigma}^{p} \qquad \text{Equation 6}$$

$\boldsymbol{\sigma}^{e}$ is the elastic portion of stress and $\boldsymbol{\sigma}^{p}$ is the plastic portion of stress. Separating the plastic stress allows for the isolation of energy dissipation due to viscous effects in the material. Since no assumptions were made to remove any contributions of dissipative energy, viscoelastic effects must be accounted for in addition to those of elastic and plastic effects. The rate of deformation tensor is decomposed similarly using the Green-Naghdi Decomposition provided in Equation 7 (Green and Naghdi 1965, 251),

$$\boldsymbol{D} = \boldsymbol{D}^{e} + \boldsymbol{D}^{p} \qquad \text{Equation 7}$$

$\mathbf{D}^{e}$ is the elastic portion of the rate of deformation tensor and $\mathbf{D}^{p}$ is the plastic portion. The plastic part of the rate of deformation provides the ability to account for dissipations due to plastic deformations of the material. Substituting Equation 6 and Equation 7 into the strain energy term results in an expansion of the rate of strain energy presented in Equation 8,

$$\boldsymbol{\sigma} : \boldsymbol{D} = \boldsymbol{\sigma}^{e} : \boldsymbol{D}^{e} + \boldsymbol{\sigma}^{p} : \boldsymbol{D}^{e} + \boldsymbol{\sigma}^{e} : \boldsymbol{D}^{p} + \boldsymbol{\sigma}^{p} : \boldsymbol{D}^{p} \qquad \text{Equation 8}$$

$\boldsymbol{\sigma}^{e}\mathbf{:D}^{e}$ represents elastic strain energy that is the time-independent strain energy associated with the pad and wafer; $\boldsymbol{\sigma}^{p}\mathbf{:D}^{e}$ represents viscoelastic strain energy that has time-dependent viscous effects; $\boldsymbol{\sigma}^{e}\mathbf{:D}^{p}$ represents elasto-plastic strain energy that has history-independent, yet time-dependent effects; $\boldsymbol{\sigma}^{p}\mathbf{:D}^{p}$ represents the fully plastic strain energy that has history-dependent and time-dependent effects. Elasto-plastic strain energy accounts for plastic deformation at a constant yield stress, so the previous stress state does not matter. Fully plastic strain energy accounts for plastic deformation where yield stress changes from strain hardening, where the previous stress state is of importance. Determination of the relative contributions that each form of strain energy contributes to dissipation provides important information about the mechanical processes involved in scratching. This analysis is completed through mechanical material characterization experiments for the pad material, as well as knowledge found in the literature for the wafer materials. Plastic damage from scratching of the wafer is accounted for with the plastic forms of strain energy.

Through experimental measurements of mechanical and thermodynamic aspects of the CMP scratching process, the relative magnitudes of each dissipation process can be determined. Equation 5 provides the means to account for each individual dissipation process that occurs in pad scratching. Sources of energy dissipation that are determined negligible in this work include acoustic fluxes, sensible heat flux out of the system, and mass flux of the pad material. The acoustic fluxes that exist in the planarization experiment of pad and wafer contact were inaudible over the equipment on which the experiments were performed. Acoustic power produced at these intensity levels was negligible compared to the input energy of the system. Sensible heat that was generated

and emitted from the pad and wafer contact has been found to be negligible through thermocouple and infrared thermometer measurements of the slurry-covered wafer surface during planarization. The infrared thermometer and thermocouple showed no difference between the temperature of the room and wafer surface temperatures, within an error of ±1.5°C. Mass flux in CMP is dominated by the wafer material as it is planarized when compared to the pad material mass flux. Pad material is removed during diamond conditioning processes that are not considered here. These processes of dissipation are thus considered negligible compared to the processes that include internal energy changes, energy that is associated with wafer mass flux, and strain energies within the pad and wafer. The determination of the relative contributions of these dissipation processes provides an understanding of how energy is transferred through CMP. The resulting information provides an overall improved physical understanding of the process.

3.2 CMP Stress Analysis

To describe the contributions from each form of strain energy, a description of the contact stresses associated with the pad and wafer contact is required. Modeling the stresses and deformations of materials requires relations which describe the materials' physical properties, known as constitutive equations, which provide relations between physical quantities for a specific material. Relationships between stress and strain for wafer materials and the polishing pad are necessary to determine the stress and strain fields associated with chemical-mechanical planarization. Constitutive models which

relate stress to strain may also be a function of quantities including time and temperature. Along with constitutive models of stress and strain, relations which describe a material's change in spatial dimensions under certain deformations are determined. Compressibility of a material is important in determining true stress fields associated with the pad and wafer contact.

3.2.1 Wafer Material Constitutive Modeling

The wafer materials of interest in this work are copper and amorphous silicon dioxide (SiO_2). The integrated circuits (ICs) of today utilize copper as the main conducting material for its low electrical resistance and practicality for manufacturing processes (Li 2008, 734; Steigerwald, Murarka, and Gutmann 1997; Kim et al. 2013, 307-310; Steigerwald et al. 1995, 217-217). Insulating materials used for copper interconnects include silicon dioxide and various low-*k* dielectrics. While low-*k* materials are becoming more prevalent in today's integrated circuits, SiO_2 is still widely used in industry as a standard insulating material (Yanda, Heynes, and Miller 2005; Steigerwald, Murarka, and Gutmann 1997). Silicon dioxide is chosen as the main insulating wafer material to focus on in this work.

Copper behaves as a linear elastic material in quasi-static loading until the material reaches its yield stress (Boyer 1987, 630; Rittel, Ravichandran, and Lee 2002, 627-642; Sumigawa et al. 2010, 6040-6047; Zhang et al. 2011, 1497-1502), which is between 60 MPa and 800 MPa, depending on how the material is produced. Copper that is produced in bulk has a yield stress between 60 MPa and 300 MPa. Through various

mechanical testing methods in the literature, the yield stress of thin film copper has been found to be larger than that of bulk copper (Sumigawa et al. 2010, 6040-6047; Zhang et al. 2011, 1497-1502; Xiang, Tsui, and Vlassak 2006, 1607-1618; Volinsky et al. 2001, Q5; Wei et al. 2007, 541-544). This material strengthening is a result of dimensional and microstructural constraints that occur within thin films. Depending on the integrated circuit design, metal and dielectric layer thicknesses can range from 10 nm to 1000 nm (Atanasova et al. 2013, D3255-D3259; Lim et al. 2014, 1255-1261; Dubreuil et al. 2010, 421-425). Thus, the yield stress of electroplated copper wafer material is larger than that of standard bulk copper. Analysis of electroplated copper thin film grain structure shows that the copper grains are randomly distributed with numerous crystal orientations (Xiang, Tsui, and Vlassak 2006, 1607-1618; Volinsky et al. 2001, Q5; Wei et al. 2007, 541-544). This information permits the assumption that copper wafers are homogeneous materials. As thin films have microstructural constraints as previously mentioned, thin films are not particularly isotropic. Yet, it is reasonable to assume isotropic material behavior for copper wafers when approximating stress fields.

Silicon dioxide (SiO_2) is typically deposited using chemical vapor deposition (CVD), which results in an amorphous film of the material (Yanda, Heynes, and Miller 2005; Thagella 2004, G205-G215; Ju and Goodson 1999, 7130-7134). Silicon dioxide thin films have been mechanically tested through tensile and indentation methods in the literature. Quasi-static tensile tests of 1 um thick samples of silicon dioxide show linear stress-strain behavior until fracture (Gianola and Sharpe Jr. 2004, 23-27; Sharpe Jr. et al. 2007, 649-658). Fracture occurs between 300 MPa and 500 MPa of tensile stress which is nearly 0.6% strain. Indentation experiments on 2 um thick silicon dioxide films

show yield conditions through multiple indentation tip geometries (Cao and Zhang 2008, 1941-1951). The equivalent indentation stress reported is the average stress computed from the applied load divided by the contact area. At yield, the indentation stress and strain are no less than 3 GPa and 10%, respectively. Before SiO_2 yields, the stress and strain have a linear relationship. Below the yield stress, it is assumed that silicon dioxide behaves as a linear elastic material. Also, CVD silicon dioxide films are homogenous as the deposited film is amorphous. The same assumption for isotropic silicon dioxide films is made which provides approximations of the actual stress fields.

The constitutive equation for homogenous isotropic linear elastic materials, also known as Hooke's Law, is given in Equation 9 (Sadd 2009),

$$\sigma_{ij} = \frac{E\nu}{(1+\nu)(1-2\nu)} e_{kk}\delta_{ij} + \frac{E}{1+\nu} e_{ij} \qquad \text{Equation 9}$$

The Cauchy stress tensor is σ_{ij}, assumed to be symmetric, e_{ij} is the infinitesimal strain tensor, δ_{ij} is the Kronecker delta, E is the elastic modulus, and ν is the Poisson's ratio. E and ν are properties that describe the mechanical behavior of a specific linear elastic material. The elastic modulus for bulk and thin film copper is typically between 70 GPa and 160 GPa (Rittel, Ravichandran, and Lee 2002, 627-642; Sumigawa et al. 2010, 6040-6047; Zhang et al. 2011, 1497-1502; Xiang, Tsui, and Vlassak 2006, 1607-1618; Volinsky et al. 2001, Q5; Brandes and Brook 1992, 14-6). Poisson's ratio for bulk and thin film copper is about 0.34 (Sadd 2009; Brandes and Brook 1992, 14-6; Lee et al. 2009, 51-54). The elastic modulus of bulk and thin film amorphous SiO_2 is between 55 GPa and 75 GPa (Gianola and Sharpe Jr. 2004, 23-27; Sharpe Jr. et al. 2007, 649-658; Cao and Zhang 2008, 1941-1951). Bulk amorphous SiO_2 has a Poisson's ratio of about

0.17, while thin film SiO_2 can reach a value up to 0.25 (Carlotti, Doucet, and Dupeux 1997, 102-105; Tsai and Fang 2003, 377-383). These wafer materials behave linearly elastically until their yield stress is reached. It is at this point where plastic deformation and thus damage is produced in the material.

3.2.2 Polishing Pad Constitutive Modeling

The most commonly used polishing pad during CMP of copper interconnects is known as IC1000 (Eusner, Saka, and Chun 2011, H379-H389; Kim, Saka, and Chun 2014, P169-P178; Kim, Kim, and Jeong 2000, 945-951; Kim et al. 2008, 454-463), which is a porous polyurethane foam manufactured by casting the liquid polymer into a circular mold (Steigerwald, Murarka, and Gutmann 1997; Jairath et al. 1994, 121-131). The literature has shown this material is mechanically time dependent (Kim, Kim, and Jeong 2000, 945-951; Kim et al. 2008, 454-463; Ludwig and Chaves 2011, 2264-2267; Borucki 2002, 105-114). Thus, the rate at which strain or stress are applied along with the past mechanical history of the material are of importance in the pad's constitutive model.

Many works in the literature characterize the mechanical behavior of IC1000 using stress relaxation experiments and dynamic mechanical analysis (DMA). Such experimental methods provide information on the time dependent behavior of IC1000. The literature which states the mode of deformation used of pad mechanical experiments mainly utilize tension or bending (Li et al. 1995, 601-606; Borucki 2002, 105-114; Zantye et al. 2003, 183-190; Li et al. 2000, E7-E7; Lu, Obeng, and Richardson 2002,

177-186). In these modes of deformation, the bulk mechanical behavior is measured. In CMP, the pad operates in compression from the applied normal force, as well as shear from relative velocity of the pad and wafer. For the compression aspect of deformation, the rough surface of the pad contributes to the mechanical behavior (Tichy et al. 1999, 1523-1528; Luo and Dornfeld 2003, 45-56; Castillo-Mejia et al. 2003, G76-G82; Runnels, Miceli, and Kim 1999, 4619-4625; Fan et al. 2010, H526-H533). The pad surface is relatively rough compared to wafer surfaces so that the overall compressive stiffness of the pad acts similar to two viscoelastic materials in series. The asperity layer behaves as a softer material since the real area of contact is much smaller than the nominal contact area with initial loading of the asperity tips only. Experimentally, the compression modulus of IC1000 has been shown to be up to two orders of magnitude less than the modulus in tension (Kim et al. 2008, 454-463). This is a result of the asperity layer not being directly involved in supporting the applied load in tension or in bending. Also, the porous polymer structure of the polyurethane foam may behave differently in compression than in tension. It is thus important to model the compressive mechanical properties of the pad material to account for the complex behaviors of the asperity layer and porous internal structure. Further, there is no information in the literature to date, which provides the typical experimentally measured compressive strains which occur on the pad material during CMP. In this work, a constitutive mechanical model for the IC1000 pad in compression is constructed. This model accounts for time dependent behaviors through a range of applied pressures that occur in CMP.

Along with the mechanical constitutive model for the IC1000 pad, information about the kinematics of the material is necessary for proper stress field modeling. The true stress, or Cauchy stress is computed using Equation 10 (Lai, Rubin, and Krempl 2010),

$$\boldsymbol{\sigma} = \frac{1}{J}\boldsymbol{P}\boldsymbol{F}^{\boldsymbol{T}} \qquad \text{Equation 10}$$

P is the first Piola-Kirchhoff stress tensor, **F** is the deformation gradient tensor, and J is the Jacobian of the deformation gradient tensor. The Cauchy stress describes the load that is applied to a differential area in its deformed state (Lai, Rubin, and Krempl 2010). Piola-Kirchhoff stress describes the stress based on the un-deformed area, similar to engineering stress. **P** is typically known, as the initial undeformed area is easily measureable. Computation of Cauchy stress requires knowledge of the deformation of the continuum, which is given through **F** and J. The Jacobian is a measure of the change in volume of the material, given in Equation 11 (Lai, Rubin, and Krempl 2010),

$$J \;=\; |Det\,\boldsymbol{F}| \;=\; \frac{d\mathcal{V}}{dV_o} \qquad \text{Equation 11}$$

$d\mathcal{V}$ is the deformed volume and $d\mathcal{V}_o$ is the un-deformed volume. The way in which a material deforms and changes volume is specific to each material. Thus, the Jacobian of the IC1000 pad material in compression is found to allow for computation of the true stress in the polishing pad.

The polishing pad material used in all experiments is a Rohm and Haas IC1000 A2 pad (Rohm and Haas Co., Philadelphia, PA). The IC1000 pad also has a softer subpad which never contacts the wafer material. Under the subpad is adhesive used to

attach the pad to the polishing machine being used. For experiments used to characterize the IC1000 pad only, this subpad is completely removed. This current work is concerned with the mechanical behavior of the material that is in direct contact with the wafer, as the IC1000 pad directly induces the stresses on the wafer. An image of the pad surface is presented in Figure 11. It consists of squares that are approximately 0.22 inches by 0.22 inches. Including the larger groove width, the squares are approximately 0.25 inches by 0.25 inches. Each square has three to four smaller diagonal grooves across them that are approximately half as deep as the larger grooves. The major thickness of the pad is approximately 0.050 inches while the smallest thickness, that does not include the grooves, is about 0.020 inches.

Figure 11: IC1000 Polishing Pad Surface

3.2.2.1 IC1000 Pad Compressive Stress Relaxation

A mechanical description of the IC1000 pad material behavior during CMP is crucial in accurately modeling the contact stresses between the pad and wafer materials.

To characterize the compressive mechanical behavior of the pad, compression relaxation experiments are conducted. These experiments reveal the time dependent and stress magnitude dependent mechanical behavior of the IC1000 pad in compression. A relaxation experiment applies strain to the material, which is held constant, while the resulting load is measured over time. The nominal stress of the material is computed to observe trends with time through a range of initial stress values. Pad samples in numerous conditions are also tested, including used pad material. Resulting time and stress magnitude dependent relaxation of the material is obtained.

The pad's relatively small thickness of 0.05 inches provides a challenge to measure displacements accurately on the magnitudes of deformation that occur in CMP. The IC1000 pad has a bulk quasi-static elastic modulus on the order of 100 MPa or 14500 psi (Castillo-Mejia et al. 2003, G76-G82). The literature also states that the equivalent asperity layer elastic modulus is on the order of 1 MPa or 145 psi (Kim et al. 2008, 454-463). With a typical applied normal pressure of 4 psi in CMP (Chandra et al. 2008, 559-562; Armini et al. 2007, H667-H671), the level of strain can reach 3% using the asperity layer elastic modulus. With the pad's thickness of 0.05 inches, this strain results in a displacement of only 0.0015 inches in compression. A typical universal testing machine does not have the displacement resolution to accurately measure these expected strains.

To accurately apply and measure the small displacements that are predicted from CMP loading conditions, a custom compression testing setup is designed and fabricated. The compression setup is pictured in Figure 12. It consists of a Newport Corporation SM-50 Vernier micrometer (Newport Research Corp., Irvine, CA) which provides the

means to introduce displacement to the system by translating the displacement block. This block is secured to the angle bracket to maintain its front face square to the base plate. The pad sample tested is placed between the displacement block and the compression block. A 5 kg load cell (Phidgets, Calgary, Alberta, Canada) is secured to an aluminum fixture. This load cell is used to measure the load that is applied to the pad sample as the displacement and compression blocks are forced together with the micrometer. Strain measurements of the pad sample are performed by measuring the change in distance between the blocks with digital images. A Leica DMLB microscope (Leica Microsystems Inc., Bannockburn, IL) with a mercury lamp is used to provide proper optical magnification and lighting. A Watec WAT-902A CCD camera (Watec, Newburgh, NY) with Osprey SwiftCap software (Osprey by Variosystems, Southlake, TX) are used to capture video of the top edges of the blocks. The resulting images are in a grayscale format with a 600 pixel by 400 pixel resolution. MATLAB Imaging Processing Toolbox (Mathworks, Inc., Natick, MA) is used to measure the change in distance between the two blocks from the images taken during the compression.

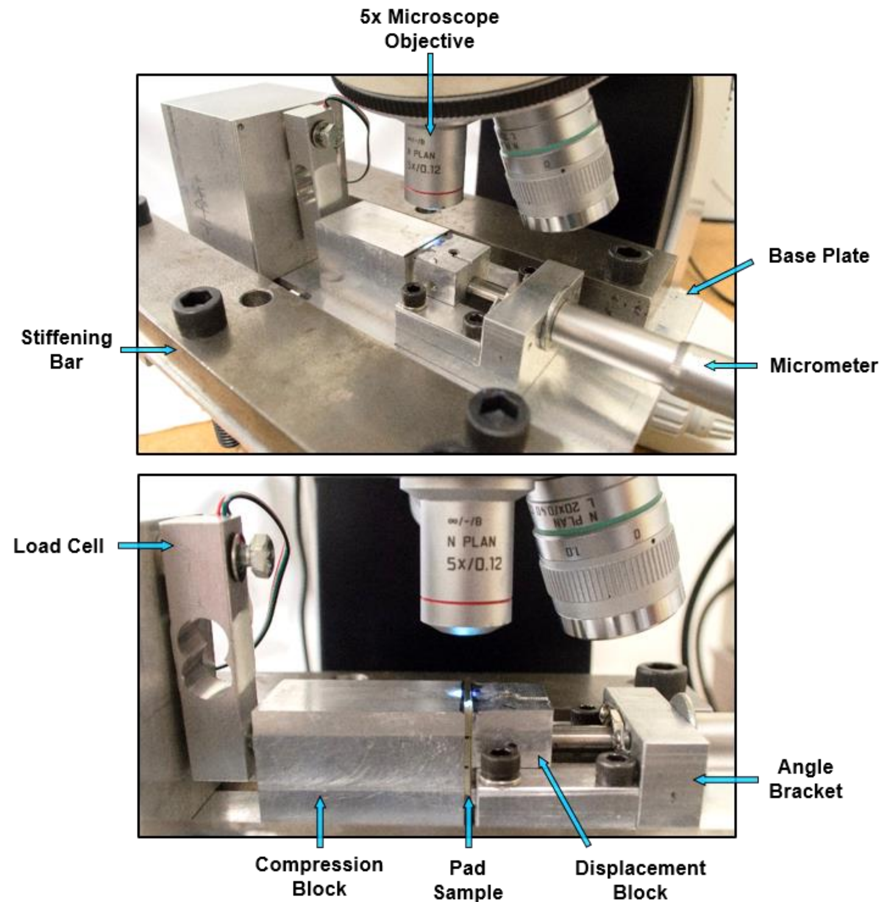

Figure 12: Compression Test Setup

Each contact face is machined to be square with the base plate so that displacement and load are evenly distributed across the pad sample. The compression block is not secured and is floating with respect to the load cell and displacement block. This compression block is required in the setup to separate the pad sample from the load cell so that the microscope objective can properly observe the block edges. As the compression block is floating, it self-aligns to the pad sample face when load is applied. The load cell is initially aligned by forcing the load cell, compression block, and displacement block together while tightening the load cell's fixture secure. Placement

of the load cell contact point with the compression block is set to be in line with the center of the sample material so moments are not produced. Steel bars are secured to the aluminum base plate to provide rigidity to the system so that the base plate does not bend under load.

Errors associated with this system in itself include the system compliance, which may displace the components so the block and load cell faces are no longer parallel. This has the potential to provide error in the strain measurements as the strain is not evenly distributed across the pad sample. Other errors are associated with the random digital noise from the camera sensor, analog to digital signal noise of the load cell measurements, and time dependent relaxation of the system.

Load cell analog signals are amplified and digitally converted with a PhidgetBridge interface board (Phidgets, Calgary, Alberta, Canada). This hardware is used in conjunction with LabView (National Instruments, Austin, TX) to record the load cell output over time. The load cell is calibrated using a range of weights with masses between 20 mg and 2 kg. A linear regression of the data is performed to provide a relation between the load cell output and actual force values. This regression is performed using MATLAB's *polyfit* function. The resulting linear fit has a coefficient of determination equal to one when rounding to five decimal places. This indicates a very good linear fit and accurate calibration. The manufacturer states that the load cell has a creep value of 0.01 lb_f per hour and a repeatability error of ± 0.006 lb_f.

Strain measurements are conducted using MATLAB's Image Processing Toolbox. A video is taken of the top edges of the blocks during compression, between which the pad sample is compressed. A single still image of the block edges is presented

in Figure 13. The grayscale images from the video are placed through a black and white filter. The threshold brightness value between black and white is chosen to properly extract the edges of the blocks. To account for unaligned edges relative to the camera sensor, a linear regression is performed along the pixels of the lower block edge. The resulting linear slope is used to rotate the image at the proper angle to align the block edge parallel to the image's x-axis.

Figure 13: Example Image of Block Edges.

Left: Initial Grayscale Image. Right: Black and White Processed Image for Strain Measurement.

To measure strain, the number of pixels between the block edges are measured and averaged for each video frame. A frame which represents zero strain on the pad sample is chosen for the initial number of pixels. The remaining pixel counts for each frame are compared to the initial number to acquire a measure of strain. The MATLAB code which imports and processes the video frames for strain measurements is provided in the Appendices under MATLAB Code for Strain and Stress Analysis of Compression Relaxation. This code also imports load data acquired simultaneously with the video. The video is set to capture at a rate of 25 frames per second; the load cell captures data

at the same rate. Syncing the load and strain data provides a means to acquire trends of stress versus strain.

The 5x objective on the microscope is used as it provides the necessary field of view to observe the block edges. Using a distance calibration slide, the field of view is determined to be 1.36 mm x 2.04 mm, with a resolution of 0.0034 mm per pixel. Error associated with the random noise of the digital image sensor is quantified by taking a video of the still block edges under no applied load. The video is taken for 30 seconds to account for the longest amount of time that a video is captured. The distance between the block edges are measured over time through image processing with MATLAB. The edges are separated by the initial pad thickness. The digital image noise in strain over time is computed to vary by $\pm$ 0.02% strain.

This setup allows for the instantaneous measurement of load as it appears on the LabView interface. Yet, what is input to the system is displacement from manually turning the micrometer. Thus in running the experiments, displacement of the pad samples is input by turning the micrometer until a desired peak load is achieved. When this peak load is reached, the micrometer is released. The loading rate is applied as uniformly as possible at constant rate. The loading process is timed to take approximately 5 seconds from initial load measurement to peak load. Constant loading rate and time of loading are desired to be kept constant to remove potential variations between trials. Varying these parameters may introduce unwanted nonlinear behavior when comparing data between trials. Since these parameters are manually controlled, errors are introduced from these potential variations.

Relaxation compression experiments are conducted on the pad material using the constructed compression test setup. To perform these experiments, a pad sample is placed between the compression and displacement blocks. The compression block is lightly pushed against the pad material so that the friction between the pad and block faces holds it in place. The controlled variables in these compression experiments are the peak load, pad sample area, and variations in condition of the pad samples. The pad samples vary with condition from a new pad, used pad, or a pad that has been soaked in slurry or distilled water. These variations allow for mechanical characterization of the pad sample through different stages of the pad's service life and duty cycles. The peak load and pad sample area are chosen to fall within the range of loads that the load cell can measure while covering the range of peak stresses to be tested. Compressive stresses that occur in CMP are on the range of 1 psi to 7 psi (Chandrasekaran et al. 2004, G882-G889). Experiments are run to cover this range of peak stresses, while focusing more on the most typical pressure in CMP of 4 psi. Pad samples used have a nominal area of 0.375 inches or 0.1875 inches. The result of these experiments is the stress relaxation behavior over time at a range of peak loads for various conditions of the pad material. These measurements provide information to mechanically characterize the compressive stress behavior of the IC1000 polishing pad in CMP.

3.2.2.1 IC1000 Pad Compressibility

The Jacobian of the pad material in compression is estimated using the same compression test setup for the stress relaxation experiments, but without the load cell. The compression block is compressed flat against the load cell fixture as load

measurements are unnecessary for compressibility measurements. This experiment tracks volume change of a pad sample through a range of compressive strains. Samples of IC1000 pads of approximately 0.06 inches by 0.06 inches are cut from the 0.05 inch thick IC1000 pad using a sheet metal shear and a single-edge razor. This pad sample size is chosen based on the largest block of material that can be cut to not include any grooves. The resulting sample is a solid block of pad material with no groove separation for ideal volume measurement as it is being compressed. Since the sample's area that is being compressed is approximately square, the volume of the sample can be estimated as the thickness multiplied by the width squared. The face that is being measured will behave in the same manner as the faces which are unseen.

The pad sample is placed between the compression plates and then slightly loaded so that the sample holds its weight with friction. As the compression plates are displaced together with the micrometer at a relatively constant rate, a video of the top face of the pad and edges of the compression blocks is recorded. The grayscale video is taken at 20 frames per second for the approximate 15 second duration of compression. Each experiment compresses the pad to approximately 15% to 20% compressive strain. An example image taken from an experiment's video is seen in Figure 14. It has to be ensured that there is good contrast between the pad sample, plate edges, and background to easily isolate the sample using the MATLAB Image Processing Toolbox. A code is created which measures the thickness and average width of the pad sample face for each frame, and is provided in the Appendices under MATLAB Code for Compressibility Measurements of the IC1000 Pad. This code places the video frames through a binary image filter with a constant threshold value for each respective video. Setting this

constant threshold value provides consistent results of distance measurements for a single experiment. An example of the isolated binary image of the pad sample from Figure 14 can be seen in Figure 15. After the sample is isolated, a linear regression is applied to a portion of edge points that represent the compression block edge. A linear regression is used to acquire an angle to rotate the pad sample for alignment of the compression plate faces parallel to the image's x-axis.

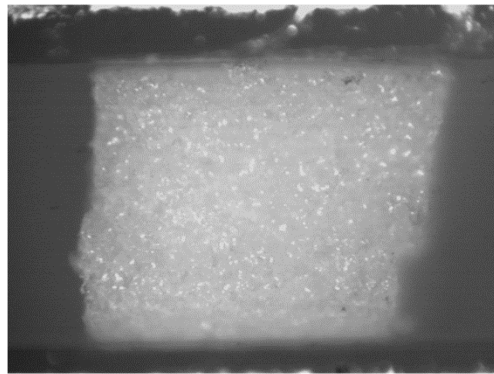

Figure 14: Grayscale Image of Pad Sample before Compression

Figure 15: Binary Image of Isolated Pad Sample with Linear Regression for Rotation

The thickness and width of the sample is measured along each row of the image. For the found width values, the magnitudes are compared to the maximum width found. If a width value is less than 80% of the maximum, it is discarded. This provides more consistent results as the edges of the binary pad image are prone to changes in light reflection with each frame. Additionally, plate edges may reflect light in various directions as the pad sample is compressed. The remaining values of width are then averaged to provide the width measurement of that video frame. Thickness is taken as the average value of distance between the compression block edges.

Volume of the sample is calculated as the average thickness times the average width squared. This computation assumes that the pad sample expands the same into the image as the measured width. Thus, errors are introduced with samples that are not perfectly square. Example images of the initial pad sample and fully compressed sample are seen in Figure 16. To compare the volume to the amount of compression, the compressive strain of the pad sample for each frame is computed. The MATLAB code plots a figure of strain for each video frame so the user can choose to omit the video frames at the beginning and end, during which compression is not occurring. The Jacobian is estimated by dividing the current volume for the current image by the original volume from the chosen first frame. The Jacobian is plotted against compressive strain and a linear regression is applied with MATLAB to acquire a numeric relationship between both variables.

Figure 16: Rotated Binary Images of Pad Sample. Left: Uncompressed. Right: Fully Compressed.

The dimensions of the pad samples are measured to determine how close each sample is to a rectangular block. Dimensions measured are the width and height of the pad sample's compressed face. An example of a pad sample is seen in Figure 17. These measurements are manually completed using the command *imtool* in MATLAB to provide estimates. To measure how close the compressed face is to a square, the height and width measurements are compared. Also, the measured width values from the videos are compared due to variations in these dimensions from left-over groove features from the pad when the samples were cut. It can be seen that a part of the groove on some of these pad samples is left over, such as on the bottom right of the sample in Figure 14.

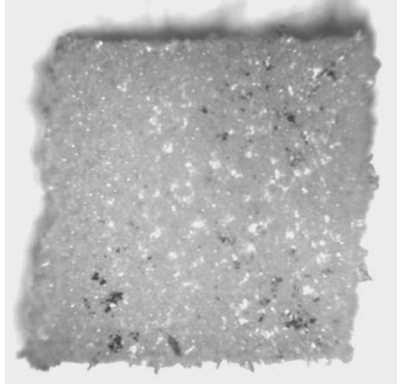

Figure 17: Pad Sample for Compressibility

The largest deviation from a 1.00:1.00 aspect ratio from a single sample is 1.00:0.88. The average for all samples is an aspect ratio of 1.00:0.93. From measurements of width using the captured videos, it is found that the largest percent change in width due to the grooves is approximately 19%. On average for all samples this value is 12%. With these relatively small deviations in the assumed sample geometry, the experiments provide reasonable approximations.

Another source of error in this experiment is that the sample materials also have friction acting on the faces in contact with the compression plates. The pad samples are not in pure compression, but have a more complex deformation through the experiment. Thus, the measured Jacobian is not for pure compressive deformation only. This experiment provides an approximation of the Jacobian of the pad material under compressive displacements. The information provided through these methods is useful for approximate analysis of true stresses in IC1000 polishing pad material.

Other parameters which describe the compressibility of materials are also computed. These parameters include the Poisson's ratio and the dilatation, or trace of

the infinitesimal strain tensor. The Poisson's ratio is a parameter which describes the constitutive behavior of an elastic material. It is defined in Equation 12 (Sadd 2009),

$$\nu = -\frac{d\varepsilon_{trans}}{d\varepsilon_{axial}} \qquad \text{Equation 12}$$

ε_{axial} is the strain along the compressed direction of the material and ε_{tran} is the transverse strain, or the strain along the width of the sample. When ν is equal to 0.5, the material is incompressible for the small strain assumption of linear elastic theory (Lai, Rubin, and Krempl 2010). To approximate the Poisson's ratio, a linear regression is applied to the axial and transverse strain data. The resulting slope of the linear regression results is the approximation for Poisson's ratio from the experimental data.

Dilatation is a measure of compressibility that is formed using the strain tensor (Lai, Rubin, and Krempl 2010). Consider a differential rectangular volume that has an initial volume of V_o, given in Equation 13,

$$V_o = dx_1 dx_2 dx_3 \qquad \text{Equation 13}$$

dx_1, dx_2, and dx_3 are the lengths of each side. The edges are oriented to point in the direction of principal strain. When the differential volume is strained, the change in volume from the initial volume is represented in Equation 14 as ΔV,

$$\Delta V = \big((1+E_1)(1+E_2)(1+E_3) - 1\big) dx_1 dx_2 dx_3 \qquad \text{Equation 14}$$

E_i represents the principal strains. To relate this to the dilatation, the change in volume is normalized to the original volume, given in Equation 15,

$$\frac{\Delta V}{V_o} = (1 + E_1)(1 + E_2)(1 + E_3) - 1 \qquad \text{Equation 15}$$

If all second order or higher terms are removed from Equation 15, the result is the dilatation of the infinitesimal strain tensor e_{ij}, in Equation 16,

$$\frac{\Delta V}{V_o} = e_1 + e_2 + e_3 = e_{ii} \qquad \text{Equation 16}$$

The dilatation is also known as the trace of the infinitesimal strain tensor in the principal orientation. This is the case, as removing the higher order terms assumes small strains. With experimental data, the change in volume of the pad sample with respect to the original volume is computed using Equation 15 and compared to the small strain assumption of dilatation in Equation 16.

3.2.2.2 Tensile Characterization of IC1000 Pad

To analyze the bulk properties of the IC1000 pad, mechanical tensile testing is conducted on the pad material. An Instron 3345 universal testing machine (Instron, Canton, MA) with screw action grips is used to conduct quasi-static and stress relaxation tensile tests on polishing pad samples. Strain is measured using the measured crosshead displacement of the Instron machine. This method of strain measurement is determined to be reasonable through compliance testing of the Instron machine and grips. A steel bar that is 1.5 inches wide and 0.62 inches thick is tensile tested with a gauge length of about 0.05 inches. The bar is pulled at a constant displacement rate of 0.001 inches per second. This steel bar has a stiffness of approximately 5.5 x 10^8 lb_f/inch, which is found using its geometry and the elastic modulus of steel. The bar is much stiffer than the

Instron machine itself, based on manufacturer's information, which has a stiffness of about 4.5 x 10^4 lb_f/in. The minimum stiffness of the entire loading system is measured based on tensile testing the steel bar, since the displacement of the system will be mainly from the Instron machine and its grips. Additional displacement may take place due to slippage of the steel bar in the grips. The system stiffness may be underestimated from this slipping, so these experiments provide conservative error estimates.

Stiffness of the testing system is computed from the steel bar tensile test load and force data. A figure of load versus displacement for tensile testing of the steel bar is shown in Figure 18 for all three trials performed. Linear regressions of this data are computed up to 0.005 inches of extension to remove potential nonlinearities from slipping of the steel bar on the grips. The minimum stiffness value of all three trials is computed to be 22,000 lb_f/inch.

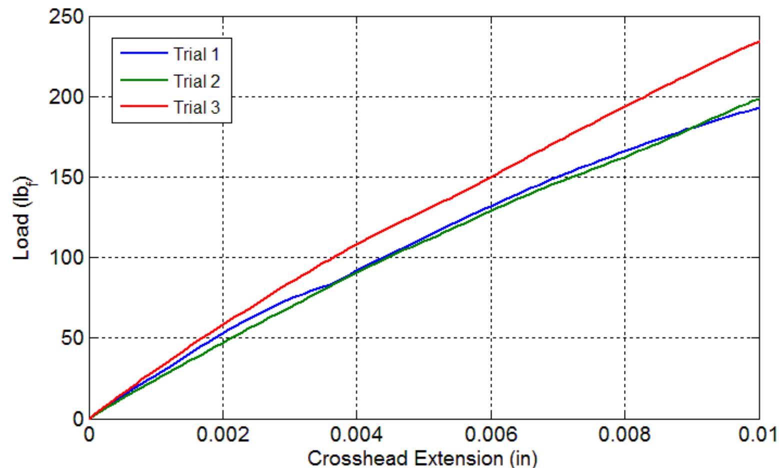

Figure 18: Load versus Crosshead Extension for Tensile Compliance Testing

To compute the error associated with strain measurements of the pad samples to be tested, their typical stiffness is required. Pad samples tested have a gauge length of 4 inches and a width of 1 inch. The thickest part of the pad material is about 0.05 inches while the thinnest part is about 0.02 inches. An average thickness of 0.035 inches is used. From the performed quasi-static tensile experiment, the elastic modulus of the pad material was found to be approximately 19.1 x 10^3 psi based on a 0.035 inch thickness. This value is reasonably close to the values found within the literature for the IC1000 elastic modulus. Based on the stiffness of this sample and the system stiffness of 22,000 lb_f/inch, the error in the extension of the pad sample is found to be 0.75% of the measured value. This error is considered to be small and acceptable for tensile tests of the pad material. For load measurement errors, the Instron machine's load cell is accurate to ± 0.5% of the reading down to 1/100 of the load cell capacity of 1,125 lb_f.

A sample of pad material is cut to provide a 4 inch gauge length and a 1 inch width for each stress relaxation experiment. The quasi-static tensile test pad sample had a width of 0.75 inches. The experimental setup for these experiments is shown in Figure 19. The grooves of the pad are oriented parallel along the length of the sample, with the direction of applied load. These grooves provide a challenge for tensile testing in terms of accurate stress measurements. Grooves will introduce stress concentrations in the thinner sections of the pad. To attempt a reasonable approximation of stress, an average of the thinnest and thickest section of the pad is used for the average cross sectional area, which is 0.035 inches.

Figure 19: Tensile Experimental Setup for the IC1000 Pad

Just before running an experiment, the Instron machine's load cell is zeroed before the pad sample is set in the grips. The Instron machine is set to slowly apply displacement until load just begins to increase. At this point, the gauge length of the sample between the grips is measured with calipers. For the quasi-static tests, the machine is set to pull at a rate of 0.002 inches per minute and the experiment is ended after approximately 50 minutes. Relaxation tests apply displacement at a linear rate until the desired strain level is achieved at a constant 0.6 seconds for each trial. This time is chosen based on the maximum speed that the Instron machine can pull for the maximum holding strain desired. Trials are run for constant strains of 0.25%, 0.50%, 1.0%, 1.5%, 2.5%, and 5.0%. After the strain is applied, the load is measured over time for 16

minutes. This time is recommended for stress relaxation experiments by the universal testing machine manufacturer.

3.2.3 Contact Stresses in Scratch Generation

An analysis of the contact stresses between the pad and wafer materials is conducted to reveal the relative importance of the strain energy terms in the thermomechanical model. The analysis encompasses the constitutive behaviors of the pad and wafer material along with the geometry of the contact. Average surface roughness of the IC1000 pad is two orders of magnitude larger than the wafer material surface (Kim, Saka, and Chun 2011, 393-404; Lay and Duquette 2006, 1-9; Nasrullah, Tyler, and Nishi 2005, 303-311). With the much smoother wafer surface relative to the polishing pad, it is assumed that the wafer is a flat elastic half-space in contact with the asperities of the pad. To analyze local contact stresses, the stresses associated with a single pad asperity in contact with a flat elastic half-space is used as the contact model. Pad asperities are assumed to be spherical. An image that illustrates the steps of pad and wafer contact with scratching is shown in Figure 20. The first step is an initial point contact onto the wafer surface by a single asperity, as the wafer is loaded onto the pad. The pad asperity deforms into the wafer with additional normal pressure. As the pad and wafer move relative to each other at velocity, the stresses in the wafer surface increase due to tangential tractions from friction. For scratching to occur, the stresses in the wafer become large enough that the pad asperity plastically yields the wafer material. As the pad continues to move relative to the wafer, the asperity ploughs

through the wafer to form a scratch. The focus of this contact stress analysis is the determination of failure criteria in which the pad asperity plastically yields the wafer.

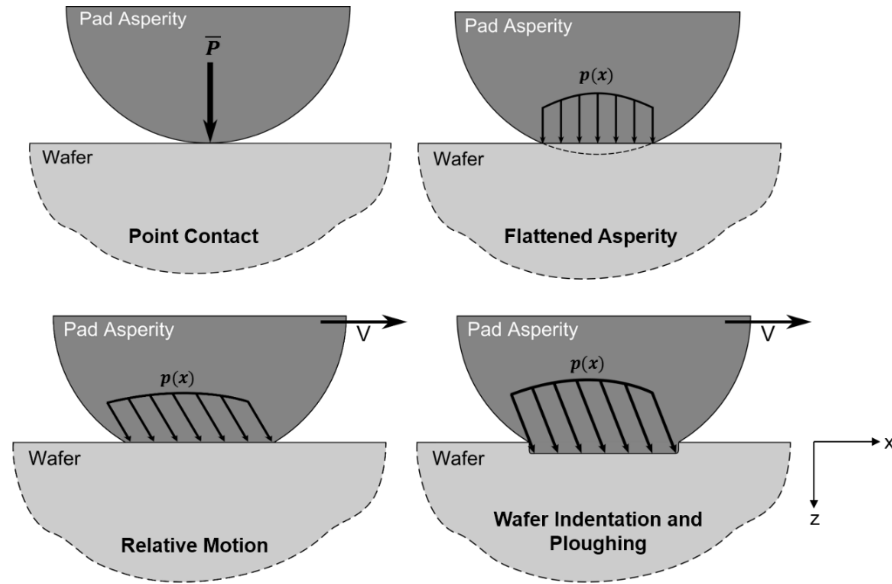

Figure 20: Evolution of Pad Asperity and Wafer Contact

A Hertzian contact is commonly used to model the stresses associated with a circular asperity contact. Assumptions made with this type of contact include that the strains are small, each solid is considered an elastic-half space, and the surfaces are frictionless. These assumptions are not necessarily appropriate as the strains in the relatively soft pad asperity may exceed what is considered small, since the pad is relatively soft compared to the wafer. The polishing pad stresses are time dependent and may also plastically deform, thus it is not necessarily elastic. Also, the contact is not frictionless since tangential tractions are required to remove material from the wafer surface in polishing.

Work has been done in the literature to model the single pad asperity contact with the wafer half-space using a modified Hertzian contact (Kim, Saka, and Chun 2014, P169-P178; Hamilton and Goodman 1966, 371). This solution combines a Hertzian normal contact pressure distribution with a tangential traction distribution that is proportional to the normal force using the coefficient of friction. Using this contact pressure solution, a function for the von Mises stress of the wafer is determined. This provides a yield criteria for scratching the wafer when comparing von Mises stress to the wafer yield stress. Along with friction, the model also accounts for plastic deformation of the pad asperity using a uniform pressure distribution. In this work, the stress field analysis is expanded upon to account for mechanical time dependency and dissipation processes due to friction.

3.3 Chemical-Mechanical Planarization Experiments

Numerous experiments are conducted in the current work to obtain data that is essential for construction of the thermomechanical model. The central experiment conducted in this work replicates the process of chemical-mechanical planarization. Polishing pad and wafer materials are loaded and translated against each other with CMP slurry as a lubricant. The pad and wafer contact are set to travel distances equivalent to a number of wafers polished. During these experiments, forces transmitted between the pad and wafer materials are monitored. Measured force values allow for computation of the tractions applied between the pad and wafer. Tractions that are

transmitted between the materials during CMP are needed for accurate stress field computations, input energy values, and evolution of the mechanical contact in time.

Upon completion of the planarization experiments, the acquired polishing pad and wafer materials are experimentally analyzed through various methods. Wear of the wafer materials are analyzed through measurements of sample mass before and after planarization. Surface topography of the materials are measured with a profilometer before and after planarization for information about the geometrical transformation of pad and wafer surfaces. Worn pad material is thermodynamically analyzed using differential scanning calorimetry (DSC) to track potential internal energy changes of the polyurethane pad material. Additionally, worn pad material is mechanically tested to track the mechanical behavior of the IC1000 pad through CMP.

3.3.1 Planarization Experiments

It is important to reproduce the chemical-mechanical planarization process to gather the necessary mechanical and thermodynamic data for the model being constructed. The equipment must be able to apply normal pressure between the IC1000 polishing pad and wafer materials while applying a relative velocity between the surface contacts. These pressures and velocities must be of the same magnitude used in CMP. Contact forces between the pad and wafer materials must also be measured during the entire polishing process. The most important direction of force measurement are normal to the contact and in the direction of translation. For analysis of thermodynamic,

topographical, and wear of tested materials, the equipment must also allow for sampling of polishing pad material at intervals of experimentation.

To fulfill the requirements of experimentation, a reciprocating linear tribometer, fabricated in-house, is used to conduct the planarization experiments. An image of the tribometer that is implemented for these experiments is shown in Figure 21. The tribometer uses an igus DryLin ZLW-1040-LCB linear belt drive table (igus, East Providence, RI) that is powered by a Parker RS33B-SNNPS stepper motor (Parker Hannifin Co., Mayfield Heights, OH). The stepper motor is controlled with a Parker ZETA6000 controller system coupled with an Arduino interface (Arduino, Somerville, MA). Average velocity of the table is measured by timing the motor's running signal with an Arduino interface. This time is compared to the distance traveled per motor step, which is calibrated with a dial indicator to the thousandth of an inch.

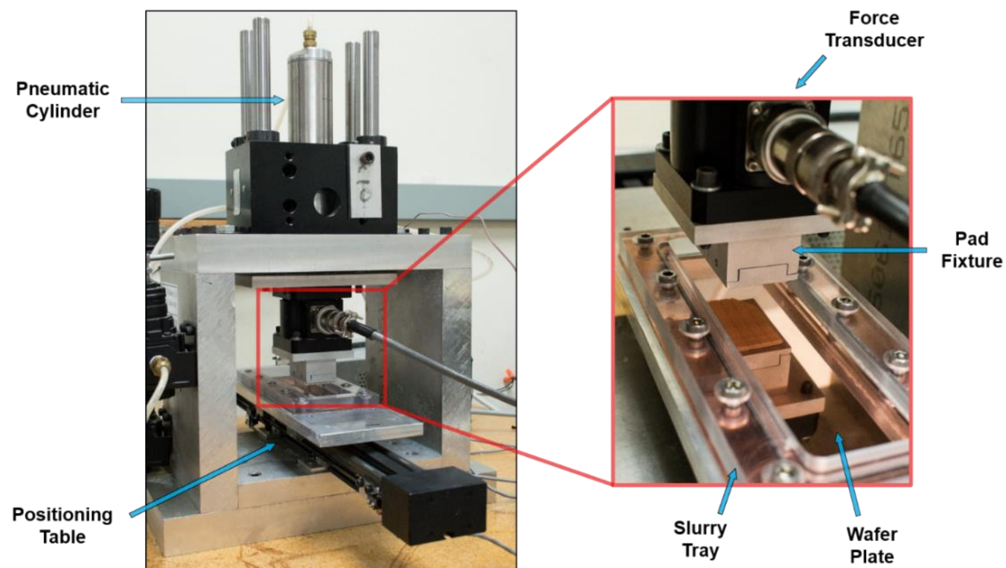

Figure 21: Reciprocating Linear Tribometer

The wafer material is fixed to the reciprocating table for the pad material to articulate against. A slurry tray is used to hold the wafer material to the table as well as to contain a layer of slurry on top of the wafer plate. The polishing pad is secured to the force transducer with the adhesive backing of the IC1000 pad onto a flat load cell plate fixture, seen in Figure 22. The fixture allows for the pad material to be cut from the plate for intermediate material analysis at various polish times. This is made possible as the plate is held with set screws so that the pad sample can be centered in the load path after a piece has been removed. The polishing pad material is loaded onto the plate of wafer material at the proper pressure using a pneumatic cylinder. Load is applied from the pneumatic cylinder to an AMTI MC3A-6-250 Dynamometer (Advanced Mechanical Technology Inc., Watertown, MA) that measures the contact forces and moments acting on the contacting materials. The force transducer's voltage outputs are amplified by an AMTI MSA-6 MiniAmp using a gain of 1000 and a bridge excitation of 10 V. LabView is used to control the number of cycles the table reciprocates and also records the force transducer output.

Figure 22: Polishing Pad Tribometer Fixture

The polishing pad material used is a Rohm and Haas IC1000 A2 pad with a softer subpad. The slurry used is the Dow ACuPLANE LK393C4 (The Dow Chemical Co., Midland, MI). This slurry is a typical copper interconnect CMP slurry with colloidal silica abrasive particles of 0.050 um average diameter (Eminess Technologies, Scottsdale, AZ). The wafer materials used in these experiments are 99.99% pure copper plates, and 99.99% pure fused silica plates. For the copper wafer material, copper plates of 0.05 inches thick are cut to approximately 4 inches by 9 inches. These plates have holes drilled into them to properly attach to the tribometer table. For silicon dioxide wafer material, fused silicon dioxide plates that are 0.12 inches thick, 2.25 inches wide, and 6.50 inches long are utilized. The slurry tray seen in Figure 21 is machined to hold the silica plate firmly while also sealing the tray so slurry does not leak out of the contact.

Wafer materials are desired to have the surface roughness on the same order of magnitude as actual IC wafers. Similar surface roughness ensures that the contact behavior between the pad and wafer is comparable to CMP. Average roughness (R_a) and root mean squared roughness (R_q) of copper wafer surfaces are on the order of 1 to 10 nm (Lay and Duquette 2006, 1-9; Joo and Liang 2013, 979-987; Webb, Gack, and Reid 2004, 82-95). Average roughness and root mean squared roughness for silicon dioxide wafer surfaces are on the order of 0.1 nm to 1 nm (Nasrullah, Tyler, and Nishi 2005, 303-311; Lee, Kim, and Lee 1996, 1443-1451; Hiller et al. 2010, 064314; 064314). The R_a and R_q values for the wafer materials are measured with a Mahr Federal profilometer (Mahr GmbH, Göttingen, Germany). The profilometer is discussed in more detail later in Section 3.3.2. The average R_a and R_q values for each copper plate surface

before polishing are less than 0.063 um and 0.088 um, respectively. Average R_a and R_q values for each silicon dioxide surface before polishing are less than 0.016 um and 0.019 um, respectively. The roughness values for silicon dioxide plates are an order of magnitude larger than that of a typical silicon dioxide wafer. Yet, the silicon dioxide surface roughness is on the same order of magnitude as copper wafers and will provide similar experimental comparisons between materials. The copper plates have noticeable defects on their surfaces from the material supplier. These defects include scratches and dimples that are at the largest 0.1 mm wide and 2 um deep, based on profilometer measurements. The majority of the copper surface does not contain these defects and is accurately represented by the surface roughness provided. It is determined that these copper surfaces are sufficient for experimentation with the relatively low size and number of defects. Effects that these defects may have on the results are monitored though examination of the copper surfaces during and after the tribometer experiments.

The basic procedure of these experiments begins with adhering a piece of IC1000 polishing pad to the pad fixture. A plate of wafer material is secured to the reciprocating table using the slurry tray. Using the pneumatic cylinder with pressurized air, a load is applied to the pad to achieve the desired pressure for the area of pad material being loaded. This load is verified with the force transducer output. The motor translates the material contact in cycles at the proper velocity. At specified intervals of distance traveled, samples of pad material are collected for further topographical and thermodynamic analysis.

3.3.1.1 Dimensional Analysis

Dimensional analysis reduces the number of parameters to be varied in an experiment by combining all important parameters into a few non-dimensional groups. The method, known as the Buckingham Pi Theorem, is applied here to guide the design of experimentation (Buckingham 1916, 263-296). All of the important parameters are listed with their respective units, as presented in Table 1. Each parameter is assigned a type, whether it is a fixed value, controlled variable, or a variable. A fixed value is a parameter that cannot be changed in the experiments due to constraints of the CMP process or equipment. A controlled variable is a parameter that can be set during CMP and varied depending on the specific application. A variable is a parameter which is a function of the fixed values and controlled variables. Variables are the parameters that are typically measured, or calculated from data obtained in experiments. In Table 1, values for the fixed parameters and values for the minimum and maximum controlled variables are listed.

Table 1: Chemical-Mechanical Planarization Experiment Parameters

Parameter		Units	Type	Fixed	Minimum	Maximum
Normal Pressure	p	M/LT^2	Controlled Variable	-	2 psi	5 psi
Velocity	V	L/T	Controlled Variable	-	7.87 in/s	23.62 in/s
Distance Traveled of Pad	D	L	Controlled Variable	-	3,517 ft	10,548 ft
Effective Modulus	E*	M/LT^2	Cu: Fixed	20,400 psi	-	-
			SiO_2: Fixed	20,300 psi	-	-
Kinematic Viscosity	ν_s	L^2/T	Fixed	9.73×10^{-6} ft^2/s	-	-
Wafer Density	ρ	M/L^3	Cu: Fixed	8.94 g/cm^3	-	-
			SiO_2: Fixed	2.20 g/cm^3	-	-
Wafer Surface Energy	γ	M/T^2	Cu: Fixed	1.360 J/m^2	-	-
			SiO2: Fixed	4.275 J/m^2	-	-
Coefficient of Friction	μ	-	Variable	-	-	-
Change in Wafer Mass	Δm	M	Variable	-	-	-
Change in Average Wafer Waviness	ΔW_a	L	Variable	-	-	-
Average Roughness of Pad	R_a	L	Variable	-	-	-
Specific Enthalpy of Reaction	h	L^2/T^2	Variable	-	-	-

The three controlled variables for these experiments are the normal pressure, velocity, and distance traveled for the pad and wafer contact. It is desired to run these experiments to envelope the entire range of parameter values to observe the outputs as a function of the controlled inputs. Chosen minimum and maximum values for these parameters are based on the range of values stated in the literature and limits of the tribometer setup. It is found in the literature that the range of pressures used in CMP experiments can span 1 psi to 7 psi (Chandrasekaran et al. 2004, G882-G889). The

sensitivity of the force transducer and the smallest area of pad material possible for the pad fixture limits the minimum pressure. Using 1 psi would have provided too low of a force to accurately measure using the tribometer load cell. It is for this reason that the low pressure is increased to 2 psi so that accurate force measurements are made. From preliminary experiments testing the tribometer at higher pressures with the pad translating on the wafer, the adhesive of the polishing pad cannot handle pressures above approximately 5 psi in the tribometer setup. The pad material adhesive released from the fixture due to the extra friction at normal pressures above 5 psi. Release of the adhesive occurred only after an inadequate number cycles required for these experiments. The highest pressure is thus set to 5 psi so that the pad material remains fixed for the entirety of an experiment.

The range of relative velocities which occur in CMP are found in the literature to be 0.2 m/s to 1.2 m/s (Thagella 2004, G205-G215). In English units, this velocity range is from 7.87 in/s to 47.24 in/s. Through preliminary testing, it is found that the design of the tribometer does not allow for velocities above approximately 0.6 m/s. If the tribometer is run at velocities above this amount, the layer of slurry is forced out of the slurry tray due to the rapid deceleration when changing direction. The slurry level is reduced to an insufficient level after only a few cycles above this velocity. To keep the rate of slurry removal to a maintainable level, the maximum velocity is chosen to be 0.6 m/s, or 23.62 in/s.

In the planarization experiments, it is important to determine the maximum travel distance of a pad through its lifetime. This distance is a function of the velocity, the typical polish time per wafer, maximum number of wafers polished per pad, and

CMP geometry. The computation of total distance is based on the maximum distance a point on the pad travels against a wafer in one rotation. The geometry of the pad and wafer contact is shown in Figure 23. The pad trajectory is the rotational path of a point on the pad at radius r_t. The wafer radius is r_w, the offset radius is r_o, the contact arc length is s, and α is the angle that corresponds to the contact arc length. As the pad moves through one rotation, the pad is in contact with the wafer for the contact arc length distance, s. To compute the maximum distance traveled in contact by a point on the pad, it is necessary to determine the value of the pad trajectory radius r_t that maximizes the contact arc length.

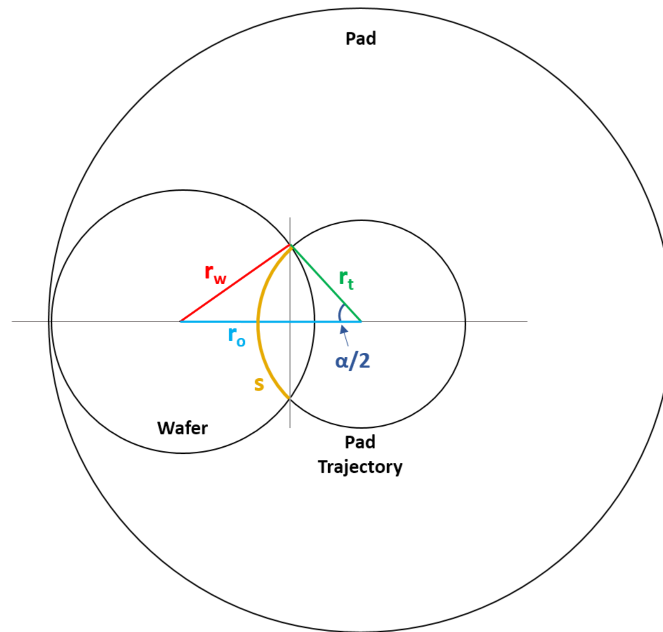

Figure 23: Arc Length of Pad and Wafer Contact through a Single Rotation

It is found through the literature that a common wafer diameter is 200 mm, and a common polishing pad diameter is 500 mm (Chandra et al. 2008, 559-562; Balakumar

et al. 2005, G867-G874). This results in r_w equal to 100 mm. Also, r_t can range from 0 mm to 250 mm, while r_o can range from 100 mm to 150 mm. The value of s is calculated based on the angle α and the law of cosines for the triangle outlined by r_w, r_t, and r_o. This relation using the law of cosines is given in Equation 17 (Leonard et al. 2014, 152),

$$r_w{}^2 = r_t{}^2 + r_o{}^2 - 2r_t r_o \cos {}^{\alpha}/_{2} \qquad \text{Equation 17}$$

The equation is rearranged to solve for α. Equation 17 is then used to compute the contact arc length of the circular pad trajectory as the angle α multiplied by the radius of the arc length r_t,

$$s = \alpha r_t = 2r_t \cos^{-1} \frac{r_t^2 + r_o^2 - r_w^2}{2r_t r_o} \qquad \text{Equation 18}$$

Maximum contact arc length occurs at some value of r_t. To find this value, the derivative of Equation 18 is taken with respect to r_t and set equal to zero, shown in Equation 19,

$$\frac{ds}{dr_t} = 2\cos^{-1}\left(\frac{r_t^2 + r_o^2 - r_w^2}{2r_t r_o}\right) + \frac{2(r_o^2 - r_t^2 - r_w^2)}{r_t r_o \sqrt{B}} = 0 \qquad \text{Equation 19}$$

Setting the derivative equal to zero solves the maximum arc length with respect to the trajectory radius. B is given in Equation 20,

$$B = -\frac{r_o^4 - 2r_o^2(r_w^2 + r_t^2) + (r_w^2 - r_t^2)^2}{r_o^2 r_t^2} \qquad \text{Equation 20}$$

Using MATLAB, r_t in Equation 19 is numerically solved and obtained using r_w equal to 100 mm, and r_o equal to 100 mm or 150 mm. The results provide a maximum contact arc length of 224.44 mm when r_o is 100 mm at a trajectory radius of 130.44 mm.

With the maximum contact distance traveled by the pad in one rotation, the total maximum travel distance through the service life of a pad can be computed. To compute this distance, the number of rotations which a pad completes during its duty cycle is needed. The angular velocity of a polishing pad is computed as a function of r_o and the relative velocity of the pad and wafer, given in Equation 21 (Saka 2001, 233-238),

$$\omega = \frac{V}{r_o} \qquad \text{Equation 21}$$

ω is the pad angular velocity, V is the relative velocity, and r_o is the offset radius. This equation is for the pad and wafer rotating at the same angular velocity with their centers offset by r_o. These conditions are typical of CMP processes. The angular velocities for the minimum and maximum velocities of 7.87 in/s and 23.62 in/s at r_o of 100 mm are calculated using Equation 21. The minimum and maximum angular velocities are 19.1 rpm and 57.3 rpm, respectively.

The measurement used in CMP to determine the amount that a wafer should be polished is by polishing time. The standard time that a single wafer is polished is reported to be 60 seconds, from multiple sources (Eusner et al. 2009, H528-H534; Chandra et al. 2008, 559-562; Armini et al. 2007, H667-H671). The standard service life of a single IC1000 polishing pad is approximately 250 wafers/pad (Huey et al. 1999, 54 - 58). The maximum distance traveled is computed based on the equivalent minimum and maximum angular velocities, the distance traveled per revolution of 224.44 mm,

polishing time of 60 seconds, and a total of 250 wafers. The maximum distances traveled for the minimum and maximum velocities are computed to be 3,517 feet and 10,548 feet, respectively. Depending on the maximum or minimum velocity, the tribometer experiments are conducted until the pad material has traveled the corresponding distance in contact.

With the range of controlled variables decided, the values for fixed parameters are determined. The effective modulus of the contact is a relation which combines the elastic properties of the wafer and pad materials, given in Equation 22 (Bhushan 2002),

$$\frac{1}{E^*} = \frac{1-\nu_1^2}{E_1} + \frac{1-\nu_2^2}{E_2} \qquad \text{Equation 22}$$

This modulus accounts for the elastic properties of both materials of the contact as subscript 1 and 2. The elastic modulus of the high purity copper plates is from that of 99.99% bulk copper, which is 117 GPa or 17.0 x 10^6 psi (Brandes and Brook 1992, 14-6). Poisson's ratio of bulk copper is about 0.34 (Sadd 2009; Brandes and Brook 1992, 14-6; Lee et al. 2009, 51-54). The silicon dioxide properties are referenced from material supplier information which was provided with the silica plates (Shin-Etzu, Tokyo, Japan). The elastic modulus of the silica plates is 73 GPa or 10.6 x 10^6 psi, and the Poisson's ratio is 0.17. The elastic modulus of the pad material is taken from a quasi-static tensile test conducted on a pad sample using a universal testing machine, as discussed in Section 3.2.2.2. Since the stress acting on the pad sample is non-uniform due to the grooves, the modulus is taken using an average of the thickest and thinnest parts of the pad for an approximation. This value of the IC1000 pad quasi-static bulk elastic modulus is 132 MPa or 19.1 x 10^3 psi. Although this is not the elastic modulus

of the pad material in compression as the material is used, this value provides a representative value of the pad modulus to compare to the wafer materials. The Poisson's ratio of the IC1000 pad is taken as 0.25 as determined from the pad compression tests in the current work, as discussed in Section 3.2.2.1. Discussion of the results of this value is presented in the Section 4.1.2. With these elastic moduli and Poisson's ratios, the effective modulus is computed separately for copper and silicon dioxide against the IC1000 pad using Equation 22. The effective modulus for copper and IC1000 pad is 20,400 psi. For silicon dioxide and IC1000 pad, the value of effective modulus is 20,300 psi.

Elastic modulus of the IC1000 pad material is taken as a constant for this dimensional analysis as a representative value. The modulus can change as a function of several parameters that include frequency of loading, temperature, and soak time. Results of dynamic mechanical analysis (DMA) of IC1000 pad material is presented in the literature. DMA provides the storage and loss modulus of the pad sample as it is exposed to an oscillating load and various temperature ranges. For the planarization experiments performed with the tribometer, velocities are taken to be 7.87 in/s or 23.62 in/s. The tribometer table moves 4 inches in each direction, or 8 inches for one complete cycle of table reciprocation. With these values, the frequency in which the load applied changes direction is from 0.98 Hz to 2.95 Hz. From the results of DMA, it is shown that the storage modulus of the IC1000 pad in shear increases slightly with increasing frequency. Specifically from 120 MPa at 0.1 Hz to 135 MPa at 1 Hz, holding all other parameters constant (Li et al. 1995, 601-606). With such a small change in material stiffness through frequencies on the order of 0.1 Hz and 1 Hz, it is assumed that the

elastic modulus of the pad material as a function of the velocity is constant. From the same DMA experiments, change in material stiffness as a function of temperature is measured. The literature states that the temperature of typical CMP contact can range between 20°C and 40°C (Charns 2005, 188-193; Kakireddy 2008, 141-150; Jiao et al. 2011). DMA results show that stiffness of the pad decreases with temperature. From 20°C and 40°C, the storage modulus of the IC1000 pad in tension decreases from approximately 750 MPa to 500 MPa, with all other parameters constant (Lu, Obeng, and Richardson 2002, 177-186; Charns 2005, 188-193; Kakireddy 2008, 141-150). With a change in storage modulus being less than an order of magnitude, it is assumed the pad modulus is constant through the potential temperature range that occurs in the CMP processes.

The amount of time which the polishing pad soaks in aqueous slurries has the effect of decreasing the modulus of the pad material. DMA experiments in the literature show that the shear storage modulus of the IC1000 pad decreases from approximately 135 MPa to 105 MPa after soaking for 800 minutes (Li et al. 1995, 601-606). It is at 800 minutes of soaking time the storage modulus approaches a constant value with respect to soak time. To eliminate the variation of pad modulus through the tribometer experiments as the pad material soaks in slurry, each pad sample is soaked for at least 14 hours, or 840 minutes, before use. When the pad sample is removed from the slurry to be secured to the tribometer, it is not allowed to dry for more than 20 minutes. The pad elastic modulus is thus treated as a constant value in the tribometer experiment dimensional analysis.

Important properties of the ACuPLANE slurry include the fluid's mechanical behavior, represented with kinematic viscosity. CMP slurries are mainly comprised of water, with approximately 80% water, 15% abrasives, and the remainder being various chemicals (Cabot Microelectronics, Aurora, IL). It is assumed that the slurry behaves as a Newtonian fluid with its high water content. The kinematic viscosity of the slurry is taken as that of water at room temperature of 25°C, which is equal to 0.973 x 10^{-5} ft/s^2 (White 2011, 826).

Density and surface energies of the wafer materials are important in computation of energy that is dissipated in wearing the material away. The density of copper is 8.94 g/cm^3 at room temperature (Brandes and Brook 1992, 14-6). Silicon dioxide plates have a density of 2.20 g/cm^3 from the manufacturer information (Shin-Etsu Chemical Co., Tokyo, Japan). Surface energies of material can be computed from fracture toughness values and related to the critical energy release rate. Mode-I fracture toughness of pure copper at room temperature is reported to be 110 $MPa \cdot m^{1/2}$ (Atkins and Mai 1985, 798; Ghosh and Prakash 2013, 224-34). For assumed plane stress experimental conditions, the fracture toughness of a material under a single mode of fracture is related to the energy release rate with Equation 23,

$$2\gamma = G_c = \frac{K_c^2}{E} \qquad \text{Equation 23}$$

K_c is the critical stress intensity factor, or fracture toughness, E is the elastic modulus of the material, and γ is the surface energy of the material. From Equation 23 and the elastic modulus of copper equal to 117 GPa, the critical energy release rate of copper is 103 kJ/m^2, giving a surface energy value of 51.5 kJ/m^2. This value is much larger than

that reported of the copper surface energy found using liquid contact angles, which is 1.360 J/m^2 (Kinloch 1987, 18). It is believed that the fracture toughness values reported for copper includes energy of plastic deformation, since copper is not a brittle material. It is desired to use the surface energy alone to determine the energy of mass loss only, not including plastic deformation. Thus, the value of 1.360 J/m^2 is taken as the copper surface energy. For fused silicon dioxide, the surface energy is reported to be 4.275 J/m^2 at room temperature (Lucas 1995, 743-8).

The remaining parameters are variables that include coefficient of friction, which is calculated from measurements from the tribometer load cell readings as the ratio of friction force to normal force. Change in mass of the wafer material is measured using a Mettler Toledo XS304S scale (Mettler-Toledo, Columbus, OH). Change in waviness of the wafer material is a parameter used to estimate the energy dissipated from wearing the wafer material. The average roughness of the pad material characterizes the surface evolution of the pad. This change in wafer waviness and pad roughness is measured using a profilometer, discussed in detail in Section 3.3.2. Enthalpy of reaction is a measure of the internal energy of the pad material, which is obtained using differential scanning calorimetry (DSC). The DSC experiments are discussed in more detail in Section 3.3.3.

All of the important parameters for the experiment are determined and characterized. This information allows for the construction of non-dimensional pi groups to reduce the number of parameters to vary in the experiments. The Buckingham Pi Theorem is used to arrange the dimensional parameters into pi groups. Since pi groups are dimensionless and all parameters describe the behavior of the experiments,

each pi group is a function of one another. It is desired to create a functional relationship which states that the pi group which has the variables is a function of the pi groups with controlled variables. The constructed pi groups in the functional relationship is presented in Equation 24,

$$\frac{\Delta m\mu\gamma}{h\rho^2 \Delta {W_a}^2 {R_a}^2} = f\left[\frac{pUD}{\nu_s E^*}\right] \qquad \text{Equation 24}$$

The first pi group on the left includes all the variables to be measured in the experiments. The remaining pi group contains all the variables which are controlled in the experiments. To envelope the entire range of controlled variables, minimum and maximum values are run in each experiment. By using the minimum and maximum parameter values in the pi groups, the non-dimensional parameter has a minimum and maximum value as well. Running the experiments for each trial to have a different combination of extreme values completely covers the entire spectrum of this functional relationship. This method results in a test matrix that organizes all of the trials needed to be performed for each wafer material, presented in Table 2, without double counting of any parameters.

Table 2: Planarization Test Matrix

Wafer Material	***V***	***p***	**Distance Traveled (D)**	**Pi Group**
Copper	Minimum	Minimum	Take measurements at intervals of distance traveled.	$0 \leq \frac{pVD}{\nu_s E^*} \leq 526{,}000$
		Maximum		
	Maximum	Minimum		
		Maximum		
Silicon Dioxide	Minimum	Minimum		
		Maximum		
	Maximum	Minimum		
		Maximum		

The test matrix provides that eight experiments are required to be performed. In these experiments, each wafer material requires all four combinations of low and high velocity and pressure parameters. Variables are continuously measured through the distance traveled in an experiment, while pad material is collected at various intervals of distance traveled. With the maximum distance traveled set for an equivalent of 250 wafers. The iterations of distance chosen to collect pad samples are for the equivalent distances of polishing 10, 50, 100, and 250 wafers. This provides a collection of pad samples from each experiment which contain information about how the pad material evolves through CMP.

3.3.1.2 Experimental Procedure

With the experimental design completed, a summary of the tribometer planarization experiments is provided. A sample of pad material is cut from an IC1000 pad to be 6 squares by 8 squares in size, with nominal dimensions of 1.5 inches by 2 inches. To ensure that the pad material maintains a relatively constant elastic modulus through the entire experiment, the pad sample is soaked for at least 14 hours before the experiment is begun, as discussed previously. The motor control and table are set up so that the table travels a total of 8 inches for each cycle. LabView is set to record force values at a frequency high enough to result in at least 10 samples per cycle. This number of data points allows for a better observation of mechanical variations through a single cycle.

The wafer material plate is weighed and then secured to the tribometer table with the slurry tray and tightened screws. The pad sample is adhered and properly centered

to the pad load cell fixture. Approximately 20 ml of slurry is then applied onto the wafer material in the slurry tray. While the pad material is still not in contact with the wafer plate, the force transducer is zeroed. While measuring the load, air pressure on the pneumatic cylinder is applied to force the pad material onto the wafer plate. Pressure is applied until the desired load is reached for the trial being performed and for the current nominal pad area. The number of cycles is set so that the end distance traveled coincides with the next interval of pad sample collection; either for polishing 10, 50, 100, or 250 wafers.

Throughout the course of the experiments, the set normal pressure needs to be monitored and adjusted periodically. The loads applied are relatively small compared to typical loads that this tribometer applies. With this, the normal force can drift through the course of the experiment. Slurry has to be periodically added to the slurry tray due to evaporation and potential splashing during trials of higher velocity.

After the interval number of cycles has been reached and the motor stops reciprocating, data collection is then halted. The pad material is unloaded from the wafer. A 2 square by 6 square sample of pad material is obtained from the whole sample using a razor. It is then rinsed in distilled water to remove the majority of slurry and wear particles. The remaining pad material is placed back into the fixture and properly centered. Proper normal force is applied for the new pad sample area onto the wafer plate. The removal of pad sample is done for intervals of distance equivalent to polishing 10, 50, 100, and 250 wafers. This distance depends on the velocity of the trial. After the total distance for polishing 250 wafers has been achieved on the remaining pad material,

the experiment is complete. The wafer plate is cleaned with water to remove any slurry or wear residue. The wafer plate is weighed after the water has dried.

These experiments are performed for both copper and silicon dioxide wafer materials. For each material, the experiments are run up to the maximum travel distance for all four combinations of pressure and velocity. Wafer plates and polishing pad samples that result from these experiments are applied to the next set of experiments for further analysis.

3.3.2 CMP Material Topographical Evolution

The topography of contacting surfaces is important for understanding and modeling contact mechanics behavior. Measurement of pad and wafer topography provides the geometry of pad and wafer surface asperities. The geometry supplies information to calculate stress fields and understand frictional behavior for the pad and wafer contact. Measuring surface roughness before and after polishing also unveils information about how the CMP materials wear and plastically deform. Surface roughness ultimately provides a geometric understanding of the pad and wafer contact, describing their surface evolution through applied stress fields during CMP.

Profilometry also provides information about larger scale surface features than those typically quantified as roughness. In general, a surface has a wide range of roughness length scales superimposed onto each other (Bhushan 2002). Depending on the surface being measured, roughness is typically considered to be on the nanometer to millimeter scales of wavelength along the surface. Topographical variations on larger

scales are represented as surface waviness. In this work, both roughness and waviness are important for different aspects of the surface analysis.

For the planarization experiments, roughness and waviness of the pad and wafer materials are measured before and after use. Topography is measured using a Mahr Federal Perthometer with a MFW 250 tracing arm, shown in Figure 24. This device is controlled using MarSurf XR 20 software (Mahr GmbH, Göttingen, Germany), which records the surface profile heights and computes roughness and waviness values. The device is calibrated using a certified roughness standard from Mahr Federal.

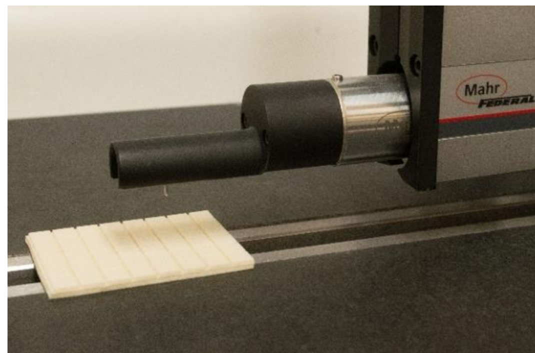

Figure 24: Mahr Federal Perthometer

The travel length used for most measurements is set to 5.6 mm, the longest length available. This length provides better representative roughness values of a surface over a longer sample length. A travel length of 1.75 mm is chosen for roughness measurements of features smaller than 5.6 mm in length. Travel velocity for the travel length of 5.6 mm and 1.75 mm is 0.50 mm/s and 0.10 mm/s, respectively. For all trials, data is collected every 0.5 um along the length of travel. Roughness values are determined by MaxSurf XR 20 using a Gaussian low-pass filter with a short bandwidth

filter of 2.5 um to filter digital noise within the device. The cut off wavelength used to separate roughness and waviness measurements is 0.8 mm. In each experiment, the gathered roughness values are average roughness (R_a) and root mean squared roughness (R_q). Waviness measurements (W_a and W_q) of the same type are computed as well.

It is desired to track the evolution of pad and wafer material topography through the CMP process. The roughness of the wafer plates is taken before tribometer experiments, as well as after they are polished through 250 wafers. Topography is measured along the length of the plates as well as across the width for each plate, before and after polishing. New IC1000 pad material surfaces are measured with the profilometer to characterize pad topography before planarization experiments. The groove patterns on the IC1000 pad surface, as seen in Figure 11, make it necessary to measure roughness along certain directions. Roughness is measured along the length of the small grooves within a square. The topography of all of the pad samples that are collected from the planarization experiments are measured to view potential changes in roughness from the planarization process.

3.3.3 Polishing Pad Differential Scanning Calorimetry

Energy dissipation in chemical-mechanical planarization can potentially dissipate into the polyurethane pad material as internal energy. This internal energy dissipation is mathematically represented by $\rho\dot{u}$ in Equation 5. The polyurethane foam of the polishing pad experiences the strain energy or sensible heat due to applied tractions. Some of this energy may be dissipated within the polymer structure of the

IC1000 pad, which can result in the alteration of the chemical makeup of the material. To track changes of internal energy, differential scanning calorimetry (DSC) of the collected pad material samples is conducted. In DSC, two aluminum pans (TA Instruments, New Castle, DE) are placed onto their own respective heaters in a calorimeter's heating cell. A diagram of a generalized DSC heating cell is shown in Figure 25. One pan contains the sample material being tested while the second one is an empty reference pan. The DSC maintains both sample and reference pans at the same temperature as they are exposed to a user set temperature program. The difference in heat flow, or power, applied to the sample and reference heaters is recorded with the temperature of the heaters. As the pans are heated, the DSC measures endothermic or exothermic thermal events that occur through the temperature change of material in the sample pan. For polymers, these events typically include phase changes, glass transition, and oxidation, among others. The resulting data describes aspects about the internal structure of the polymer and its thermal history through the observed thermal events. Changes to the internal material structure as a result of energy input to the sample can thus be tracked quantitatively.

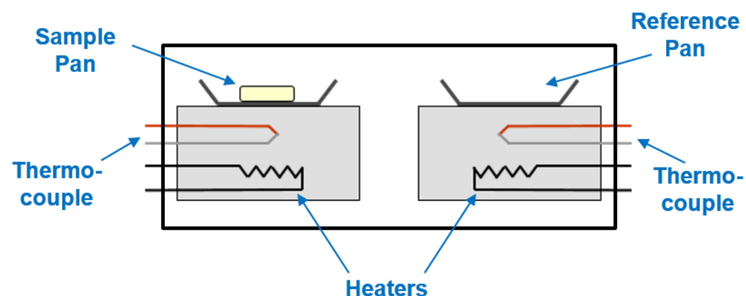

Figure 25: Differential Scanning Calorimetry Heating Cell

Pad samples tested in the calorimeter are in an atmosphere of constant pressure. Thus, the change in heat flow measured provides a means to compute the enthalpy of reaction for the thermal events that occur. The First Law of thermodynamics is the balance of energy, which states that the change in internal energy of the system is equal to the heat added to the system plus the work done on the system, given in Equation 25 (Dill and Bromberg 2003, 105-152),

$$dU = \delta q + \delta w \quad \text{Equation 25}$$

dU is the change in energy of the system, δq is heat flowing into the system, and δw is work done on the system. For DSC, the system is the sample pan, sample itself in the pan, and the reference pan. The definition of change in enthalpy of the system, represented by dH, is the internal energy plus the product of pressure and volume. Differentiating enthalpy and substituting results in Equation 25 for dU gives a relation for dH as Equation 26,

$$dH = \delta q + \delta w + pd\text{V̵} + \text{V̵}dp \quad \text{Equation 26}$$

p represents pressure and V̵ represents volume. For DSC, rate of temperature increase is conducted slowly to approximate quasi-static processes for more simple analysis. For a quasi-static process, $\delta w = -pd\text{V̵}$. The DSC is also run in a constant pressure atmosphere, so that $dp = 0$. With these simplifications, the change in enthalpy for DSC is the change in heat supplied to the system, as in Equation 27,

$$dH = \delta q \qquad \text{Equation 27}$$

This description of enthalpy assumes that no mass of the pad samples is added or lost during experimentation. The assumption of no mass loss is acceptable for trials that are conducted below the decomposition temperature of IC1000 polyurethane, which is 250°C (Yang et al. 2010, 338-346). It is found from performed DSC trials that the mass loss of a pad sample is never more than 5% of the original sample mass, if the sample stays below this decomposition temperature.

Computation of the total enthalpy of a thermal event is possible from the heat flow measurements at a constant rate of temperature change. The heat flow being measured at constant pressure is represented by $\dot{q}$, which is the time rate of change of the heat q, given in Equation 28,

$$\dot{q} = \left(\frac{\delta q}{dt}\right)_p = \frac{dH}{dt} \qquad \text{Equation 28}$$

With a constant rate of temperature, the heat flow can be divided by the rate of temperature change to acquire the heat capacity at constant pressure, mathematically described in Equation 29.

$$C_p = \left(\frac{\delta q}{dt}\right)_p \frac{dt}{d\theta} = \frac{dH}{dt}\frac{dt}{d\theta} \qquad \text{Equation 29}$$

Thus, the heat capacity difference between the sample and the reference pan at a temperature is the heat flow divided by the rate change of temperature. With the heat capacity, total change in enthalpy of the system between two temperatures can be computed with Equation 30,

$$\Delta H = \int_{T_A}^{T_B} C_p d\theta \qquad \text{Equation 30}$$

T_A and T_B are the temperatures at the beginning and end of the thermal event of interest, respectively. Enthalpy of a thermal event is the area under the heat flow versus temperature curve, above or below the baseline heat flow, divided by the constant rate of temperature change.

A DSC is used to measure heat flow between an empty aluminum reference pan and an aluminum pan of the IC1000 polishing pad material. These experiments provide information on how the internal structure of the IC1000 pad changes through CMP as a function of the controlled variables. The specific DSC used for these heat flow measurements is a TA Instruments Q10 DSC (TA Instruments, New Castle, DE). The instrument is cleaned and calibrated to provide accurate results. The DSC's baseline slope and offset are calibrated by running an empty cell through the temperature range used in experimentation. A single point temperature calibration and cell constant calibration is conducted with a 10.86 mg sample of 99.99% indium powder.

IC1000 pad samples are prepared for the DSC by using a razor to shave off the top layer of pad material. The pad's top surface layer provides the best representation of the material that is altered by planarization. If the bulk pad material is mixed in, the results are more likely to represent new pad material. The thickness of the shaved specimens of pad material range from approximately 0.005 inches to 0.015 inches. Width of the specimens are kept no larger than 0.100 inches. It is desired to keep the IC1000 pad pieces to be small and thin so that there is a small temperature gradient through the sample (Brown 1998, 691). Thinner samples provide heat flow data of a

thermal event with less temperature spread. The mass for a total sample of the IC1000 pad in a pan is kept between 2 mg and 5 mg so that the majority of the pad pieces are touching the base of the pan that is in contact with the heater. These relatively small masses provide the same benefit as thin specimens, yet still provide a significant heat flow reading.

The DSC cell is purged with 50.00 ml/min of nitrogen gas at atmospheric pressure during all experiments. Aluminum pans are sealed with aluminum hermetic lids using an encapsulating press. To maintain the constant pressure atmosphere inside of the pans, a hole is punctured through the top of the lid of each pan tested. The aluminum pan for each sample is weighed before and after pad material is placed into it. The lid is then placed on top of the pan containing the sample, pressed, and the hole is punctured. The completed sample pan is weighed. These weight measurements allow for proper calculation and separation of the pan, lid, and pad sample mass.

The temperature program used to test each IC1000 pad sample begins with an initial temperature of 30°C. The pans are first heated to 225°C and then cooled down to -75°C. Finally, the pans are heated back up to 225°C. A minimum of -75°C is used to acquire the most information possible from the experiments as this is the lowest temperature that the DSC can achieve. A maximum of 225°C is used as the maximum temperature to maintain a constant sample mass through heating. Previous work has conducted thermogravimetric analysis (TGA) on IC1010 pad material (Yang et al. 2010, 338-346), which is made of the same polyurethane foam as IC1000 pads (Dow Chemical Co., Midland, MI). TGA measures the mass of a material sample as it is heated through a range of temperatures. It is found that the pad material begins to decompose and lose

mass at 250°C. To be able to properly compare irreversible thermal events properly, the mass should be the same between the first and second heating cycles. The maximum temperature is kept to 225°C for constant mass. Several DSC experiments are run using the same method, but with 400°C as the maximum temperature to observe additional thermal events as the polishing pad samples decompose.

After each temperature endpoint is achieved, the samples are held isothermally for 1 minute. Holding the temperature at the endpoints before changing temperature rate direction ensures the entire mass of the samples have reached the end temperatures. The rate of temperature change for heating and cooling is kept constant at 10°C/minute. Past work in the literature, in which differential thermal analysis (DTA) was conducted on IC1010 polishing pad material, used the same heating rate (Yang et al. 2010, 338-346). This heating rate has been shown to be large enough that thermal events are easily identified.

CHAPTER 4

FINDINGS

4.1 Results of Polishing Pad Constitutive Modeling

Proper constitutive modeling of the chemical-mechanical planarization (CMP) polishing pad is required for proper stress analysis of the material. Results of the compression relaxation and tensile relaxation experiments on the pad material are discussed here. In addition, the compressibility experimental results are presented.

4.1.1 Compressive Stress Relaxation Experiments

IC1000 pad material is mechanically characterized in compression using the fabricated compression test setup discussed in Section 3.2.2.1. Stress relaxation experiments are performed on IC1000 pad material where a strain is applied and held constant over time. The voltage output of the load cell is measured with time for approximately 70 minutes while the pad material relaxes. This voltage data is then converted into stress values based on the load cell calibration and the nominal area of the pad sample. Strain of the pad sample is monitored using video captured through a microscope and CCD camera. The video is processed with MATLAB to compute strain based on the images captured. Strain is applied at a rate so that the held strain is reached in approximately 5 seconds. The peak load and stress of each trial is measured and compared to the strain that is held.

Compression relaxation experiments on pad samples of varying areas and initial loads were carried out initially. From initial characterization of the compression test, it was found that strain measurements from different trials were inconsistent with applied stress. To acquire a better understanding of the compression setup behavior, compression experiments were conducted on a material much stiffer than the pad samples. This material is a printed circuit board material called FR-4 that is approximately 0.036 inches thick and has an elastic modulus of 2.4×10^6 psi. This material has an elastic modulus two orders of magnitude larger than the IC1000 pad, so it is expected to strain much less under similar stresses. The results of the stress and strain values for these trials are tabulated in Table 3. The data from these experiments show that regardless of the level of stress applied or the modulus of the material, the constant strain measured is between 1.0% and 2.9% strain. There is no particular trend in strain with stress or applied load. It is speculated that the load cell of the compression setup, shown in Figure 12, is bending while load is applied. This bending would cause the compression block to rotate, giving the illusion on the captured images that the material is straining more than it is. Strain measurements from the current setup thus cannot be trusted. A button type compressive load cell would be more suited for this compression setup, which is to be implemented in future work.

Table 3: Compressive Strain of IC1000 and FR-4

Trial	Material	Area (in^2)	F_o (lb_f)	σ_o (psi)	ε (%)
1	IC1000	0.063	5.41	86.49	1.2
2	IC1000	0.188	5.81	30.99	1.4
3	IC1000	0.375	1.77	4.70	1.4
4	IC1000	0.375	2.11	5.64	1.5
5	IC1000	0.375	3.14	8.38	2.0
6	IC1000	0.375	4.33	11.53	2.5
7	FR-4	0.418	5.42	12.96	2.9
8	FR-4	0.418	5.40	12.91	1.0
9	FR-4	0.418	5.91	14.14	1.5

While the strain measurements are not usable with the available equipment, it is argued that measurements of average stress are still useful for characterizing the material behavior. Bending of the load cell, and thus rotation of the compression block does implement an uneven stress distribution across the length of the pad sample. If the same length of pad sample is used, the compressive stress distribution is constant with each trial. The change in relaxation behavior between pad samples tested with this setup can be compared with confidence.

An ASTM standard on creep testing of plastics states that the load applied and displacement measured cannot have more than ± 1% error from their desired quantities (ASTM 2001). Since relaxation experiments measure load and apply displacement, these acceptable margins of error can be applied for stress relaxation as ± 1% error as well. The largest error for load measurements is with the load cell's mechanical creep at 0.01 lb_f per hour. Each experiment performed is approximately 70 minutes long. Thus, a maximum error of approximately 0.012 lb_f due to the load cell creep occurs

through the experiment. With loads no less than 1.5 lb_f applied during these experiments, this error of load is within the acceptable margin.

To determine the validity of the assumption that strain is held constant, measurements of the change in distance between the block edges are measured from videos taken every 10 minutes through the 70 minutes of total time. These measurements are conducted for eight different experiments. Though the strain measurements cannot be relied upon, distance measurements can be used to evaluate error in the held displacement from the initial displacement. Results of error in held compressive displacement with time is presented in Figure 26. This figure shows some amount of creep in the thickness of the pad sample, with a relatively large initial jump in strain for the first 10 minutes. This creep occurs because the compression block is not held fixed relative to the compression test fixture. Thus as the pad sample relaxes, it can also creep slightly. The change in distance between the compression blocks is at a maximum of 0.4%. This percent change corresponds to a displacement of 0.017 mm, which can compared to the thickness of the pad sample of 1.27 mm. It is kept in mind that using this displacement measurement for the pad displacement is not accurate, as determined from the stress and strain behavior just discussed. But, this is the change in displacement of the total system between the two block edges. From the information gathered it is impossible to tell what the displacement magnitude of the pad sample is. Thus, it is unknown whether the displacement errors are appropriate for a relaxation experiment. But, from the data presented in Figure 26, the creep of the system appears to be consistent with each trial. From this, it is assumed that the displacement error of

all trials are similar so that the data gathered from the compression relaxation experiments can be compared with each other for information desired.

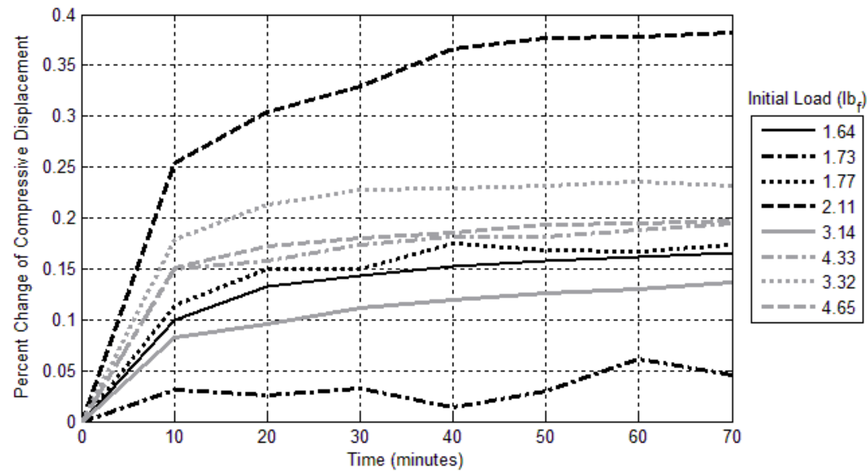

Figure 26: Percent Change in Block Edge Displacement with Time

4.1.1.1 Polishing Pad Compressive Relaxation with Soaking

Stress relaxation experiments of pad material that have undergone conditioning through soaking in slurry, and distilled water are tested. Also experimented on are pad samples taken from planarization experiments. All of these trials are set to be performed at a pressure of 4 psi. This stress level is common for CMP processes and is an appropriate level for stress relaxation characterization of the pad material (Chandra et al. 2008, 559-562; Armini et al. 2007, H667-H671). The time between initial measured load and peak load was attempted to be held constant for all trials at 5 seconds. The average time loaded was 5.20 seconds with a standard deviation of 0.40 seconds. All

pad material samples tested have an area that consists of six full squares on the pad surface, which is equal to a nominal area of 0.375 in^2.

Pad material in various conditions are tested to observe the effects that CMP has on the viscoelastic behavior of the polishing pad. Compression test trials are carried out with pad material that is new, new and soaked in slurry, new and soaked in distilled water, and from the planarization experiments that have polished the equivalent of 50, 100 and 250 wafers. The effects of slurry chemicals and water are observed through these various trials. These new and soaked pad samples are tested right after removal from the slurry or distilled water to observe mechanical behaviors when they are still wet. Also, new and soaked pad samples are tested after being dried. The slurry used in soaking is the same ACuPLANE slurry used in the planarization experiments. The new pad material is soaked in slurry and distilled water for between 14 and 18 hours. This soak time is chosen since the literature has reported that the storage modulus of IC1000 reaches a near constant value after 800 minutes (Li et al. 1995, 601-606). The samples are determined to be dry when the sample weight has stopped decreasing over time from water evaporation. For IC1000 pad material, this is approximately 72 hours for slurry and distilled water. The mechanical effects from using the pad material are also observed through the pad material collected from the planarization experiments.

Three pad samples are used from planarization experiments that were polished against the copper wafer, at low pressure, and at high velocity. These samples have in-contact travel times equal to 50, 100 and 250 wafers. Used pad samples are chosen as an attempt to compare the mechanically tested results to the results in literature that show pad scratching is reduced as a pad is used in CMP (Eusner, Saka, and Chun 2011,

H379-H389). From the literature, a pad is considered "broken-in" after it has been used in CMP enough that scratching is reduced. The samples are taken from the low pressure, high velocity copper planarization experiments because this experiment has the closest boundary conditions to that reported in the literature.

Trials are performed with the compression setup in which there is no pad sample and the two compression blocks are touching. It is found that the compression test setup relaxes in itself with a constant held strain. This system relaxation can be properly accounted for and separated from the results to acquire only the pad relaxation. In these experiments, strain is held constant while the initial stress is the controlled variable. The pad and test setup are always under the same load during the experiments since the pad completely separates the two compression blocks. Regardless of whether a pad is being tested or not, the compression setup relaxes the same way under the same initial load applied. The system relaxes the same way because the displacement of the system is always constant at the same initial load, assuming that no plastic deformations of the system occur. The measurement of stress relaxation of the pad and the system is a linear combination of both relaxations. Separation of the two relaxations is possible by characterizing the relaxation of the system alone. Then, this relaxation can be removed from the results to provide the pad relaxation itself. Since the system is a linear combination of stress relaxation in series, the system relaxation can be subtracted from the pad relaxation to isolate the pad behavior.

Multiple trials of the various conditions of pad material samples are run to acquire more confidence in the results. Five trials of the compression setup itself at an initial stress of 4 psi are conducted to provide an accurate characterization of the

system's relaxation. Six trials of the new pad material are performed to provide a sufficient baseline comparison for IC1000 pad material. From the distilled water soaked new pad samples, two relaxation trials are performed dried, and three are performed wet. Two samples are tested for the new pad with slurry soaked and dried, and new pad with slurry still wet. The remaining samples of new pad in slurry soaked and dried, along with the three samples from the planarization experiments only have one trial each. The reason for only one trial of these pad samples is due to the limited amount of available pad material in this condition.

The initial stress value is based on the maximum force measured, which occurs when strain input is halted. This value is shifted to be at the time of zero, as this is when relaxation begins. Stresses are normalized with the initial stress to properly characterize the relaxation behavior and remove the fluctuations between initial stress values of each trial, near 4 psi. Initial stress values of these stress relaxation trials range from 3.85 psi to 4.71 psi. Each trial is run for at least 4000 seconds to view the majority of the stress relaxation, as stress approaches a constant value. Results of the stress relaxation experiments are presented in Figure 27 as normalized stress versus time. A second figure is provided in which the data from 'New Pad, Slurry Dried', 'Cu LP HV 50' and 'Cu LP HV 250' are removed so that the remaining data is easier to observe. The labels 'Cu LP HV 50' are the planarization experiment pad samples that were planarized against copper at low pressure, high velocity, and at a polished wafer count of 50, 100, and 250. The normalized stress values for all trials except for the new pad in slurry that was soaked and dried, and the planarization experiment samples, are from data of multiple

trials averaged together with time. The average standard deviation through time from the averaging of this data is presented in Table 4.

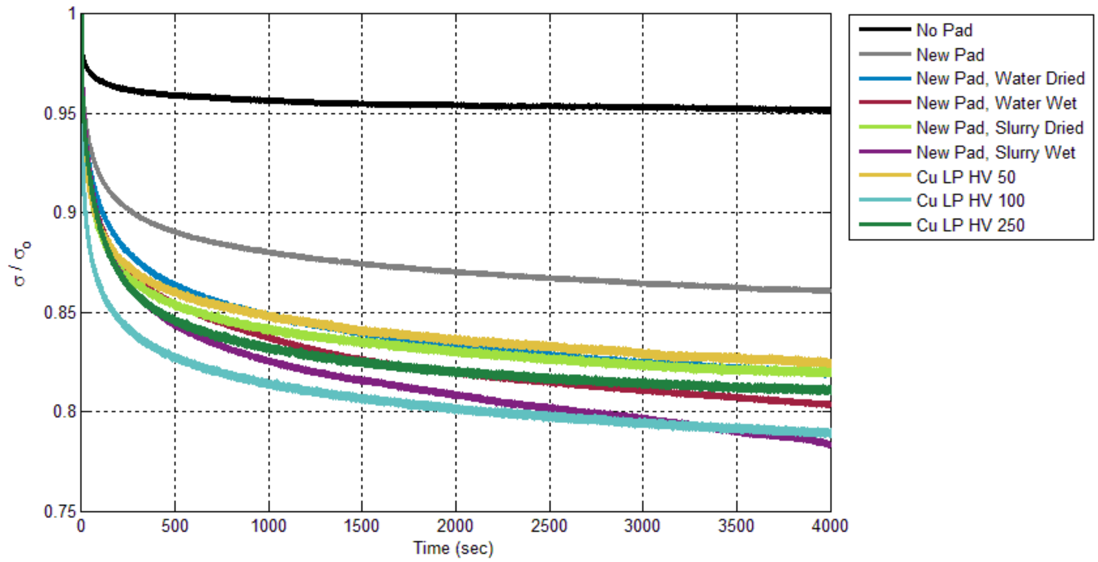

Figure 27: Normalized Stress Relaxation of Pad Material in Compression at 4 psi

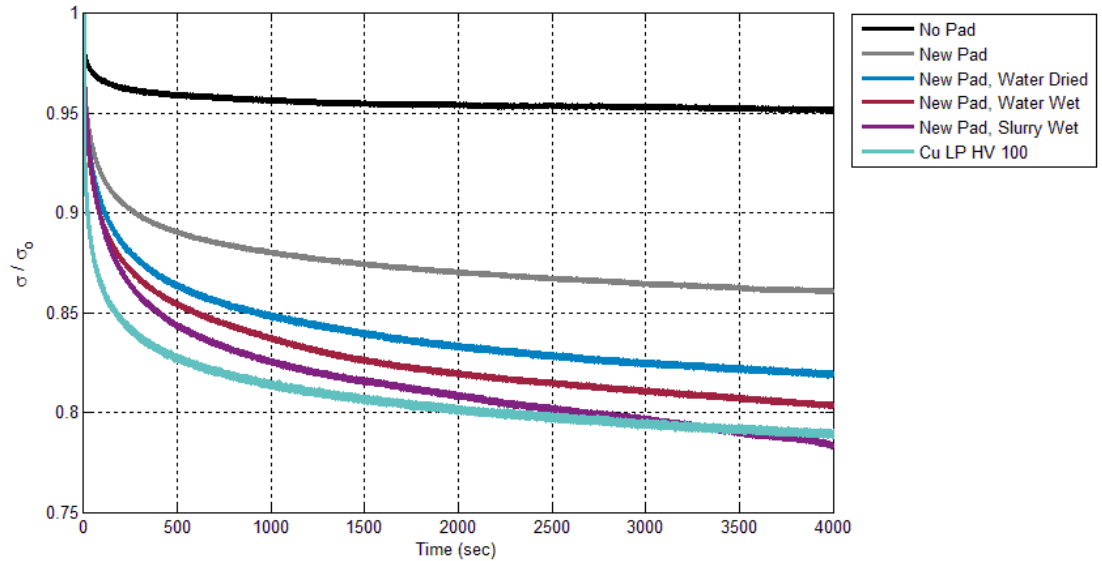

Figure 28: Reduced Trials of Normalized Stress Relaxation of Pad Material in Compression at 4 psi

Table 4: Standard Deviation of Time Averaged Normalized Stress at 4 psi

Sample Type	Average Standard Deviation of Normalized Stress
No Pad	0.0227
New Pad	0.0238
New Pad, Distilled Water Dried	0.0067
New Pad, Distilled Water Wet	0.0256
New Pad, Slurry Wet	0.0096

From the presented data it is clear that compression test setup by itself with no pad has less relaxation over time than all other trials. The additional relaxation seen in all trials is a result of the pad material relaxing under the compressive strain. It is also clear that new pad material which has never been soaked in an aqueous liquid relaxes less than those that have been. A mathematical model to describe the relaxation of stress over time is proposed in Equation 31,

$$\sigma = \sigma_o \left[k \cdot log_{10}\left(\frac{t}{t_o} + 1\right) + b \right] \quad \text{Equation 31}$$

σ is stress, σ_o is initial stress, t is time, t_o is unit time, k is the slope, and b is an intercept. Time is divided by unit time to keep the quantity inside of the logarithm unitless. The units of a logarithm of a physical dimension is meaningless by the definition of a logarithm (Matta et al. 2011, 67-70). The number one is added to the dimensionless time because when time is zero, the logarithmic term is zero. If the number one was not included, the logarithmic term would be negative infinity at time equal to zero, and it would be a negative value for logarithmic terms of between zero and one, none of which makes sense physically. Since all logarithmic terms of one and greater are positive,

adding the one is necessary (Stroud and Booth 2001). With the added number unity, the initial value of stress is the product of σ_o and b.

To check the potential validity of this relaxation model, the normalized stress is plotted against a logarithmic scale of $t/t_o + 1$. If the normalized stress follows the behavior of Equation 31, the curves will become straight lines. The data of Figure 27 is plotted with a logarithmic time scale in Figure 29. For easier viewing of the results, the data of Figure 28 is plotted with a logarithmic time scale in Figure 30.

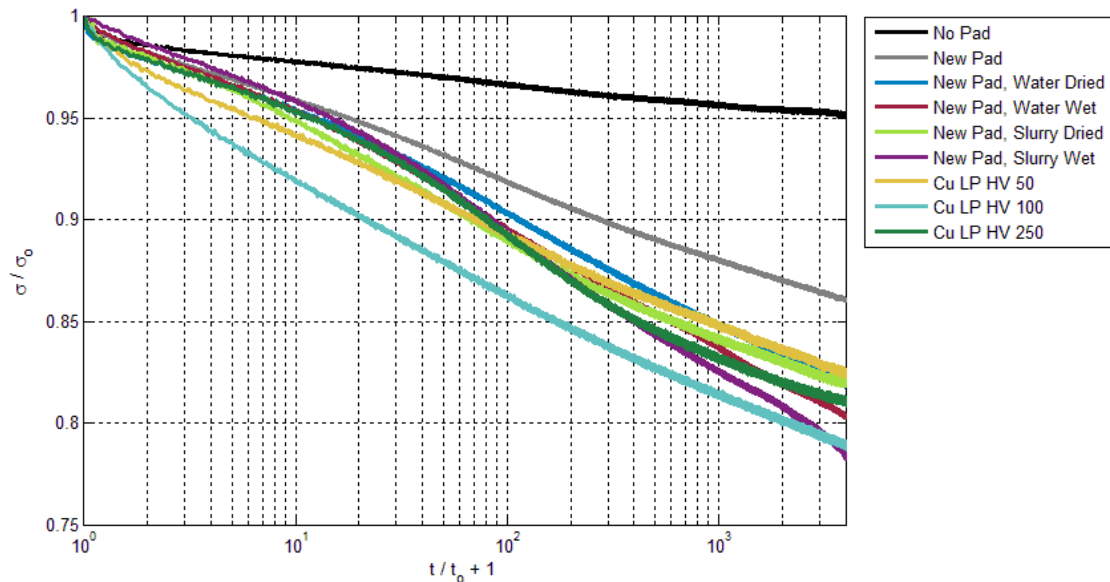

Figure 29: Normalized Stress Relaxation of Pad Material in Compression with Logarithmic Scale of $t/t_o + 1$ at 4 psi

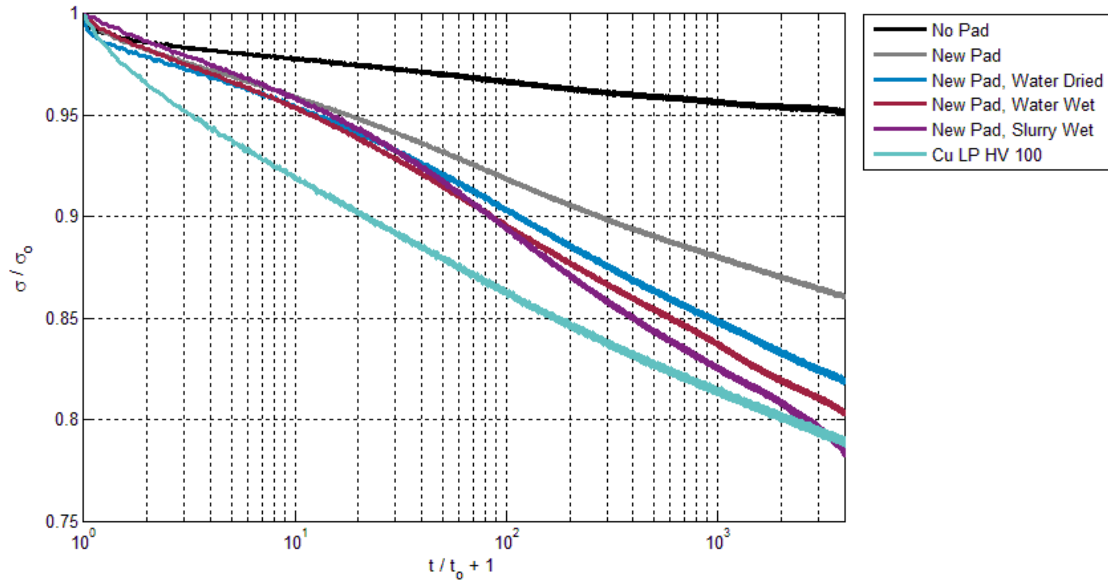

Figure 30: Reduced Trials of Normalized Stress Relaxation of Pad Material in Compression with Logarithmic Scale of $t/t_o + 1$ at 4 psi

Normalized stress on the logarithmic time scale in Figure 29 appears to show two potentially different scales of relaxation. Some trials show a short time relaxation that transitions into a long time relaxation. This transition completes at around 100 seconds, from observation of the slopes of multiple lines in Figure 29 and Figure 30. Some trials appear not to have this change of slope, while some do. Slopes of the curves in the semi-logarithmic figures represent the rate at which the system and the pad material are relaxing logarithmically with time. A shallower slope represents a slower relaxation relative to a steeper slope. For some, the slopes of the short time relaxation in Figure 29 are shallower. An example of a shallower short time slope is the 'New Pad, Slurry Wet' relaxation data. For this trial, the logarithmic function which represents the short time relaxation is relaxing slower than the long time behavior. Although the linear axes of time shows the pad material relaxes more from 0 seconds to 100 seconds, the

logarithmic rate of relaxation is slower for some trials. In other words, if a logarithmic function that has the slope of the long time relaxation were plot alongside this raw relaxation data, the long time relaxation function would relax more in the first 100 seconds.

The system itself with no pad shows a fairly level relaxation which suggests that it only has a single relaxation time. Many trials with the pad material show two relaxation times, which may be a result of the pad material's actual mechanical behavior under stress relaxation. The short relaxation time may also be an artifact of the creep that occurs within the first 10 minutes of these experiments, as shown in Figure 26. With increasing compressive strain of the sample, the pad material would not able to relax as much as if the strain were held constant. Since it is impossible to determine the strain of the pad sample itself, the cause of the multiple relaxation times cannot be confirmed. Although since the creep of the system is consistent from the results of multiple trials, the relaxation trials can be compared between each other.

The curves of normalized stress against the logarithmic scale of time plus one appear approximately linear. The linear behavior on the logarithmic time scale suggests that Equation 31 is a sufficient model for the data. To fit this mathematical model to the stress relaxation data, a linear regression between normalized stress and the base 10 logarithm of time plus one is conducted for each type of pad tested. The result is the slope and the intercept of the line.

To achieve proper values for the relaxation of the pad material alone, the fit slope of the compression setup must be subtracted from the fit slopes of the pad trials. Since the stress relaxation is a linear combination of the system and pad with constantly held

displacement, this subtraction removes the relaxation contribution of the system. The results of the corrected relaxation times of the pad samples and the relaxation time of the system with no pad is given in Table 5 and Table 6. Table 5 provides the short term relaxation fit values, while Table 6 gives the long time relaxation values. Short time is considered from 0 seconds to 100 seconds, and long time is from 100 seconds to 4000 seconds. A fit is also conducted through the entire 4000 seconds for comparison, as if there were only a single relaxation time. These full time fit slopes are provided in Table 7. Intercepts and coefficients of determination for the linear regressions are also provided. An example of the curve fits for the new pad material compression relaxation data are shown in Figure 31, Figure 32, and Figure 33. The value of t_o for all fits is a single unit of the time, which is one second, since the units of time used are seconds.

Table 5: Short Time Compressive Stress Relaxation Model Fit Values for Pad Material at 4 psi

Sample Type	k	b	R^2
No Pad	-0.011	0.990	0.992
New Pad	-0.028	0.998	0.996
New Pad, Water Dried	-0.036	1.001	0.989
New Pad, Water Wet	-0.043	1.007	0.991
New Pad, Slurry Dried	-0.045	1.004	0.996
New Pad, Slurry Wet	-0.047	1.016	0.981
Cu LP HV 50	-0.037	0.990	0.998
Cu LP HV 100	-0.047	0.979	0.997
Cu LP HV 250	-0.044	1.007	0.978

Table 6: Long Time Compressive Stress Relaxation Model Fit Values for Pad Material at 4 psi

Sample Type	k	b	R^2
No Pad	-0.007	0.981	0.981
New Pad	-0.026	0.983	0.998
New Pad, Water Dried	-0.043	1.001	0.998
New Pad, Water Wet	-0.048	1.007	0.999
New Pad, Slurry Dried	-0.032	0.964	0.994
New Pad, Slurry Wet	-0.056	1.017	0.996
Cu LP HV 50	-0.032	0.969	0.997
Cu LP HV 100	-0.035	0.945	0.997
Cu LP HV 250	-0.036	0.966	0.977

Table 7: Full Time Compressive Stress Relaxation Model Fit Values for Pad Material at 4 psi

Sample Type	k	b	R^2
No Pad	-0.009	0.984	0.978
New Pad	-0.027	0.988	0.995
New Pad, Water Dried	-0.043	1.004	0.998
New Pad, Water Wet	-0.048	1.009	0.999
New Pad, Slurry Dried	-0.035	0.975	0.985
New Pad, Slurry Wet	-0.056	1.022	0.996
Cu LP HV 50	-0.033	0.975	0.995
Cu LP HV 100	-0.037	0.953	0.993
Cu LP HV 250	-0.040	0.983	0.969

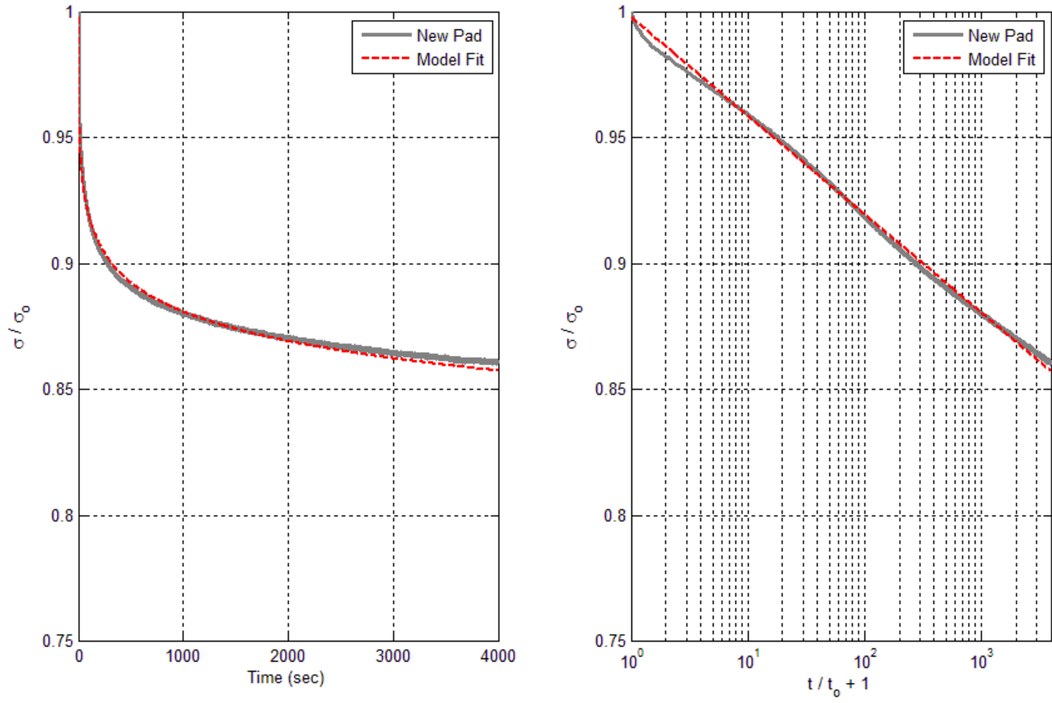

Figure 31: Short Time Compressive Relaxation Curve Fitting of Pad Material at 4 psi

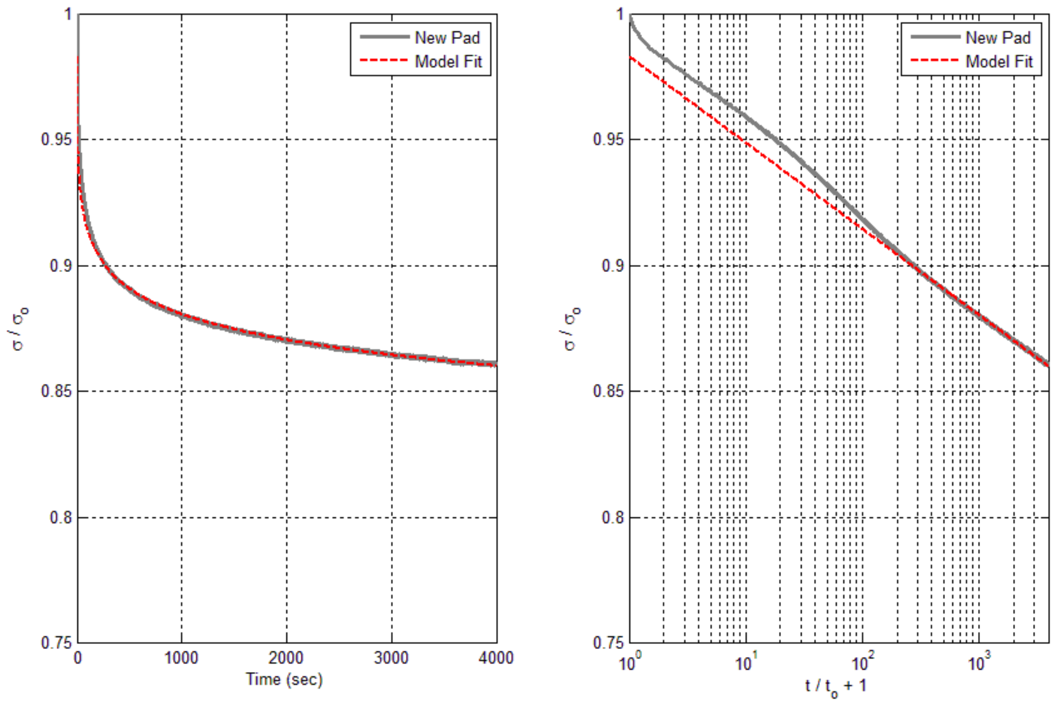

Figure 32: Long Time Compressive Relaxation Curve Fitting of Pad Material at 4 psi

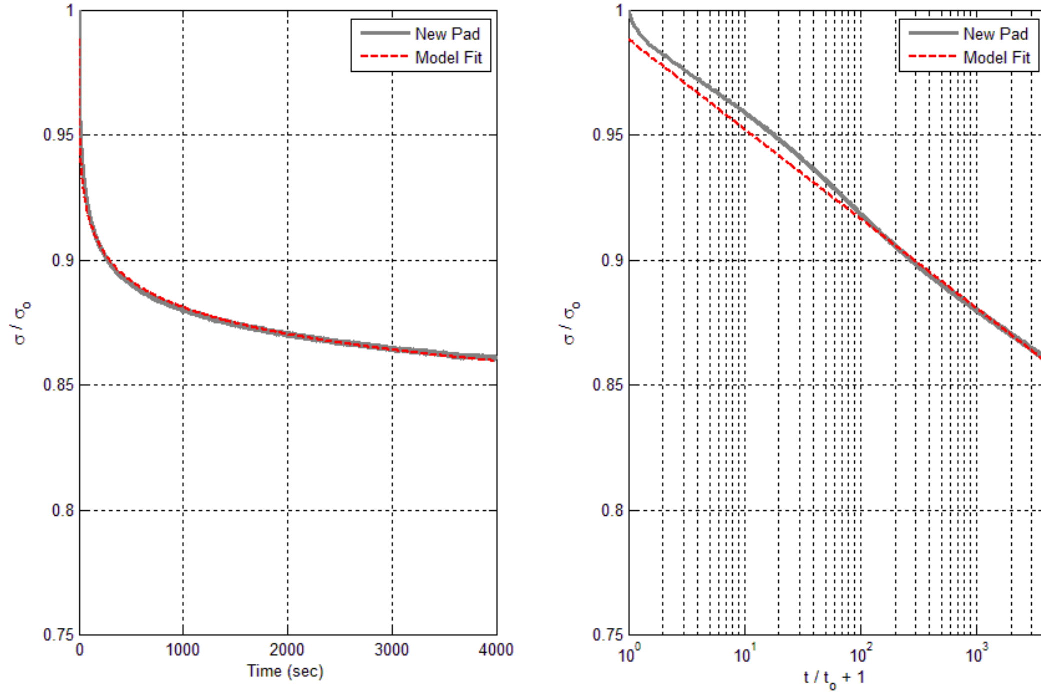

Figure 33: Full Time Compressive Relaxation Curve Fitting of Pad Material at 4 psi

The results show sufficient fits of the models with coefficients of determination near 1 in Table 5, Table 6, and Table 7, representing a close linear correlation of the model. Figure 31, Figure 32, and Figure 33 visually show close the model fits to the stress relaxation data with time. The physical meaning of k can be interpreted by rearranging Equation 31 to solve for time. The result is given in Equation 32,

$$t = t_o 10^{\left(\frac{\sigma/\sigma_o - b}{k}\right)} - t_o \qquad \text{Equation 32}$$

This equation explains that k is the value of σ/σ_o minus b when time is equal to 9 seconds, using t_o equal to 1 second. Thus, k has a very specific definition that may be challenging to interpret physically. To gain a better physically representative parameter from the experimentally fit results, a time constant is defined with the symbol τ_n, where

the subscript n is set as a desired percentage. This time constant is defined as the time that the material takes to relax its normalized stress n percentage of its initial value. From the model of Equation 31, the initial value of normalized stress at time equal to zero is b. The definition of τ_n is mathematically described in Equation 33,

$$\tau_n = t_o 10^{\left(\frac{(1-n)b-b}{k}\right)} - t_o = t_o 10^{\left(-\frac{nb}{k}\right)} - t_o \qquad \text{Equation 33}$$

The value of n is chosen based on the percentage of initial relaxation that is of interest. A value of n equal to 10% or 0.1 is chosen to compare each sample's relaxation behavior for short, long, and full time. The value of n equal to 10% is selected since it produces time constant values of the pad relaxation trials that are simple for comparison, typically being on the order of 100 seconds. The values of $\tau_{0.1}$ are tabulated in Table 8.

Table 8: 10% Relaxation Time Constant for Pad Relaxation Models at 4 psi

	$\tau_{0.1}$ (seconds)		
Sample Type	Short Time	Long Time	Full Time
No Pad	4.45×10^{8}	8.89×10^{11}	1.07×10^{11}
New Pad	4191	6202	4842
New Pad, Water Dried	584	224	220
New Pad, Water Wet	214	121	122
New Pad, Slurry Dried	173	997	622
New Pad, Slurry Wet	139	68	65
Cu LP HV 50	482	1042	858
Cu LP HV 100	118	481	379
Cu LP HV 250	198	508	279

These results provide a quantitative comparison between the samples at long and short times of relaxation. Smaller time constants means that the material is relaxing

more over time, since it takes a shorter time to relax 10% of its initial value. Regression fits with steeper slopes, or smaller values of k, coincide with smaller time constants since a steeper slope means the sample is relaxing more over time. The time constants of the full time models fit in between the long and short times of relaxation. There is no particular trend observed in whether the short time values of $\tau_{0.1}$ are larger or smaller than the long time values. Comparisons are better obtained between sample types using the full time relaxation data. For all time fits, the system with no pad relaxes at the slowest rate since it has much larger time constants than any trial with a pad sample. The slowest relaxation rate, or largest time constant, of pad samples are the new pad samples for all of the model fits. This leaves the fact that all pad samples that have been at some point soaked in an aqueous liquid relax more than the new pad material.

For the new samples that were soaked in distilled water or in slurry, the wet pad materials relaxed more than the dry pad materials. For full time relaxation, the wet samples have a smaller time constant than any dried pad sample. It appears that the slurry may increase its relaxation rate in time when it is wet compared to the distilled water, which has a larger wet relaxation time. This observation becomes the opposite when observing the dried sample results.

Used pad samples are shown to relax on the same order as dried new pad samples. For all three time scales fit, the 50 wafer count sample relaxes less than the two higher wafer count samples. The 100 and 250 wafer count samples have similar time constants. This suggests that the pad material relaxes more as it is used, but begins to level off after a certain amount of polishing time. These results can be compared to experiments that are reported in the literature for a "broken-in" pad (Eusner, Saka, and

Chun 2011, H379-H389). An IC1000 pad was polished against copper wafers for a polish time similar to the 100 wafer planarization experiment pad samples. After this conditioning process, the scratches produced on wafers by pad asperities decreased. The compressive relaxation results of this work suggest that the part of the process which decreases pad scratching may be due to the increased stress relaxation of the pad through polishing time. A major result of these experiments is the suggestion that the conditioning process may be in part due to the viscoelastic properties of the pad material. Additional work on this matter would have to be conducted to confirm these results.

Another major result from these compression relaxation experiments is that all pad samples which have been soaked in an aqueous liquid have smaller time constants than the new and untouched pad samples. This statement is true even for the new and dried pad samples. Previous research has been conducted on the mechanical effects of soaking CMP polishing pads in slurry and water. The earliest literature found examines the topic of stiffness changes in IC1000 pads with water soak time (Li et al. 1995, 601-606). Results showed that the storage modulus of IC1000 pad material decreases exponentially with time. This decrease in storage modulus beings to level off after 800 minutes of soak time in deionized water. It was also found that the material removal rate of CMP is not affected by the soaking time, and suggests that material removal is not a function of the bulk pad properties, but rather by more of the surface properties. Several other papers show the same trend of a decrease in modulus of bulk pad material with slurry and water soak time (Kim et al. 2008, 454-463; Moinpour et al. 2002, 766-71). Castillo-Mejia, et. al. observe a decrease in stiffness in IC1000 pads with water soaking

and investigate the causes (Castillo-Mejia et al. 2003, G76-G82). This research suggests that water breaks the hydrogen bonds that connect urethane groups of the IC1000 pad. Disruption of these bonds make it easier for the polymer strands to move past each other and thus decreases the pad modulus after soaking. This theory is supported by infrared spectroscopy results of the soaked and un-soaked pad.

4.1.1.2 Polishing Pad Compressive Relaxation with Stress Magnitude

Additional compression relaxation trials were performed at larger initial loads and stresses. A trial with no pad material was conducted at a maximum initial load of 5.25 lb_f. Using the area of six squares of pad material, this is equivalent to a nominal stress of 14 psi. This trial is used to characterize the system's relaxation at higher loads. Two trials are performed on a pad sample of six and three squares to a maximum load of 4.35 lb_f and 4.65 lb_f, respectively. Based on the nominal area of the pad sample for each square, the initial stress for the six square sample is 11.5 psi while the three square sample is stressed to 24.8 psi. These levels of initial load and stress can be compared to the 4 psi initial stress experiments which have an average initial load of 1.95 lb_f. The normalized stress values of the higher stress trials are plotted on a linear scale of time in Figure 34. The same data is plotted against a semi-logarithmic scale of $t/t_o + 1$ in Figure 35 to compare to the model of Equation 31.

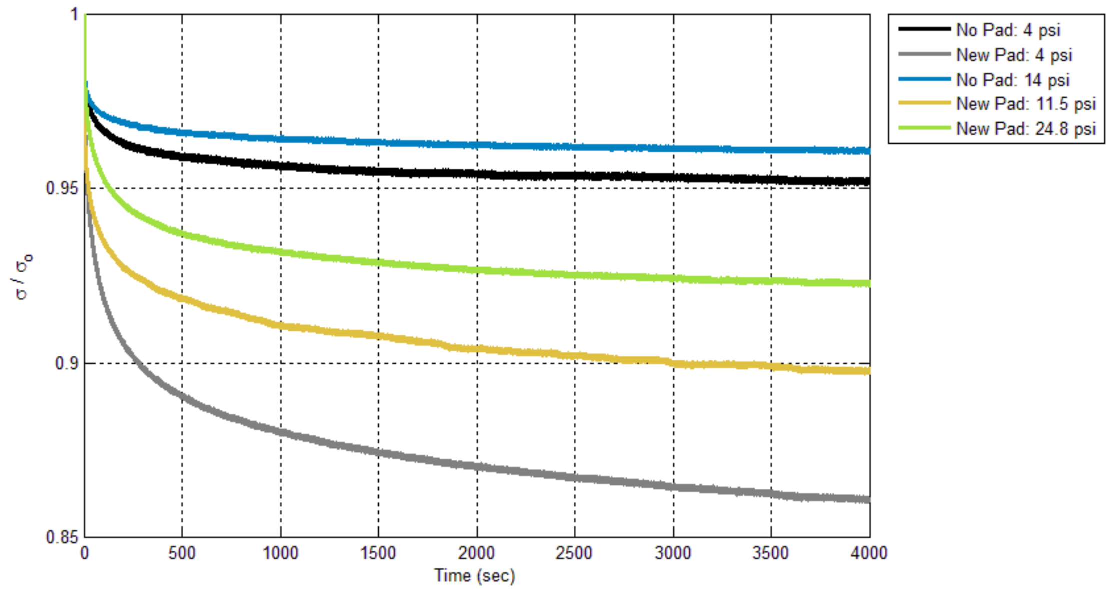

Figure 34: Normalized Stress Relaxation of Pad Material in Compression at a Range of Initial Stresses

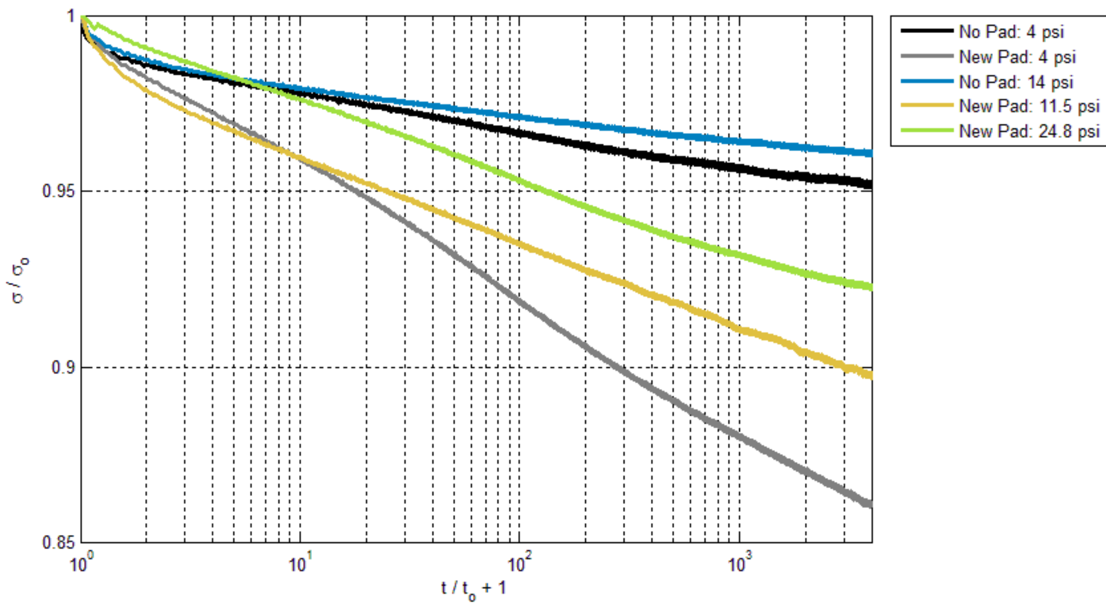

Figure 35: Normalized Stress Relaxation of Pad Material in Compression with Logarithmic Scale of $t/t_o + 1$ at a Range of Initial Stresses

From the data presented in Figure 34 and Figure 35, it appears that a higher stress level results in less relaxation from its initial value over time. To quantify this observation, the same linear regression is performed on normalized stress versus the base 10 logarithm of $t/t_o + 1$. The high stress trial slope is subtracted from the fit slopes of high stress pad samples to obtain the proper relaxation data of the pad samples alone. The results of short time, long time, and full time relaxation model fits are tabulated in Table 9, Table 10, and Table 11, respectively. Graphs that compare the fit models to the actual data are given for the range of fitting times in Figure 36 to Figure 38. The 10% time constant values for these trials are given in Table 12. All of these results are shown along with the corresponding low stress compression trials for comparison. Initial stress values given for the no pad trials are based on the area of six pad square samples, which is 0.375 inches^2.

Table 9: Short Time Compressive Stress Relaxation Model Fit Values for New Pad Material at Various Initial Stresses

Sample Type	σ_o (psi)	k	b	R^2
No Pad	4	-0.011	0.990	0.992
No Pad	14	-0.009	0.989	0.976
New Pad	4	-0.028	0.998	0.996
New Pad	11.5	-0.014	0.985	0.995
New Pad	24.8	-0.011	0.999	0.998

Table 10: Long Time Compressive Stress Relaxation Model Fit Values for New Pad Material at Various Initial Stresses

Sample Type	σ_o (psi)	k	b	R^2
No Pad	4	-0.007	0.981	0.981
No Pad	14	-0.006	0.983	0.991
New Pad	4	-0.026	0.983	0.998
New Pad	11.5	-0.015	0.981	0.998
New Pad	24.8	-0.009	0.984	0.990

Table 11: Full Time Compressive Stress Relaxation Model Fit Values for New Pad Material at Various Initial Stresses

Sample Type	σ_o (psi)	k	b	R^2
No Pad	4	-0.009	0.984	0.978
No Pad	14	-0.007	0.984	0.986
New Pad	4	-0.027	0.988	0.995
New Pad	11.5	-0.015	0.982	0.999
New Pad	24.8	-0.010	0.989	0.985

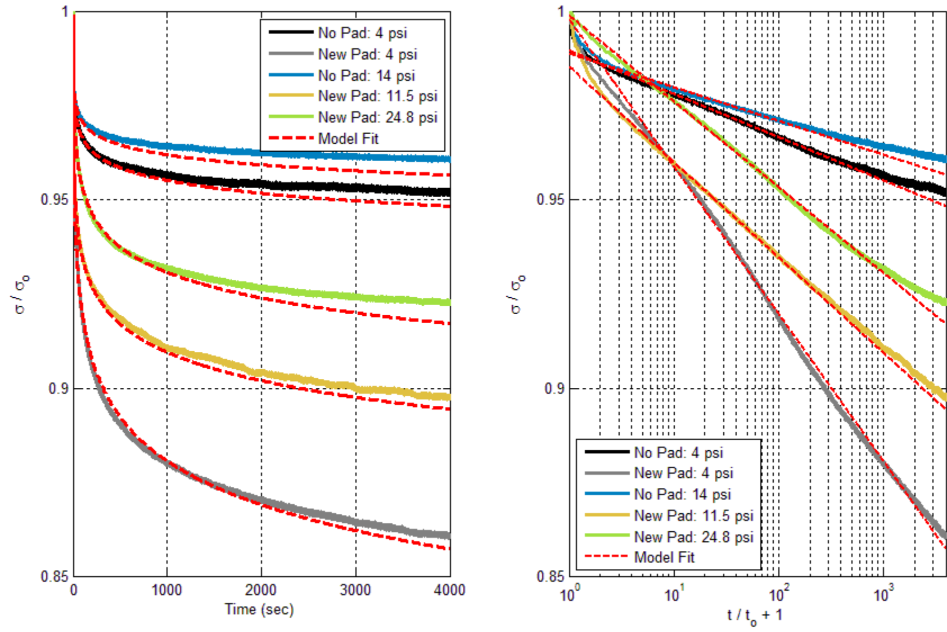

Figure 36: Short Time Compressive Relaxation Curve Fitting of Pad Material at a Range of Initial Stresses

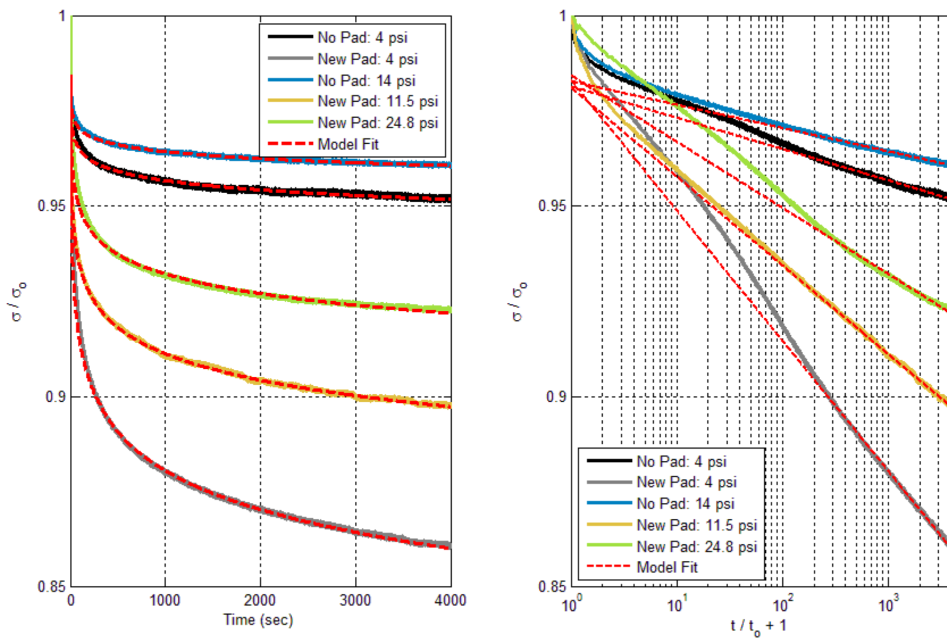

Figure 37: Long Time Compressive Relaxation Curve Fitting of Pad Material at a Range of Initial Stresses

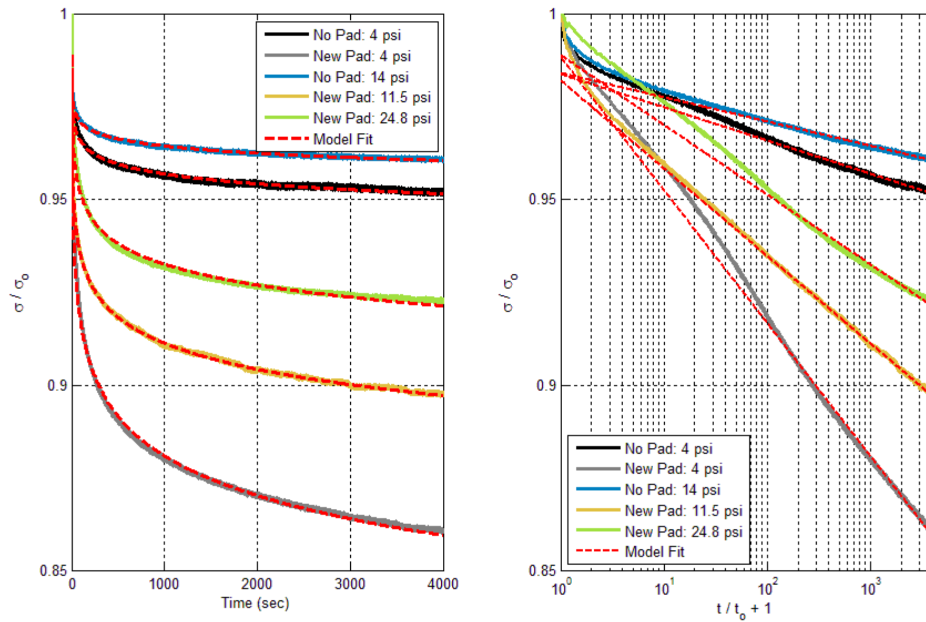

Figure 38: Full Time Compressive Relaxation Curve Fitting of Pad Material at a Range of Initial Stresses

Table 12: 10% Relaxation Time Constant for Pad Relaxation Models at a Range of Initial Stresses

Sample Type	Initial Stress (psi)	$\tau_{0.1}$ (seconds)		
		Short Time	Long Time	Full Time
No Pad	4	4.45×10^{8}	8.89×10^{11}	1.07×10^{11}
No Pad	14	1.18×10^{11}	1.21×10^{16}	1.29×10^{15}
New Pad	4	4191	6202	4842
New Pad	11.5	1.39×10^{7}	3.35×10^{6}	5.26×10^{6}
New Pad	24.8	7.75×10^{8}	6.32×10^{10}	1.19×10^{10}

The gathered stress relaxation model slopes and the 10% time constant values explain that the pad material relaxes from its initial value less over time at higher initial stresses. This trend is the case for all fit time ranges.

Results of all compression relaxation trials of the IC1000 polishing pad show time dependent mechanical behavior. The compression relaxation behavior is indicative that viscoelastic strain energy term, represented by $\boldsymbol{\sigma}^{\mathbf{p}}\mathbf{:D}^{\mathbf{e}}$, is significant for the CMP polishing process. The dissipation of input energy into viscous deformation of the pad material is important as the stress relaxation is substantial within the time scale of polishing. The viscoelastic strain energy appears to change through the course of a pad's duty cycle. As a pad is soaked longer, the material relaxation rate increases. Also, results indicate that the pad material relaxes more after polishing 100 wafers. The viscoelastic strain energy is also a function of the applied normal load on the pad during CMP. Thus, it is determined that the viscoelastic strain energy dissipated is of importance to the overall thermomechanical model of CMP and must be taken into account.

4.1.2 IC1000 Pad Compressibility Results

The several measures of IC1000 polishing pad compressibility are experimentally approximated using the optical compression test setup. A rectangular sample of pad material is placed between the compression plates. This sample is compressed at a relatively constant rate using the micrometer until the sample has reached at least 15% strain. The entire compression occurs on the order of 10 seconds. While the pad is compressed, a video is taken of a face of the sample as well as the compression plate edges. The images from the video are processed using MATLAB Image Processing Toolbox to measure the average compressive axial strain and change in average width of the pad sample's face. The volume of the material is approximated

as the face area multiplied by the average face width squared. The result is information on the change in volume of the pad sample as a function of compression strain. The Jacobian is determined by dividing the volume by the original volume.

Strain measurements are sufficient using the optical microscope and digital camera setup for these experiments because the samples tested are much less stiff than in the stress relaxation experiments. Also, load measurements are unnecessary for these experiments, so the load cell which is suspected of bending with applied load was removed. The compression block thus sits directly up against the load cell fixture that is attached to the base plate. If any bending of the system occurs, the effects are minimal due to the small size of the samples tested.

A total of eight pad samples were cut from the pad and compressed to at least 15% strain. All trials used a limit of 0.4 for the *im2bw* function for conversion to a binary image. The evolution of a pad sample's face through a trial can be seen in Figure 39. The results of the experiment is the linear regression conducted on the Jacobian vs. axial strain data for each of the 8 trials. An example of the results for Trial 5 is seen in Figure 40, which presents data that has similar features to all other trials. Each data point is a computation of the Jacobian and compressive strain from a single frame of the 20 frame per second video. All trials show an inverse correlation between the Jacobian and compressive strain that is closely a linear relation. The data points have a slight spread about the linear fit. This variation is likely due to random noise associated with the digital camera sensor, variations in lighting as the compression plates and pad sample move, and compliance of the compression system. Quantitative results of the linear regression slope and intercept for each trial are given in Table 13.

Figure 39: Compression of Pad Sample (Trial 5)

Left: 0% Strain. Middle: 10% Strain. Right: 18% Strain.

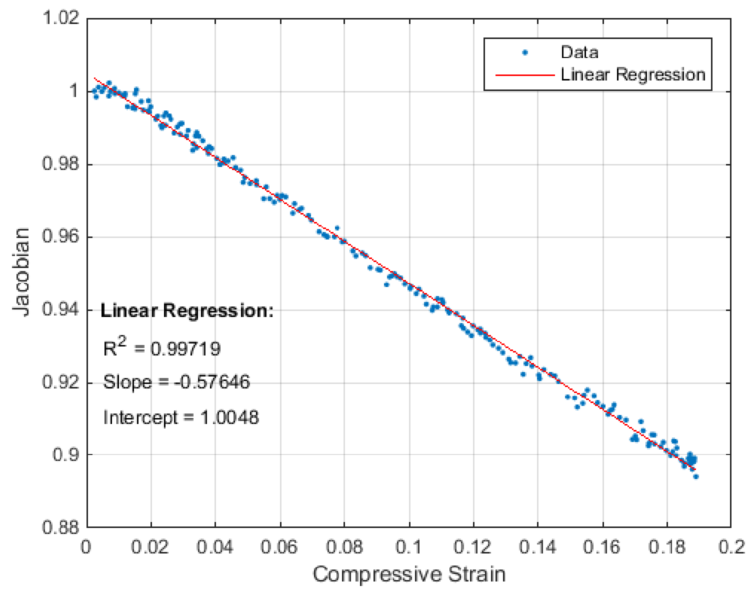

Figure 40: IC1000 Jacobian versus Axial Compressive Strain Data and its Linear Regression (Trial 5)

Table 13: Linear Regression Results for Jacobian versus Compressive Strain of IC1000

Trial	Slope	Intercept	R^2
1	-0.697	1.00	0.999
2	-0.747	1.00	0.995
3	-0.697	0.99	0.992
4	-0.518	1.00	0.997
5	-0.576	1.00	0.997
6	-0.394	1.01	0.993
7	-0.513	0.99	0.994
8	-0.583	1.00	0.998
Average	-0.590	1.00	0.996
Standard Deviation	0.118	0.01	0.002

Table 13 shows that there is a strong inverse linear correlation between the Jacobian and compressive strain as the coefficient of determination (R^2) is very close to 1. All of the slopes of the linear fit are relatively close together with the standard deviation being approximately 20% of the average magnitude. This deviation is suspected to be a result of the varying shapes of pad samples. The linear regression for each sample is very good, indicating the systems of measurement are not a cause of the variation. It is expected that the volume of the pad sample decreases with applied compressive strain, of which the experimental data shows. The linear trend seen within the strain range tested indicates that the volume of the samples changes directly with the applied deflection. Pores of air in the polyurethane foam are compressed, yet it appears they are not completely collapsed under these strains. With collapsed pores, the slope of the line is expected to change as more material comes into contact per differential area to resist volume change. So it appears that collapsed pores do not occur

up to at least 20% strain. It is less than this pad strain level in which CMP deformation occurs, so this experimental data is sufficient for the strain levels needed.

The relatively small standard deviation of the linear slope values and all R^2 very close to 1, the data achieved for compressibility is suitable as an approximation. The equation utilized for the IC1000 Jacobian in further analysis is the average of the linear regression values for all trials. This relation between the Jacobian and compressive strain is given in Equation 34,

$$J = -0.590(\varepsilon_c) + 1.00 \qquad \text{Equation 34}$$

J is the Jacobian and ε_c is compressive strain. This computation does not account for the non-uniform strain fields and imperfect sample geometry. Since the Jacobian is a local measurement of deformation, this is an approximation as an average compressibility of pad samples.

An approximation of the Poisson's ratio is also computed from the same experimental data used for the Jacobian computation. Using the transverse strain of the pad sample, which is equivalent to the change in width over the original width. The transverse strain of the pad sample is plot against the axial compressive strain. A linear regression is conducted for each of the 8 trials. An example plot of compressive strain versus transverse strain from Trial 5 is shown in Figure 41. The results of the linear regression slopes are equivalent to the average Poisson's ratio of an experiment multiplied by negative one. Results are tabulated in Table 14.

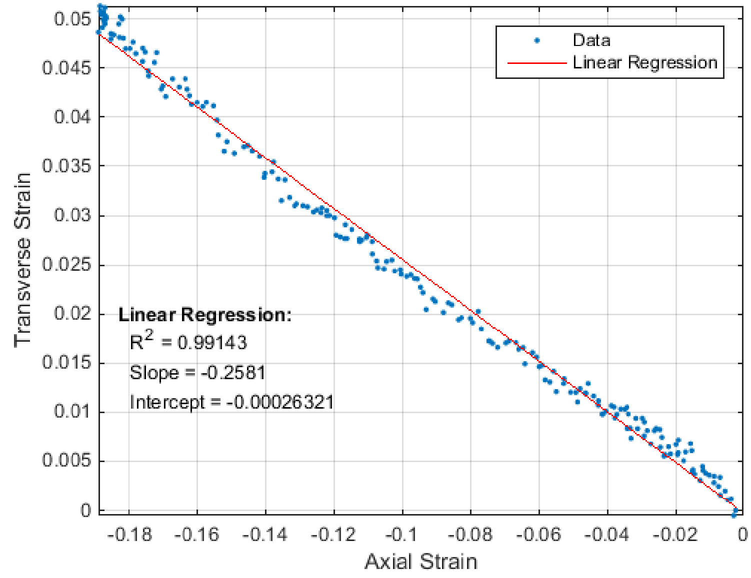

Figure 41: Transverse Strain versus Axial Strain Linear Regression for the IC1000 Pad Poisson's Ratio (Trial 5)

Table 14: Linear Regression Results for Transverse Strain versus Axial Strain of IC1000

Trial	Slope $\left(\nu = -\frac{d\varepsilon_{trans}}{d\varepsilon_{axial}}\right)$	R^2
1	0.19	0.994
2	0.15	0.974
3	0.18	0.947
4	0.28	0.993
5	0.25	0.992
6	0.37	0.997
7	0.30	0.987
8	0.25	0.992
Average	0.25	0.984
Standard Deviation	0.07	0.017

For each sample, the linear regression fits well with all coefficients of determination above 0.94 with most being above 0.99. The results show an average Poisson's ratio of IC1000 to be 0.25, taken as the approximate value for IC1000. This value falls within the range of reported Poisson's ratios in the literature for IC1000, which range from 0.15 to 0.3 (Eusner, Saka, and Chun 2011, H379-H389; Bastawros et al. 2002, 1022-1031; Ring et al. 2007, H239-H248; Deshpande et al. 2005, 261-9).

Finally, the unit volume change of the material is computed based on the strain data in thickness and in width. Equation 15 is used with E_1 equal to the strain in the thickness. E_2 and E_3 are set as the strain in width. The resulting values include the higher order terms of strain. Equation 16 is used to compare this unit volume change to its first order approximation. This approximation is known as dilatation, or the trace of the infinitesimal strain tensor in the principal direction as shown earlier in Equation 15. Figure 42 depicts unit volume change of the pad sample from Trial 5 versus the compressive strain. The first order approximation is plotted along with the higher order relation. Linear regression of the unit volume change and compressive strain are conducted for each trial. The regression results are presented in Table 15.

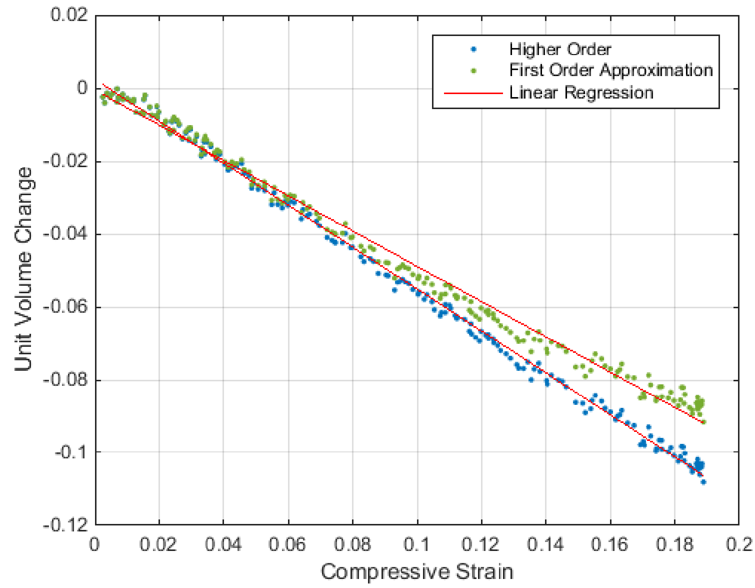

Figure 42: Unit Volume Change of an IC1000 Pad Sample (Trial 5)

Table 15: Linear Regression Results for Unit Volume Change

	Higher Order			**First Order Approximation**		
Trial	Slope	Intercept	R^2	Slope	Intercept	R^2
1	-0.693	-0.002	0.999	-0.621	-0.005	0.998
2	-0.748	0.002	0.995	-0.691	0.001	0.995
3	-0.697	-0.011	0.992	-0.638	-0.014	0.982
4	-0.519	-0.002	0.997	-0.434	-0.004	0.988
5	-0.577	0.001	0.997	-0.493	-0.002	0.991
6	-0.392	0.001	0.993	-0.276	-0.003	0.979
7	-0.512	-0.010	0.994	-0.399	-0.014	0.970
8	-0.580	-0.004	0.998	-0.501	-0.007	0.992
Average	-0.590	-0.003	0.996	-0.507	-0.006	0.987
Standard Deviation	0.118	0.005	0.002	0.139	0.005	0.009

Figure 42 displays that the unit volume change is negative with compressive strain, as expected. With larger strains, the first order approximation deviates from the higher order unit volume change that is based on Equation 15. This deviation is expected as the higher order terms have more influence on the result at larger strains. These results demonstrate the error that results in small strain approximations when strain levels become relatively large. The result is the linear approximation underestimates the amount of compression that is occurring, as shown by the smaller average slope.

The compressibility of the pad is found to be significant and measureable for IC1000 polishing pad material. From Equation 10 and Equation 34, a compressive strain of 3% results in an underestimation of true stress of approximately 2%, if the Jacobian is not taken into account. This behavior is the result of a reduction in area of the sample from the un-deformed state as it loses volume.

4.1.3 IC1000 Pad Tensile Stress Relaxation Results

Measurement of the bulk stress relaxation of the IC1000 pad material is performed by applying a constant tensile strain to a sample of the material, as discussed in Section 3.2.2.2. Six trials are performed at constant strain levels between 0.25% through 5.0% strain. The lower limit of 0.25% strain is chosen based on the magnitude of load that occurs at this strain level for the pad samples. A trial at a strain level that is lower will have its results compromised by the load cell accuracy. The upper limit of 5.0% strain is based on the tensile strength of IC1000 pad material. A pad sample breaks

around 6% or 7% strain when pulled in tension. A plot of the average stress in the IC1000 pad tensile samples over time for the six trials is given in Figure 43.

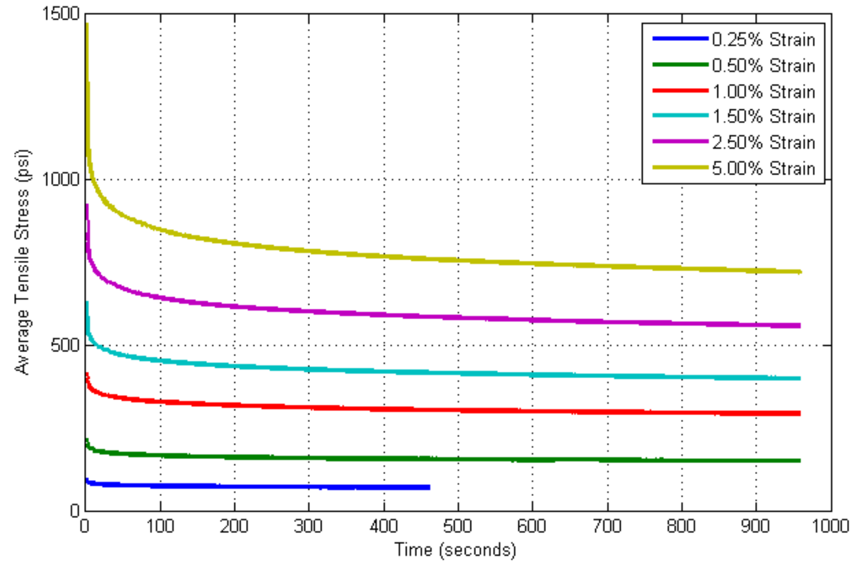

Figure 43: Average Stress Relaxation of IC1000 Pad in Tension over Time

Figure 43 shows that the trial for 0.25% constant strain was cut short due to an issue with the Instron machine's software. This data is still kept for analysis as it still provides useful information even if it is not for the full 16 minutes. As the constant strain is larger, there is also an increase in the initial tensile stress that is acting on the pad material. None of the trials have stress magnitudes that overlap each other. It is desired to fit the same stress relaxation model as the compression relaxation experimental data using Equation 31. Normalized stress versus time is shown in Figure 44. To examine the validity of a linear relation between normalized stress and the base 10 logarithm of $t/t_o + 1$, these parameters are plot on Figure 45.

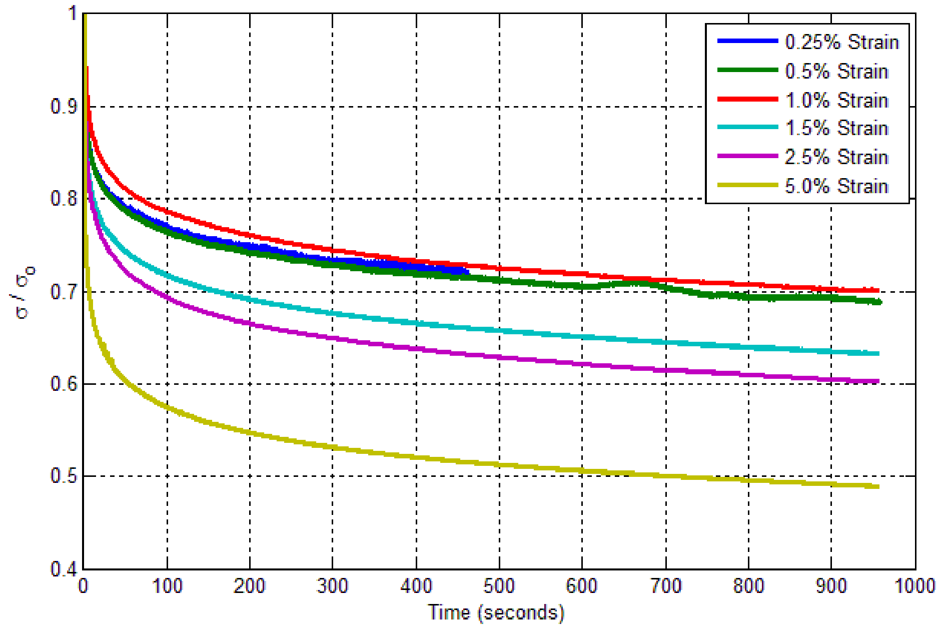

Figure 44: Normalized Stress Relaxation of IC1000 Pad in Tension with Time

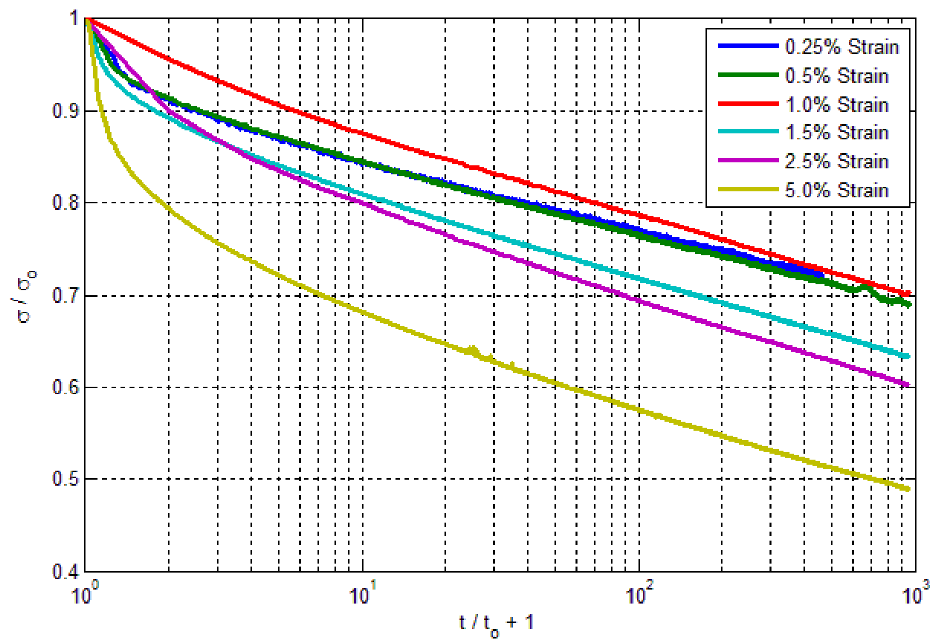

Figure 45: Normalized Stress Relaxation of IC1000 Pad in Tension with Logarithmic Scale of t/t_o + 1

After approximately one second, the normalized stress shows a linear trend with the semi-logarithmic axis of Figure 45. The first second of data shows non-linear behavior that is a result of the Instron machine overshooting and then correcting the held strain. Examples of this extra extension is illustrated in Figure 46, which plots the ratio of engineering strain to the desired held strain in the first few seconds of the experiment. The 1% strain trial shows the least amount of nonlinear behavior in the first second of data plotted in Figure 45, while 5% strain shows the most. The time of relaxation data is set at zero when the largest value of stress occurs. Figure 46 shows that the 1% strain trial had very minimal overshoot in strain, while 5% strain shows a relatively large overshoot that is also larger than any other trials. This extra strain that is added and then quickly removed by the Instron machine's feedback system is seen as the non-linear behavior within the first second of data plot on Figure 45 for the 5% strain trial. As the strain is released by the Instron machine, the pad material relaxes more than it would have at a held strain. This behavior is seen as an increased initial slope in relaxation for all trials.

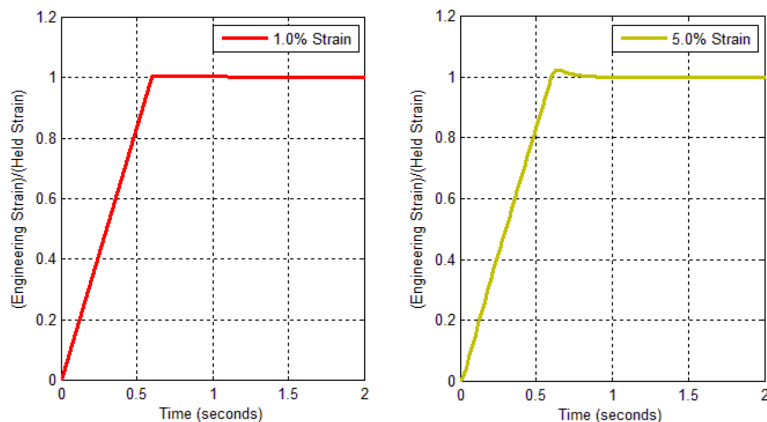

Figure 46: Instron Testing Machine Overshoot of the Set Held Strain

The extra strain added contributes to the error of the experimental fits, yet it is considered minimal as it is only the first second of data out of 16 minutes. Since the Instron machine corrects itself to give the proper strain, the remaining data is representative of the set strain hold value. This assumes any nonlinear effects with respect to time during the loading process are negligible. Two of the trials were conducted with a data collection rate of 1 Hz, while the others were set at a larger rate. All data applied to the fitting MATLAB code were reduced to be 1 Hz to remove any bias in the regression results that is obtained with additional data.

A linear regression is applied to the normalized stress versus the base 10 logarithm of $t/t_o + 1$. The results of the curves fit to the data are shown in Figure 47. Only a single linear regression of the data is taken over the entire range of time. The semi-logarithmic plot data has lines with approximately constant slopes for t greater than 1 second. The relaxation behavior for less than one second has been found to be an artifact of the Instron testing machine's initial strain correction. The linear regression slope and intercept values for all trials are provided in Table 16. 10% time constant values are given along with the regression values.

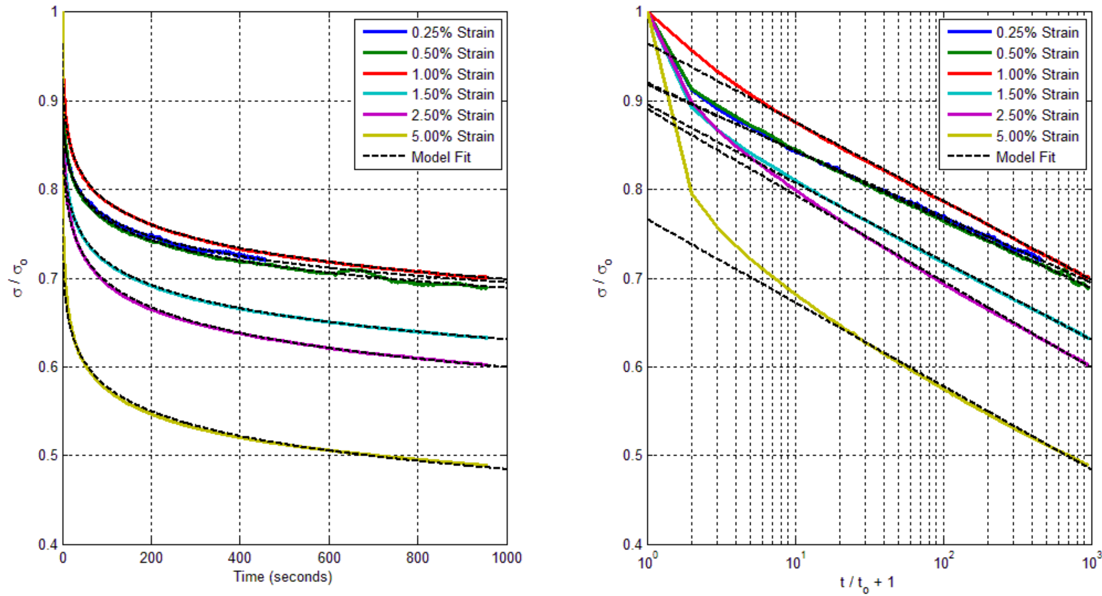

Figure 47: Regression Model of Tensile Stress Relaxation of IC1000 Pad Material. Left: Normalized Stress Versus Linear Scaled Time. Right: Normalized Stress versus Logarithmic Scaled $t/t_o + 1$.

Table 16: Tensile Stress Relaxation Fit Model Values for IC1000 Polishing Pad

Constant Strain (%)	σ_o (psi)	k	b	R^2	$\tau_{0.1}$ (seconds)
0.25	96.6	-0.074	0.918	0.997	18.11
0.50	217.3	-0.077	0.920	0.996	16.60
1.00	417.4	-0.089	0.965	0.999	13.21
1.50	630.5	-0.088	0.896	0.999	11.30
2.50	926.3	-0.097	0.891	0.997	9.27
5.00	1474.7	-0.094	0.767	0.993	7.54

All trials show a very good linear correlation between the normalized stress and base 10 logarithm of $t/t_o + 1$, with regression coefficients equal to 1 when rounded to two decimal places. Slopes of the regression models show a decrease in the slope with

a larger initial stress. A smaller slope represents more relaxation over time. This trend is mirrored with the decreasing trend of $\tau_{0.1}$ with increase initial stress. Smaller time constants means the material takes a shorter time to relax the same amount of stress as the behavior with a longer time constant. Values of the intercept deviate from the experimental data more for trials with a greater initial overshoot. This observation is logical, since the fitted model is weighted more from the data after one second, since those are the majority of the data points. The intercept thus provides a measure of error in the strain overshoot of the Instron testing machine within the first second of relaxation. Values of b are the expected starting point of normalized stress based on the data that is held at the proper strain, after approximately 1 second.

The behavior in tensile stress relaxation shows opposite trends in terms of stress magnitude than in compression. In compression, a large initial stress resulted in longer time constants of relaxation. Tensile stress relaxation is the opposite, as shown in Table 16. The literature mostly determines mechanical material behavior of the IC1000 pads in tension or bending modes of deformation. Yet, polishing pads are used in compression and in shear during CMP. These results of tensile and compression relaxation experiments highlight that there are differences in time dependent mechanical behavior of IC1000 pads depending on the mode of deformation. Thus, IC1000 pad materials should be characterized in compression as well as in shear for purposes of CMP modeling.

4.1.4 Quasi-static Tensile Testing of IC1000 Pad Material

A quasi-static tensile test of the IC1000 pad material is conducted to obtain a value for Young's modulus. The results of the experiment run in accordance with the procedure discussed in 3.2.2.2 is shown in Figure 48 as average engineering stress versus strain.

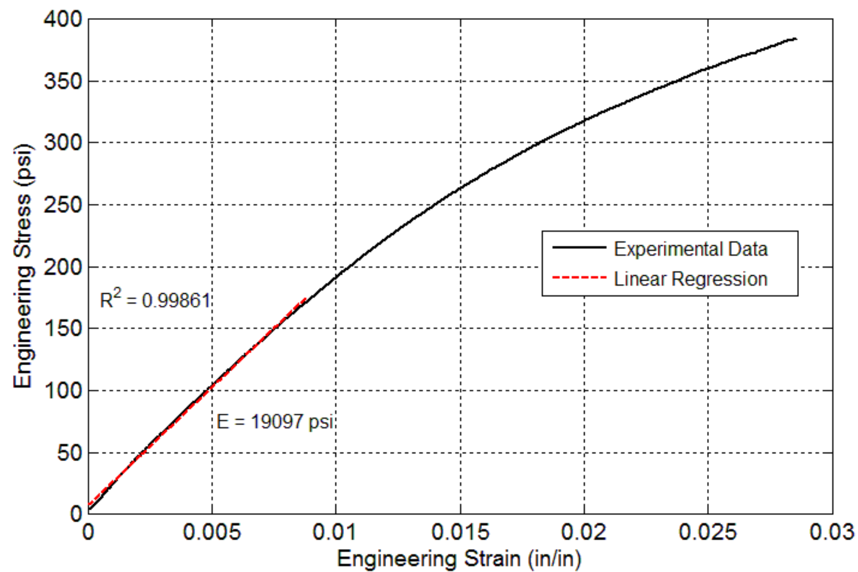

Figure 48: Quasi-static Tensile Test of IC1000 Pad

The stress versus strain shows an initial linear portion below 1% tensile strain. At about 1% strain, non-linear stress strain behavior begins to show. This behavior is most likely due to plastic deformation or bending of the pad sample due to its grooves. A linear regression on the stress strain data is performed to obtain a value for Young's modulus in the initial linear region. The regression is applied for the data between strain of 0 and 0.09. The desired result is the fit slope, which is equal to the estimated elastic

modulus. This elastic modulus is computed to be 19.1 x 10^3 psi. Literature states that IC1000 has an elastic modulus of about 52 x 10^3 psi, which is almost three times larger than what was found (Kim et al. 2008, 454-463; Castillo-Mejia et al. 2003, G76-G82; Charns 2005, 188-193). The literature does not state the thickness of the pad sample used when computing average stress. If the thinnest part of the pad sample were used, the modulus would be computed as 35.0 x 10^3 psi, which is closer to the reported values. Without sufficient knowledge of the literature's methods in experimentation, the value of 19.1 x 10^3 psi is used as the elastic modulus of IC1000 in tension.

4.2 Pad and Wafer Contact Stress Analysis

A contact stress analysis between the pad and wafer is conducted to predict the mechanical conditions that allow for scratches to be produced on the wafer surface. In this analysis, scratching is assumed to occur when the wafer material reaches its mechanical yield stress. It is at this stress level that the wafer plastically deforms. Frictional tractions are considered along with normal tractions in this analysis. Scratches that are produced by polishing pad asperities are on the microscale, which is the same scale as the pad asperity radius of curvature. To approximate the wafer stress field which produces scratches, the contact stresses associated with a single pad asperity are determined analytically. As discussed in Section 3.2.3, the average surface roughness of the IC1000 pad is two orders of magnitude larger than the wafer material surface (Kim, Saka, and Chun 2011, 393-404; Lay and Duquette 2006, 1-9; Nasrullah, Tyler, and Nishi 2005, 303-311). The geometry of the contact is assumed to be a spherical pad

asperity in contact with a flat wafer half-space, as is depicted in Figure 49. The asperity is loaded onto the wafer while moving at velocity V in the negative x direction. The origin is at the center of the circular contact with a contact diameter 2a. As discussed in Section 3.2.1, copper and silicon dioxide wafer materials are modeled as linearly elastic materials before yielding. With this, the wafer is modeled as an elastic half-space.

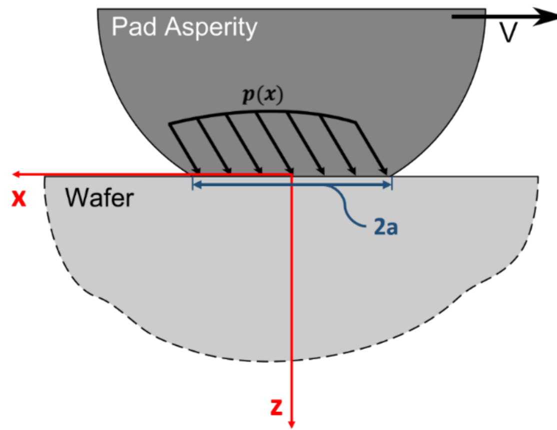

Figure 49: Pad and Wafer Contact Geometry and Coordinate System

It is shown through relaxation experiments that the IC1000 polishing pad has time dependent viscoelastic behavior. Also, the quasi-static tensile test of the IC1000 pad in Section 4.1.4, the pad material has an initial linear elastic behavior. To begin the contact stress analysis, the time dependent behavior is assumed to be negligible for small strains as the pad material behaves linear elastically. All materials are assumed to be isotropic and homogeneous. The stress field of a circular sliding contact with friction has been solved by Goodman and Hamilton (Hamilton and Goodman 1966, 371; Hamilton 1983, 53-59). Quasi-static stress fields in an elastic surface from tractions of a sliding spherical asperity are determined in closed form solutions. The solution is

based on the sum of a Hertzian normal pressure distribution and a tangential shear traction that is proportional to the normal pressure. These tractions act within the contact circle of radius a. The boundary conditions are mathematically described Equation 35, Equation 36, and Equation 37,

$$\sigma_z = -\frac{3P}{2\pi a^3}(a^2 - x^2 - y^2)^{1/2} \qquad \text{Equation 35}$$

$$\sigma_{zx} = -\frac{3\mu P}{2\pi a^3}(a^2 - x^2 - y^2)^{1/2} \qquad \text{Equation 36}$$

$$\sigma_{yz} = 0 \qquad \text{Equation 37}$$

σ is the Cauchy stress, a is the Hertzian contact circle radius, μ is the coefficient of friction, and P is the load acting between the surfaces. These conditions are for within the contact itself, where ($x^2 + y^2$) is less than or equal to a^2. A stress function in terms of displacements is applied to the governing equations to solve the stress fields. Equilibrium and the boundary conditions are satisfied automatically with solutions of the stress functions. The stress field is determined with these solutions and constitutive equations of elasticity. Stresses associated with the normal and tangential tractions are found separately. The total solution is the superposition of both stress fields.

Modeling the stresses that produce scratching from this contact requires computation of the maximum von Mises stress, and then comparing this to a yield criterion. With only normal tractions of a pure Hertzian contact, the maximum von Mises stress is below the surface of the material. Yet, the stress reaches a maximum at the wafer surface under the contact of the asperity when frictional tractions are sufficient

(Hamilton 1983, 53-59). The stress field directly under the contact and at the surface is given in Equation 38 through Equation 41, where z = 0 and $r = (x^2 + y^2)^{1/2}$ is less than or equal to a,

$$\sigma_x = \frac{3P}{2\pi a^3 r^2}\left[\frac{y^2 - x^2}{r^2}\left\{\frac{1-2\nu}{3}\left((a^2 - r^2)^{3/2} - a^3\right)\right\} - (x^2 + 2\nu y^2)(a^2 - r^2)^{1/2}\right] - \frac{3\mu P}{2\pi a^3}\left[\frac{\pi x}{2}\left(\frac{\nu}{4} + 1\right)\right] \quad \text{Equation 38}$$

$$\sigma_y = \frac{3P}{2\pi a^3 r^2}\left[\frac{x^2 - y^2}{r^2}\left\{\frac{1-2\nu}{3}\left((a^2 - r^2)^{3/2} - a^3\right)\right\} - (y^2 + 2\nu x^2)(a^2 - r^2)^{1/2}\right] - \frac{3\mu P}{2\pi a^3}\left[\frac{3\pi\nu x}{8}\right] \quad \text{Equation 39}$$

$$\sigma_{xy} = \frac{3\mu P}{2\pi a^3}\left[\frac{\pi y}{4}\left(\frac{\nu}{2} - 1\right)\right] \quad \text{Equation 40}$$

$$\sigma_{zx} = \frac{3\mu P}{2\pi a^3}\left[-(a^2 - r^2)^{1/2}\right] \quad \text{Equation 41}$$

ν is the Poisson's ratio of the wafer. σ_z and σ_{yz} have the same relations provided in Equation 35 and Equation 37, respectively.

For the stress field of the surface directly under the contact, yielding criteria is applied. The distortion-energy theory is taken for the failure criterion, which states that yielding occurs when the distortion strain energy per unit volume is greater than or equal to the distortion strain energy per unit volume at yield of that material in simple tension or compression (Budynas and Nisbett 2011, 1007). The result of this theory is the von

Mises stress criterion, which states that if the von Mises stress is greater or equal to the yield stress of the material, then that material plastically deforms. The wafer, this is equivalent to energy being dissipated in producing plastic deformation of a scratch. In three-dimensional Cartesian coordinates, the von Mises stress is defined in Equation 42,

$$\sigma_v = \frac{1}{\sqrt{2}}\left[\left(\sigma_x - \sigma_y\right)^2 + \left(\sigma_y - \sigma_z\right)^2 + (\sigma_z - \sigma_x)^2 + 6\left(\sigma_{xy}^2 + \sigma_{yz}^2 + \sigma_{zx}^2\right)\right]^{1/2} \qquad \text{Equation 42}$$

Hamilton states that the value of maximum von Mises stress moves to the surface of the material when the coefficient of friction is larger than 0.3. The location of this maximum von Mises stress is at x = -*a*, y = 0, and z = 0. Evaluating the value of von Mises stress at this location from Equation 35 through Equation 41 provides Equation 43,

$$\sigma_v = \frac{3P}{2\pi a^2}\left[\frac{(1-2\nu)^2}{3} + \frac{(1-2\nu)(2-\nu)\mu\pi}{4} + \frac{(16-4\nu+7\nu^2)\mu^2\pi^2}{64}\right]^{1/2} \qquad \text{Equation 43}$$

This equation provides the yield criterion for an elastic sliding pad asperity over the wafer surface. If the coefficient of friction between the pad asperity and wafer is above 0.3, then this relation is applicable. With this friction requirement combined with a von Mises stress above the yield stress of the wafer material, plastic deformation occurs on the wafer surface from softer material asperity tractions.

With this model, the softer pad asperity cannot scratch the wafer unless the coefficient of friction is greater than 0.3. The elastically deformed pad asperity cannot damage the wafer surface without the added tractions from friction since polishing pads

have lower hardness than wafer materials (Kim, Saka, and Chun 2014, P169-P178). With the maximum von Mises stress below the surface, the elastic asperity can only plastically yield the wafer if the asperity yield stress is greater than the wafer yield stress. This will not occur since copper and silicon dioxide have an average hardness that is an order of magnitude larger than IC1000 pad material. Hamilton shows that the maximum von Mises stress below the surface does not change significantly with added friction (Hamilton 1983, 53-59). Yet, the maximum von Mises stress on the surface is directly a result of the frictional tractions and its value surpasses the stress level under the surface when the coefficient of friction is greater than 0.3. This frictional criteria is what allows for the softer pad asperity to scratch the harder wafer.

Since the pad is a viscoelastic material, the stresses and strains of the CMP contact are time dependent. If a constant compressive displacement were applied to the sliding asperity, the normal load produced would decrease with time. This constant displacement boundary condition is similar to that of a stress relaxation experiment. In Section 4.1.1, it was experimentally shown that stress and load decreases over time for the IC1000 material which is common viscoelastic behavior. The von Mises stress on the wafer from a single asperity would thus decrease over time. As the pad asperity relaxes more, the stress level moves away from the failure conditions. In actual CMP, displacement is not held constant. Instead the normal pressure between the pad and the wafer is controlled and kept constant. This condition is analogous to a constant load if the single pad asperity is considered. With a constant load, the pad asperity will creep and displace into the wafer. The contact radius will increase and disperse the load over a larger area. As the contact radius increases, the von Mises stress decreases. For both

stress relaxation and creep conditions of a single viscoelastic asperity contact, the increase of time in contact decreases the von Mises stress and thus the ability for the pad asperity to scratch the wafer.

A real contact between a polishing pad and a wafer consists of many pad asperities in contact. The probability density of pad asperity heights has been experimentally shown to have an exponential distribution (Kim, Saka, and Chun 2014, P169-P178). With initial loading of a constant normal pressure, all pad asperities will have different levels of load acting on them depending on their initial height relative to the pad asperity mean height line. Taller asperities have a greater chance to damage the surface as the resulting load and thus von Mises stress is larger. As the asperities begin to creep under the applied load, the real area of contact increases to support the total load. Again, an increase of contact time results in a decrease in von Mises stress and ability for the pad to damage the wafer surface. Additionally, a decrease in the surface roughness of the pad surface reduces the number of asperities that have a larger load in contact, decreasing the von Mises stress away from failure.

Friction in this contact analysis is only quantified with the coefficient of friction, μ. The coefficient of friction is an empirical value that combines the multiple individual mechanisms which result in the observed frictional force. It is also an average value for the coefficient of friction through the entire contact. A particular pad asperity may have a larger equivalent value of μ than the majority of the asperities in contact. Based on this, the criterion that the coefficient of friction must be larger than 0.3 is challenging to implement for rough surface contact with multiple asperities. This yield criterion is underestimated through use of the coefficient of friction of the pad and wafer contact.

Adhesive forces between the pad asperity and wafer are not considered in this analysis. Adhesion models such as Johnson-Kendall-Roberts (JKR) and Derjaguin-Muller-Toporov (DMT) would be used to account for these surface forces (Johnson, Kendall, and Roberts 1971, 301-313; Derjaguin, Muller, and Toporov 1975, 131-143). Additional tractions would be included due to adhesive forces. It is currently unknown if the effects would be significant and should be investigated in future work. Plastic deformation of the pad asperity is not considered in this stress field analysis. The uniform contact pressure distribution of a plastically deformed asperity has been shown in the literature to yield the wafer surface with less frictional tractions (Kim, Saka, and Chun 2014, P169-P178). Plastic deformations should be accounted for to accurately model the yielding of the wafer surface.

4.3 Chemical-Mechanical Planarization Experimental Results

Chemical-Mechanical Planarization was experimentally modeled using a reciprocating linear tribometer. IC1000 polishing pad material was loaded in compressive contact with copper and silicon dioxide wafer materials. The wafer materials were reciprocated at velocity. The normal pressure and velocities were set to envelope a range of magnitudes that are commonly used in CMP. A typical CMP slurry is used as the lubricant during these experiments. There are certain aspects of the planarization experiments that are dissimilar to the actual CMP processes. These differences are considered in the analysis and are discussed here.

Since the linear tribometer provides a contact that is dissimilar to that of actual CMP, certain aspects of these experiments do not encompass what occurs in the actual planarization process. In manufacturing, the pad and wafer are rotated against each other to provide even material removal across the entire wafer. The linear tribometer only moves the pad and wafer contact back and forth in two directions. The resulting wear patterns with planarization will be directional, as opposed to the multidirectional rotating CMP process. Also, the same wafer surface is used for the entirety of the experiments for an equivalent 250 wafers. Wear and damage results of the wafer and pad are expected to be more severe as features are repeatedly worn.

Slurry is constantly flowing in CMP so that the used slurry is either drained or filtered to remove wear particles or agglomerated slurry particles. Removal of large particles from the slurry helps prevent damage from occurring with two-body and three-body abrasions. In the tribometer experiments of this work, the slurry is not removed and replaced during an experiment. The water in the slurry actually evaporates, so more slurry is added periodically to keep a wet contact. From adding additional slurry and from the creation of wear particles, there is a greater chance for damage to occur on the wafer than in actual CMP. Again, it is expected that there is a larger amount of damage to occur in the conducted planarization experiments than in actual CMP processes.

Diamond conditioners are used to roughen up the pad surface in CMP. This is performed either during or in between the polishing of wafers. The literature states that when a pad surface is not conditioned through CMP, the surface loses roughness from plastic deformation of the surface asperities (Steigerwald, Murarka, and Gutmann 1997; Li et al. 1995, 601-606; Prasad et al. 2011, H394-H400). No conditioning of the pad is

performed during the planarization experiments, which creates a new pad surface from the bulk that was underlying the old surface. From this, the pad surface is expected to be more worn and damaged than in actual CMP, which is desired in this work. A more worn pad surface allows for easier observation of the processes of damage that occur in CMP.

4.3.1 Planarization Experimental Results

For characterization of the mechanical contact between the polishing pad and wafer materials, planarization experiments are performed with a linear reciprocating tribometer. A total of eight experimental trials are conducted to envelope a wide range of velocity and normal pressure that occur in CMP. Copper and silicon dioxide are used as the wafer materials that reciprocate against the IC1000 pad sample. The magnitudes of average linear velocity are set at a maximum 23.62 in/s and the minimum is set at 7.87 in/s by the motor controller. From timing of the motor moving through the set distance, the total error associated with the maximum and minimum velocities are 23.62 ± 1.49 in/s and 7.87 ± 0.16 in/s, respectively.

The magnitude of high pressure is set to be 5 psi, and low pressure is set to be 2 psi. Normal force is set with the magnitude of pressurized air into a pneumatic cylinder that pushes the pad material on to the reciprocating wafer plates. The tribometer pneumatic system was designed to apply higher loads than those applied with these experiments. With values of normal force used in these experiments between 1.5 lb_f and 15 lb_f, the applied loads tend to relax slightly over time. As a result, the load had to be

periodically adjusted during the experiments in an attempt to maintain the desired pressure of the experiment. The average pressures through all experiments are provided in Table 17 along with the values of standard deviation. Values of pressure are based on the output voltages of the tribometer dynamometer that are converted to load using the factory calibration. The nominal pressure is then computed with the pad sample's nominal area. The average normal pressure that most deviates from the desired value is the low pressure, high velocity, silicon dioxide experiment. The average pressure of 2.50 psi is significantly larger than the desired 2 psi of pressure. The results of this experiment should be analyzed with the knowledge that the pressure is larger than the other low pressure experiments. The remaining experiments have pressures closer to the desired 2 psi or 5 psi with similar magnitudes of standard deviation.

Table 17: Average and Standard Deviation of Normal Pressure for Planarization Experiments

Wafer Material	Pressure	Velocity	Average Normal Pressure (psi)	Standard Deviation of Normal Pressure (psi)
Copper	Low	Low	2.17	0.20
Copper	High	Low	5.08	0.17
Copper	Low	High	1.97	0.29
Copper	High	High	4.84	0.28
Silicon Dioxide	Low	Low	1.79	0.23
Silicon Dioxide	High	Low	5.09	0.36
Silicon Dioxide	Low	High	2.50	0.78
Silicon Dioxide	High	High	4.98	0.21

A sample of pad material is collected at equivalent distances traveled of 10, 50, 100, and the total of 250 wafers polished. The set distances traveled for low and high velocity trials are 3,517 feet and 10,548 feet, respectively. These distances are analogous

to the time that a point on the pad surface travels in contact during CMP. This pad travel time is desired to be held constant for each experiment. For a total of 250 wafers, the total travel time is 89.3 minutes. This time is based on the geometry of CMP and the polish time of 60 seconds per wafer, as discussed in Section 3.3.1.1. Time traveled of the pad material is not the product of 250 wafers and 60 seconds per wafer since a point on the pad not always in contact with the wafer.

Errors in the time traveled that is associated with each of the four collected pad samples in each experiment are given in Table 18. This time is analogous to the error in distance traveled, as both parameters are computed based on the number of cycles that the tribometer has completed. From Table 18, a significant error in travel time exists in the high pressure and low velocity copper experiment at 250 wafer, which has traveled 8.53% longer than it should have. The most significant error in time traveled is from 50 wafers to 250 wafers for the low pressure and high velocity copper experiment. These samples traveled less time and distance than they should have. These errors in distance and time traveled should be accounted for during analysis of the results.

Table 18: Error in Time Traveled for Pad Samples

			Time Traveled Error (%)			
Wafer Material	Pressure	Velocity	10 Wafers	50 Wafers	100 Wafers	250 Wafers
Copper	Low	Low	-0.47	-0.38	-0.19	-0.08
Copper	High	Low	0	0	0	8.53
Copper	Low	High	0	-25.95	-12.97	-5.19
Copper	High	High	0	0	-0.03	-0.02
Silicon Dioxide	Low	Low	0	0	0	0
Silicon Dioxide	High	Low	0	0	0	0
Silicon Dioxide	Low	High	0	0	-0.02	-0.01
Silicon Dioxide	High	High	0	0	0	-0.01

4.3.1.1 Forces of Contact

Forces that act between the pad sample and wafer are continually measured with the dynamometer. These forces are measured parallel to the direction of travel, perpendicular to the direction of travel, and normally between the material contacts. These directions are represented by x, y, and z, respectively. The desired parameter to obtain from these results is the coefficient of friction, μ. The frictional force acts in the x-direction, which is also the direction of motion. This coefficient of friction is the ratio of frictional force to the normal force. Observation of how this parameter changes with normal pressure, velocity, and time traveled provides useful information about the stress fields in the pad and wafer during CMP. All force data is reduced down to an average value for one cycle. Variations in the data per cycle are smoothed with a uniform moving average filter with a window size of nine cycles. This smoothing allows for easier observation of trends in the data over time. It needs to be justified that any trends in the coefficient of friction with time are not due to changing magnitudes of normal force. To justify this, the forces in the x and z-direction are plotted versus time for copper and silicon dioxide wafers in Figure 50 and Figure 51, respectively.

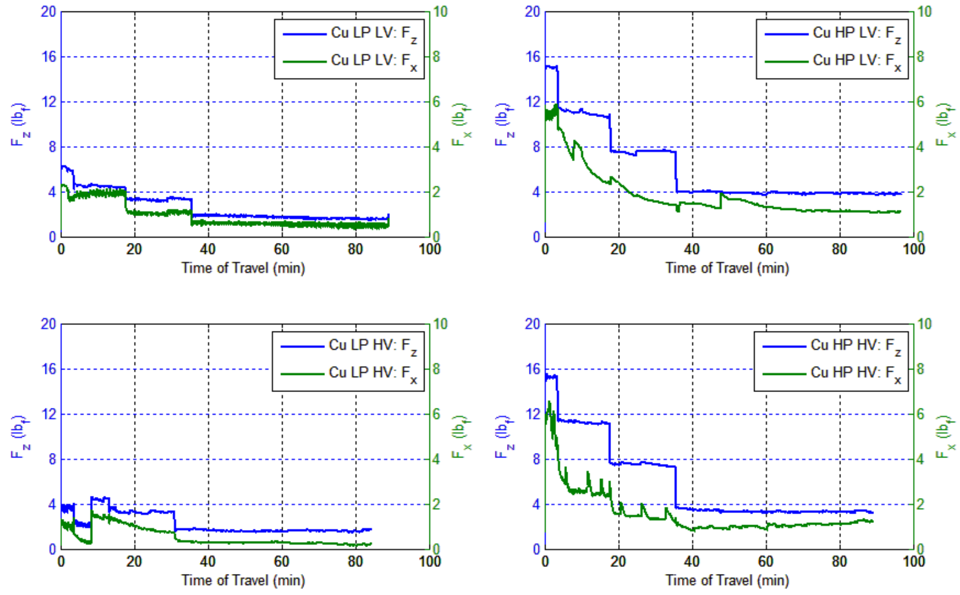

Figure 50: F_z and F_x with Travel Time for Copper Wafer and Pad Planarization Experiments

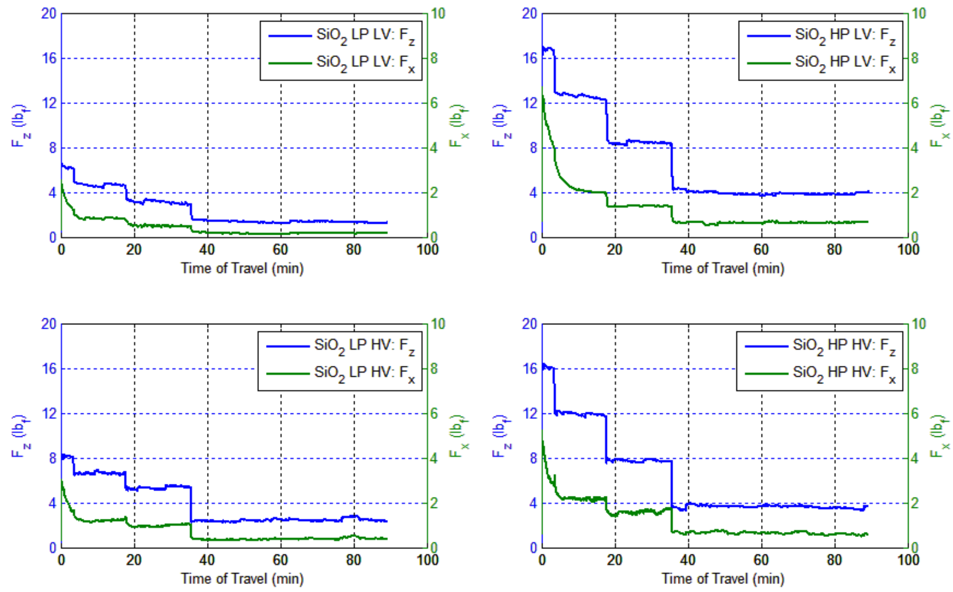

Figure 51: F_z and F_x with Travel Time for Silicon Dioxide Wafer and Pad Planarization Experiments

Figure 50 and Figure 51 illustrate the normal and frictional forces that act on the pad and wafer material through the entire equivalent 250 wafers polished. The periodic decrease in the set normal force is a result of maintaining the normal pressure as pad material is removed. Smaller increases of F_z between the larger increases of F_z occasional adjustments to maintain the pressure, as the normal force has a tendency to drift to lower values. The frictional force appears to change along with the normal force, whether they are larger jumps or smaller adjustments in F_z. There is extra variation in the frictional force that is not a result of the changes in normal force, which corresponds to changes in coefficient of friction. There are a few instances that are illustrated in Figure 50 where a small increase in the normal force from manual adjustment results in a relatively large increase in frictional force. These instances are seen within the two high pressure copper experiments, which are further elaborated on when analyzing coefficient of friction results.

Coefficient of friction is plotted versus time traveled for all copper wafer experiments in Figure 52, and for all silicon dioxide wafer experiments in Figure 53. Also plotted in these figures are the average roughness of pad sample surfaces with error bars representing plus and minus one standard deviation about the mean.

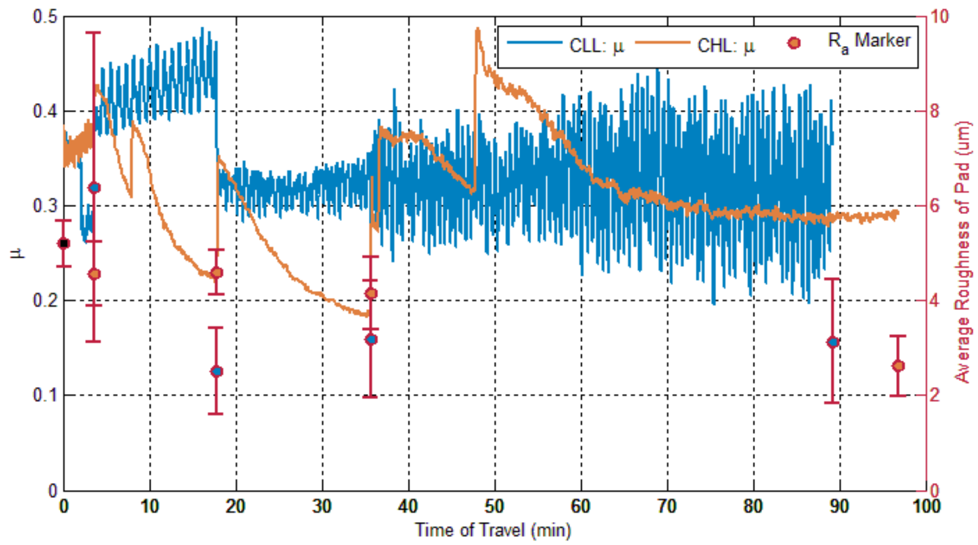

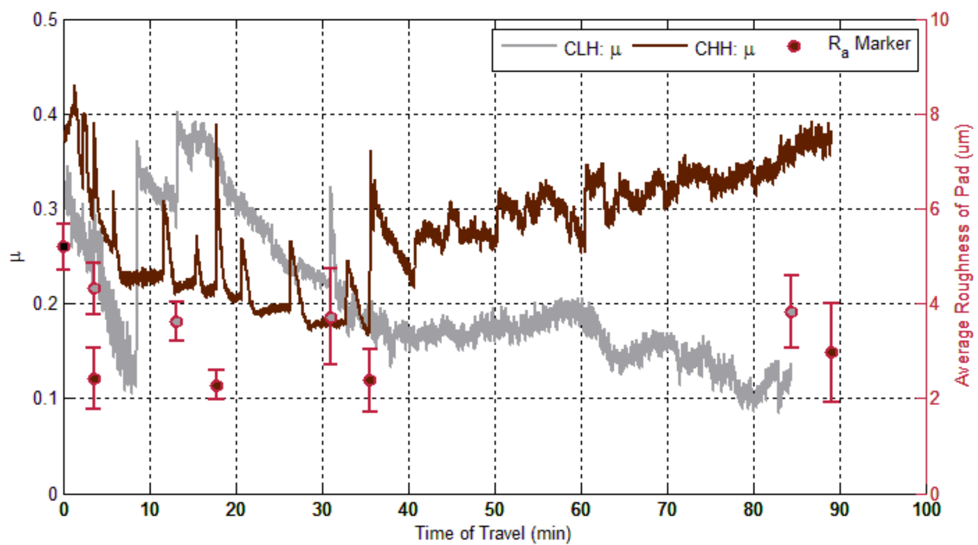

Figure 52: Coefficient of Friction and Average Pad Roughness with Time Traveled for Pad on Copper Wafer Experiments. Top: CLL (Copper, Low Pressure, Low Velocity), CHL (Copper, High Pressure, Low Velocity). Bottom: CLH (Copper, Low Pressure, High Velocity), CHH (Copper, High Pressure, High Velocity).

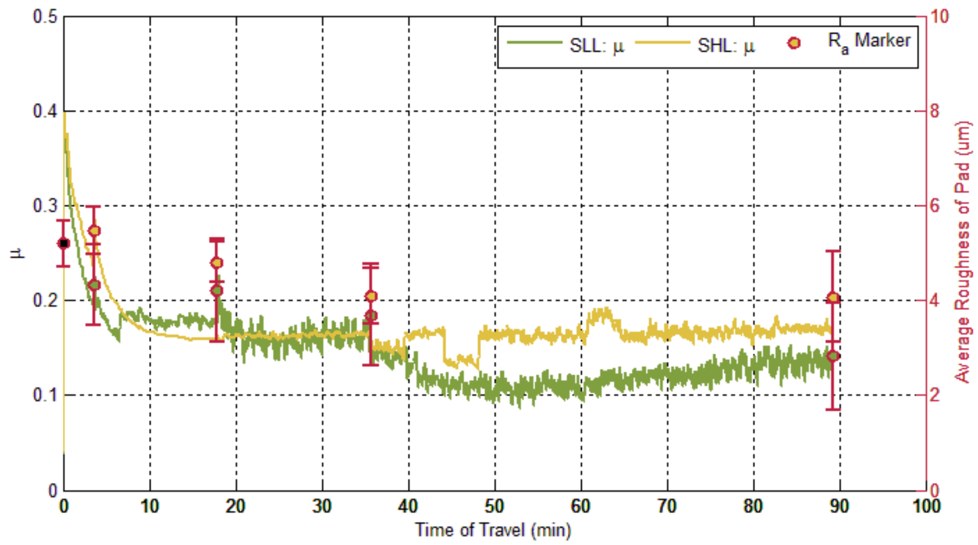

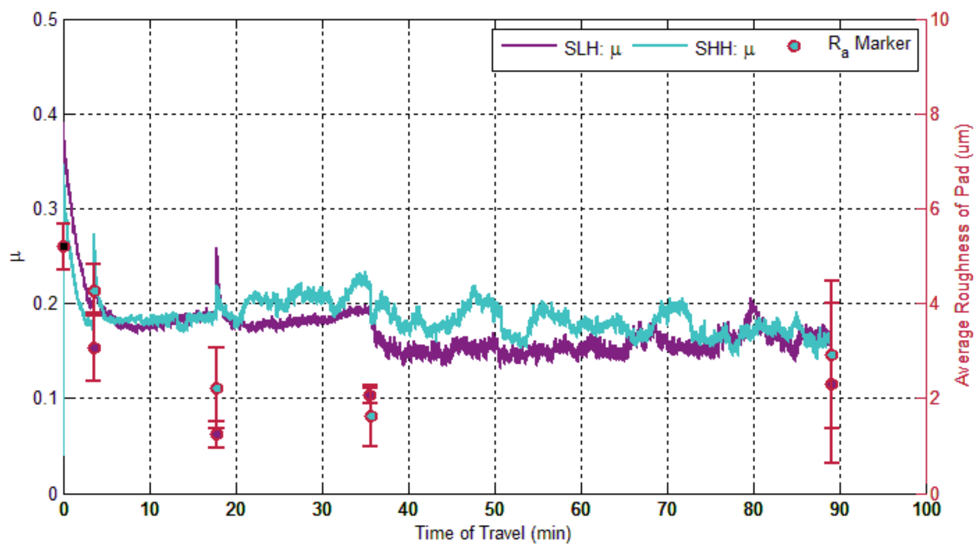

Figure 53: Coefficient of Friction and Average Pad Roughness with Time Traveled for Pad on Silicon Dioxide Wafer Experiments. Top: SLL (SiO_2, Low Pressure, Low Velocity), SHL (SiO_2, High Pressure, Low Velocity). Bottom: SLH (SiO_2, Low Pressure, High Velocity), SHH (SiO_2, High Pressure, High Velocity).

In all eight experiments performed, especially the experiments with copper wafers, there are significant increases in the coefficient of friction that occur in a very short period of time. Some of these sudden increases are a result of the removal and reapplication of load between the pad and wafer. This occurred every time a pad sample was collected and can be seen as the periodic decreases in F_z in Figure 50 and Figure 51. In Figure 52 and Figure 53, the times that the pad material was sampled are represented by the roughness markers. Another reason for these sudden increases in coefficient of friction is the periodic adjustment of normal pressure as the normal force tends to drift over time in this experimental setup. A small increase in the normal force corresponds to larger increases in the frictional force. This behavior is most prevalent in both high pressure copper planarization experiments. Even though the normal pressure is adjusted periodically, it is still kept near to the desired value as quantified previously in Table 17. After the large increase in the coefficients of friction, for most trials the values tend to move toward that which occurred just before the increase. This is not the case for some of the copper wafer experimental trials.

Coefficients of friction of the copper wafer trials provide the most variation of trends over time. The experiment with low pressure and low velocity begins with a sharp decrease in coefficient of friction, to a sudden and then steady increase for the first 18 minutes of travel time. For the remainder of the experiment, the coefficient of friction is maintained at approximately 0.32 with a large amount of variation about this center. The variation is found to be largely a result of the frictional force from referencing Figure 50. At a higher pressure with low velocity, the coefficient of friction tends to decrease over time after a sudden increases, viewing the top of Figure 52.

Copper trials with high velocities have the same general decreasing behavior in coefficient of friction over time. The coefficient of friction values are generally less than the low velocity copper experiments. The most interesting feature is that high pressure and high velocity trial in Figure 52 begins to steadily increase its coefficient of friction from about 40 minutes of travel time until the experiment is ended.

All silicon dioxide planarization trials show similar behavior and magnitudes of coefficient friction in Figure 53. The coefficients of friction begin from between 0.3 to 0.4 and quickly decrease to below 0.2 within 10 minutes of travel time. After 10 minutes, the coefficient of friction level stays steady relative to the copper trials. There still is some fluctuation in the values, especially for the high velocity experiments.

Decreasing trends of friction coefficient with time polished explains that scratch prevention is aided through conditioning the surface of the pad. As the coefficient of friction between the pad and wafer, lower stresses are imparted on the materials. From the contact stress analysis in Section 4.2, lower coefficients of friction move the maximum von Mises stress below the surface of the wafer. The wafer will not be plastically ploughed by an elastically deformed pad asperity if the coefficient of friction is below 0.3, since the wafer surface will not be yielded by a softer pad material with the maximum von Mises stress below the surface. This statement neglects the potential effects that surface adhesion and pad plasticity have on the contact stress field.

A description of how the pad surface is evolving through the polishing process is provided by measurement of surface roughness. Average surface roughness of the collected IC1000 pad samples are plotted along with coefficients of friction on Figure 52 and Figure 53. A marker that represents the new pad surface roughness is provided

at time zero for reference on all graphs. The circular marker represents the average value of roughness for that pad sample. Error bars represent plus and minus one standard deviation of the measurements for one collected sample about the average. All experiments show a general decreasing trend in surface roughness with time of travel. Most trials show a sharp decrease in average roughness for the first 18 minutes of travel time. After this initial decrease, the average roughness levels off. Coefficient of friction shows a similar behavior in most experiments. This behavior suggests that the surface roughness of the pad has a positive correlation with coefficient of friction between the wafer and pad material. Coefficient of friction is not only a function of pad surface roughness as the data shows. This correlation is in agreement with the literature that states yielding of the wafer surface is reduced with decreasing pad roughness (Kim, Saka, and Chun 2014, 431-442). The high pressure and high velocity copper trial had an increase in the coefficient of friction through the second half of its experiment, where roughness did not increase. Other variables besides pad surface roughness that were unmonitored in these experiments caused this increase.

Graphs of coefficient of friction versus distance traveled are shown in Figure 54 to determine if the values have different observed trends with distance. The magnitudes of coefficient of friction between 1000 feet and 4000 feet of distance traveled for copper and the pad appear to match better. At these distances, the friction coefficients are at their largest, except for the high pressure and high velocity. For silicon dioxide and the pad, the initial drop in coefficient of friction appears to be more uniform with distance versus time traveled. All trials appear to reach the steady value after approximately 750 feet traveled.

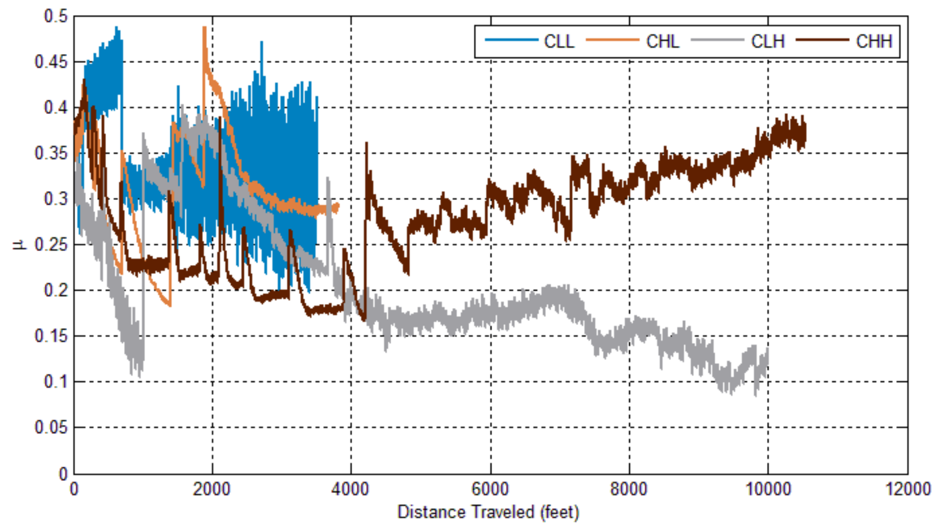

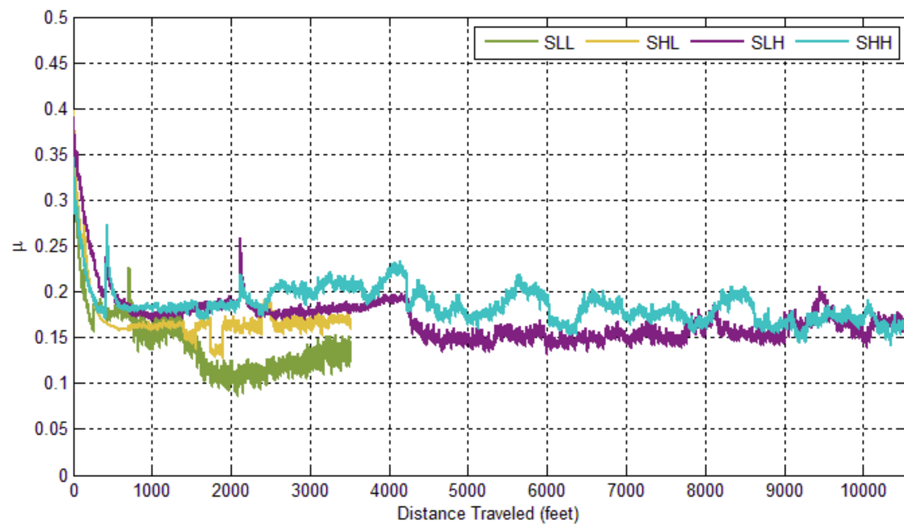

Figure 54: Coefficient of Friction versus Distance Traveled. Top: Copper and Pad Wafer Trials.

Bottom: Silicon Dioxide and Pad Wafer Trials.

4.3.1.2 Topographical CMP Surface Evolution

More detailed observations are conducted on CMP surface changes through visual analysis and profilometry. Both pad and wafer materials show visual evidence of wear and plastic deformation. All copper surfaces after planarization show wear tracks from the pad surface squares. A photograph of the copper plate surface from the high pressure and high velocity experiment is given in Figure 55, where the wear tracks are clearly seen. If the copper surface is held in the light to reflect in the proper direction, a dozen or more scratches are seen along the length of a single track. In Figure 55, a slightly brighter portion in the middle of the plate and across two tracks is visible. This section of the surface is from the original surface of the wafer as it has not completely worn away. It is more prominent for lower pressure and lower velocity experiments. This surface feature is a result of reciprocation of the contact, since the frictional force is larger when the contact begins and slows to rest, as seen from frictional force data in Figure 56 for two cycles. This figure has a motor signal, where high represents when the table is in motion. In the middle of the wafer contact with the plate, friction is close to zero. Less frictional force provides less wear and thus leaving some of the original surface of the wafer plates. In all other analysis of surface forces, the average of the forces in a cycle are used. Observation of the silicon dioxide surfaces after planarization show noticeably deeper scratches than in copper when viewing the surface. The depth magnitude of these wear features are quantified with profilometry measurements.

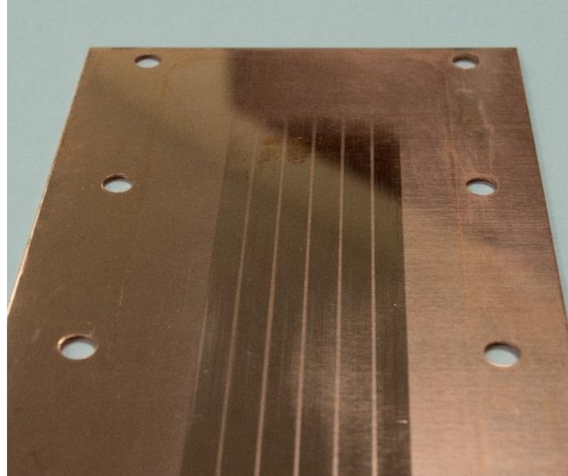

Figure 55: Copper Plate with Wear Tracks after High Pressure and High Velocity Planarization

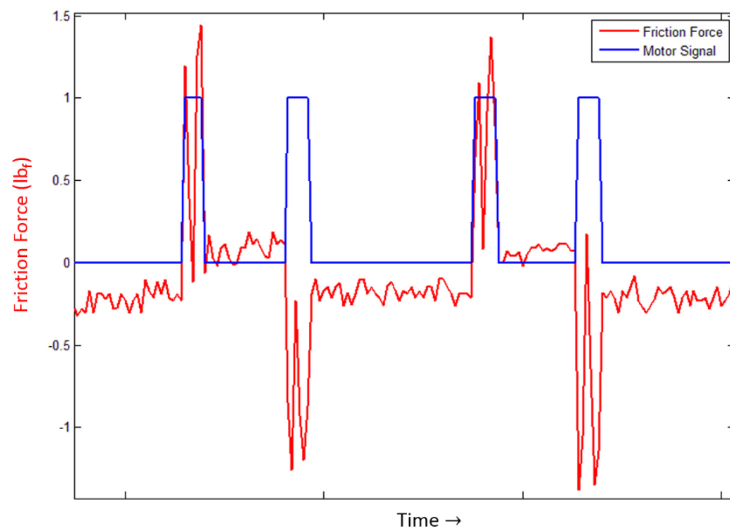

Figure 56: Friction Force of a Planarization Experiment through Two Complete Cycles

Pad surfaces visually show the same general features as a function of pressure, velocity, distance traveled, and wafer material. An image of representative pad sample surfaces is provided in Figure 57. Pad samples that were used to polish copper had a green color on the surface that is more intense with greater velocity, pressure, and

distance traveled. The sample which has the most intense color is pictured in the middle of Figure 57. This green color is likely a result of chemical reactions with copper particles in the slurry, which appear to be similar to a copper patina. Pad material used to polish silicon dioxide show no change in color. Yet, the wear surfaces of many pad samples have a more reflective or shiny appearance in some locations. These features can be identified as the bright parts of the sample surfaces of the two worn pad samples in Figure 57. From topography measurements of these reflective parts of the pad surface, they correspond to a smoother surface. This is expected as a smoother surface can reflect light better in a single direction with less light scatter than a rough surface. The appearance of these reflective pad surfaces increased with pressure, velocity, and distance traveled. This information provides evidence that the pad surface is plastically deforming through the CMP process. Glazing of the pad is the term for this type of plastic deformation and smoothing of the pad surface (Steigerwald, Murarka, and Gutmann 1997; Li et al. 1995, 601-606; Prasad et al. 2011, H394-H400). This glazing has been shown to reduce material removal rate in the literature, and correlates with lower coefficients of friction between the pad and wafer. Plastic deformation of the pad surface is thus an important aspect of strain energy dissipation that must be considered in the thermomechanical model of CMP.

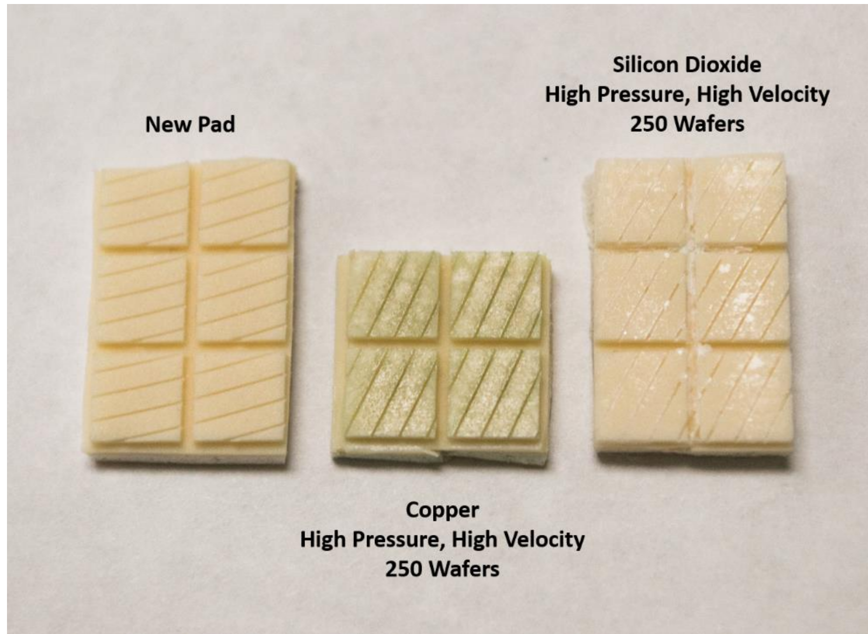

Figure 57: Pad Sample Surfaces from Planarization Experiments

To quantify these topographical changes of CMP surfaces, profilometry of pad and wafer samples is conducted before and after planarization experiments. Measurements on pad material surfaces are taken for the four collected samples of polishing 10, 50, 100, and 250 of equivalent wafer count. These measurements are performed for all eight experiments, along with new pad samples. Measurement of surface topography for all pad samples is conducted along the length of the small grooves in the pad surface squares. Each pad sample is measured at least five times with the profilometer across different sections of the pad. An average of measurements is taken for the representative roughness of each sample. Bar graphs of average roughness and root mean squared roughness are presented in Figure 58 and Figure 59. The x-axis labels represent the planarization experiment from which the samples are taken. The first letter represents the wafer material of copper or silicon dioxide, by ‘C’ and ‘S’,

respectively. The second letter represents the value of pressure that is low or high, by "L" and "H", respectively. The third letter represents the velocity being either low or high as well. Error bars represent the standard deviation of measurements above and below the average.

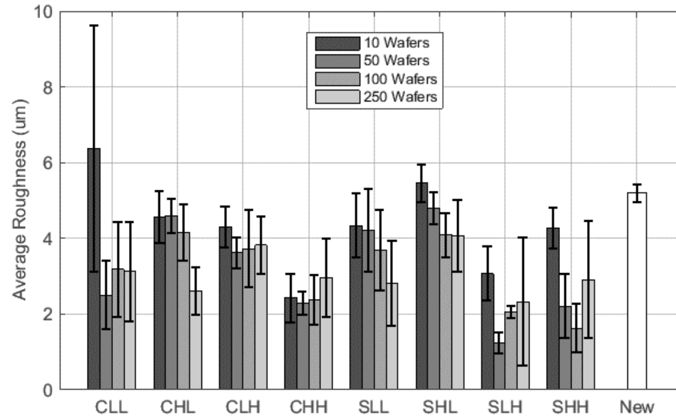

Figure 58: Average Surface Roughness of Pad Samples

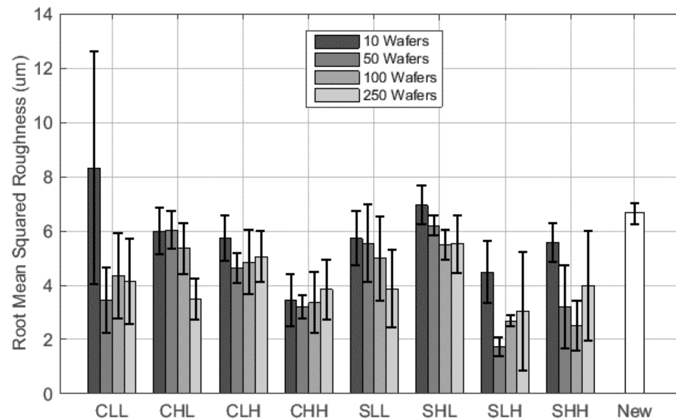

Figure 59: Root Mean Squared Roughness of Pad Samples

Both average roughness and root mean squared roughness have very similar trends with each experiment and wafer count, from comparing results in Figure 58 and

Figure 59. Roughness measurements show a general decreasing trend with more time polished and distance traveled. The roughness data appears to show that the pad asperities are plastically deformed due to the CMP process. It is also apparent that as a more energy is input to the pad through longer distances and higher velocities, the surface is worn more. Higher pressures do not appear to smooth the surface more than the low pressure pad samples. Pad samples polished with lower velocities appear to reach smaller roughness values more slowly from the new pad through 250 wafers. Higher velocity experiments reach the lowest roughness magnitudes more quickly and then begin the increase slightly after about 50 or 100 wafers polished. These decreasing trends of roughness are a result of the high velocity samples traveling a longer distance than the low velocity, though they travel for the same amount of time. Longer distance traveled with the sample applied pressure results in more energy input to the system to plastically deform the surface asperities. The high velocity pad samples show a sharp initial decrease in roughness and then a gradual increase with longer distances traveled. It is unsure how much of a contribution that wear of the pad material has on the roughness values since the mass of all samples increases due to take up of slurry particles and wear particles. Wear of the surface may also contribute to changing measurements in surface roughness through planarization.

For each experiment, the surface topography of the wafer is measured before and after the experiment is completed. Measurements are performed along the length of the wafer plates, which is in the direction of pad travel. Topography measurements are also captured perpendicular to the direction of pad travel, which is along the width of the wafer plates. Every width and length measurement before and after is measured at

least five times to characterize the entire wafer plate. Reported values are an average of the multiple measurements captured. Plots of average roughness and root mean squared roughness of the wafer materials are shown in Figure 60 and Figure 61.

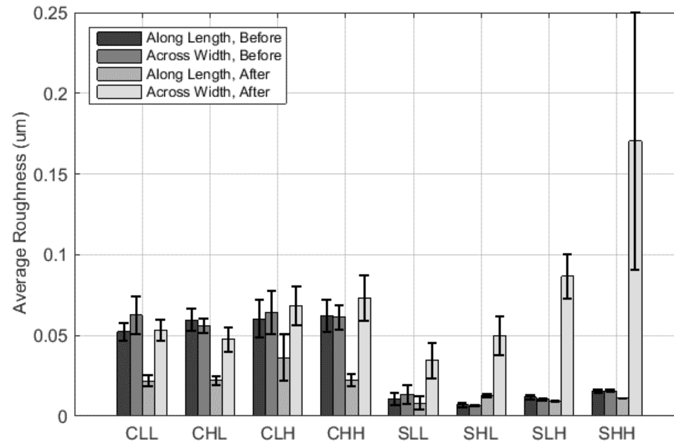

Figure 60: Wafer Surface Average Roughness from Before and After Planarization

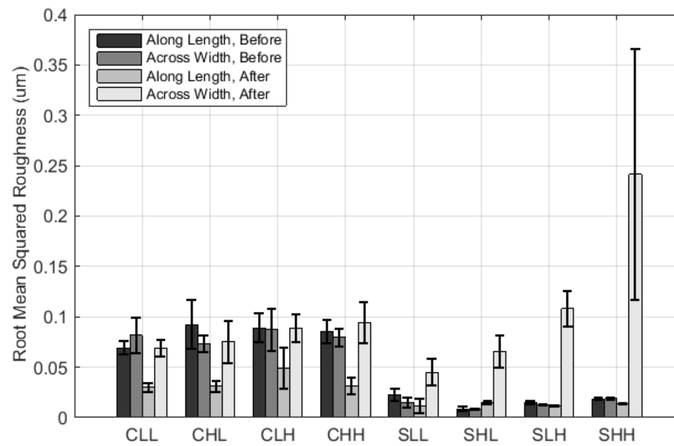

Figure 61: Wafer Surface Root Mean Squared Roughness from Before and After Planarization

Figure 61 and Figure 62 display that the average and root mean square roughness have similar trends between each experiment and direction measured. Roughness measurements along the length and across the width of the wafer plates before planarization are relatively similar, representing an isotropic surface topography. After planarization, the roughness in the direction of wear becomes smaller except for silicon dioxide at high pressure and low velocity. Perpendicular to the direction of wear, the roughness of copper remains relatively close in magnitude from before and after. The largest change in roughness is seen perpendicular to the wear direction for the silicon dioxide wafer surface. For the high pressure and high velocity silicon dioxide surface, the average roughness perpendicular to the sliding direction is ten times larger in magnitude than before polishing. The roughness values increase with higher pressure, but more so with higher velocity or distance traveled.

This general trend of decreasing roughness along the direction of travel is a result of the continual wear of the pad and slurry particles on the wafer along the same direction. The wafer surface asperities are planarized more with each pass providing a smoother surface. Increase in roughness perpendicular to the direction of travel is a result of the wear tracks and grooves that are continually worn deeper with each pass. Measurements of topography along the width of the wafer plates pick up the variation in these grooves. The average roughness data in Figure 60 suggests that the wear grooves produced in silicon dioxide are deeper than in copper. This does not necessarily mean that more material is worn away with silicon dioxide as roughness is a small scale measurement of topography. Roughness characterizes the small scale topography that has a wavelength less than the cutoff length of 0.8 mm. Figure 62 presents the larger

scale topography measure of average waviness. Waviness can be used to estimate the amount of material worn by measuring the depth of wear tracks on the wafer surface.

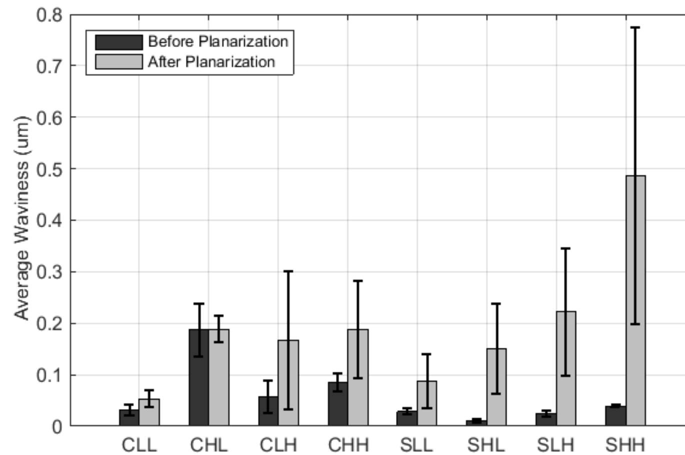

Figure 62: Average Waviness of Wafer Surfaces Perpendicular to Direction of Travel

Average waviness of all wafer materials perpendicular to the direction of travel increases after planarization. Compared to the other experiments, the high pressure and low velocity copper average waviness did not increase significantly. It appears that this may be because it started out wavier than the other wafer plate surfaces. Aside from this anomaly, the average waviness of the wafer surfaces increases with distance traveled or higher velocity, and higher pressure.

The travel length of the profilometer probe is 5.6 mm, or 0.22 inches, per trial. The width of one square of the IC1000 pad material surface, seen in Figure 11, is also approximately 0.22 inches. Each measurement of topography across the width of the wafer was set to begin inside of a wear track. Thus, the profilometer measures the change in height of the wafer surface from within the wear track to outside of the wear

track where the pad surface never contacts. Roughness measurements do not reflect this wear track depth change since the cutoff length is 0.8 mm, or 0.03 inches. Waviness does capture this change in wear track depth, as visualized in Figure 63. This waviness profile depicts a peak which represents the portion of the wafer surface that is under the grooves of the pad material, so that it is not directly worn.

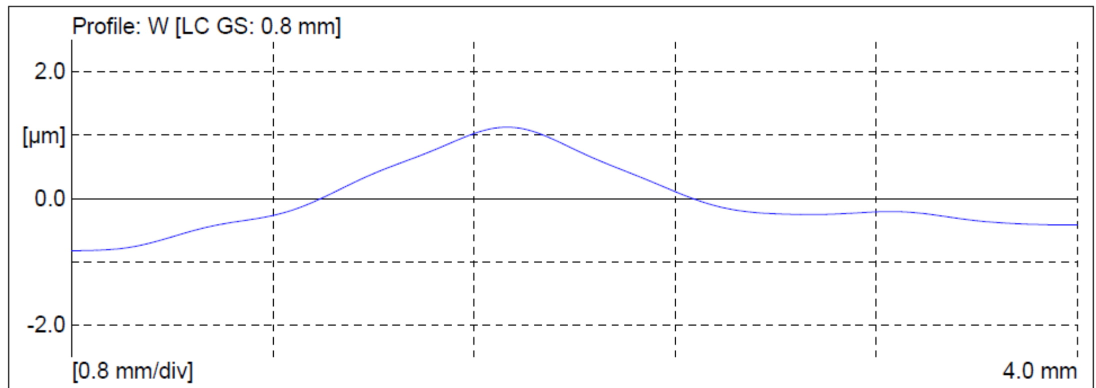

Figure 63: Waviness Profile Perpendicular to Travel Direction from Silicon Dioxide at Low Pressure and High Velocity (SLH), After Planarization

4.3.1.3 Energy of Material Removal

During planarization, the wafer material is worn away from the applied tractions between the wafer and polishing pad. For the thermomechanical model described in Section 3.1, the energy which wears this material is represented as a flux of mass out of the system. From the eight planarization experiments, change in mass of the wafer plates is tracked from weight measurements. The mass loss of the wafer material from each experiment is given in Table 19. Mass is only given in increments of 10 mg as this is

the resolution the scale provided with its setting. The experiment with low velocity and pressure on copper most likely lost some positive level of mass below 5 mg that the scale did not register. It is desired to quantify the energy which went into wearing this material away to account for energy fluxes of CMP.

Table 19: Wafer Mass Loss from Planarization Experiments

Wafer Material	Pressure	Velocity	Mass Loss (mg)
Copper	Low	Low	0
Copper	High	Low	20
Copper	Low	High	20
Copper	High	High	30
Silicon Dioxide	Low	Low	10
Silicon Dioxide	High	Low	10
Silicon Dioxide	Low	High	10
Silicon Dioxide	High	High	20

To approximate the energy that went into removing mass from the wafer, a simple geometrical model of the wafer wear is combined with the material surface energy, γ. Two times the surface energy of a material is equivalent to the energy required to create two areas of the material from breaking atomic bonds. Thus, it is the energy that is transferred into removing the material mass from the system. This quantity does not account for plastic strain energy which may also occur during the wear process that creates new surface area. The wafer surface energy can be applied to approximate the energy put into wearing the material if the total area worn can be estimated.

Assume a plate of material is in contact with another material. After the material has passed over the plate once, it has removed a volume of material that is a rectangular

area A through a depth d. This simplified wear geometry is shown in Figure 64. In reality, if a volume of material were removed, it would most likely not be evenly removed along the entire area of contact. If an equivalent volume were removed, then less of a real top surface area, A_r, would be produced with a larger real depth, d_r. The actual area that is created is smaller than the nominal worn track. This assumption is neglecting the area of the sides, which are assumed to be small relative to the top facing area. The depth of wear is approximately six orders of magnitude smaller than the wear track, comparing roughness measurements to the wafer plate measurements.

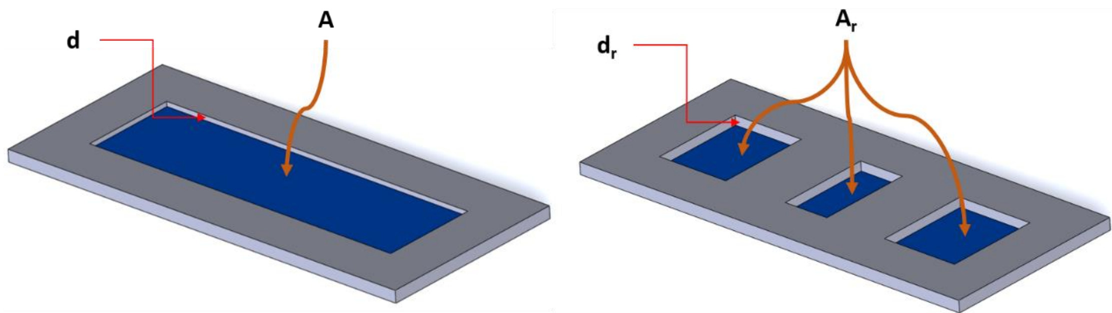

Figure 64: Wear Track Geometry for Material Removal Analysis

If the volume of material worn occurs over multiple passes, the value of A_r and d_r can change with each pass. The total material surface area created from each pass is approximated by the number of passes multiplied by the average real area. With the simple relation that the volume is equal to the area times the depth and a measurement of the final average d_r, an average value of A_r can be estimated. The volume of worn material as a function of area and depth is given in Equation 44,

$$ \forall = A_r d_r \qquad \text{Equation 44} $$

A_r can be put in terms of physically attainable values, in Equation 45,

$$ A_r = \frac{\forall}{d_r} = \frac{\Delta m / \rho}{\Delta W_a} \qquad \text{Equation 45} $$

Δm is the mass lost, ρ is the worn material density, and ΔW_a is the change in average waviness from before to after wear. From Equation 45, the average area that is created on the surface through each pass is equal to the volume of material lost divided by the average final depth. The mass lost divided by the density gives the volume of material worn. Density of copper and silicon dioxide are given in Table 2 also as 8.94 g/cm^3 and 2.20 g/cm^3, respectively. The change in average waviness perpendicular to the direction of travel provides an estimate for the average actual depth of the wear tracks created. Profilometry measurements capture the depth properly since the pad grooves provide a section of the pad where no wear due to direct pad contact occurs. The profilometry tip travels across these groove sections into the wear track to capture the change in surface height. The average waviness data is given in Table 20 for the eight run experiments.

Table 20: Average Waviness Perpendicular to Pad Travel of Wafer Surfaces

			W_a (um)		
Wafer Material	**Pressure**	**Velocity**	**Before Wear**	**After Wear**	**Difference**
Copper	Low	Low	0.0320	0.0533	0.0214
Copper	High	Low	0.1870	0.1881	0.0011
Copper	Low	High	0.0570	0.1674	0.1105
Copper	High	High	0.0857	0.1883	0.1026
Silicon Dioxide	Low	Low	0.0282	0.0868	0.0587
Silicon Dioxide	High	Low	0.0113	0.1503	0.1390
Silicon Dioxide	Low	High	0.0241	0.2217	0.1976
Silicon Dioxide	High	High	0.0394	0.4869	0.4474

From this analysis, the energy that is put into wearing away the wafer material is the product of two times the surface energy with the average real worn area and the number of passes that the pad has moved over the wafer through the experiment. This energy is mathematically described in Equation 46,

$$E_w = \frac{2\gamma N \Delta m}{\Delta W_a \rho} \qquad \text{Equation 46}$$

N is the number of passes of a planarization experiment. The maximum values of N depends on the experiment and ranges from 10,540 to 31,642 passes. Surface energy values for copper and silicon dioxide are given in Table 2 as 1.360 J/m^2 and 4.275 J/m^2, respectively. Mass loss values are taken from Table 19, while change in average waviness values are taken from Table 20. The complete range of energy values for all eight experiments are calculated and given in Table 21. Computed values of the frictional work are tabulated as well. This is the energy put into the pad and wafer through frictional forces as the tribometer friction force per cycle multiplied by the distance traveled per cycle.

Table 21: Energy of Material Removal from Planarization

Wafer Material	Pressure	Velocity	N_{max}	Total Frictional Work (kJ)	E_w (kJ)
Copper	Low	Low	10540	4.39	0
Copper	High	Low	11448	9.51	63.3
Copper	Low	High	30002	7.03	1.5
Copper	High	High	31638	22.65	2.8
Silicon Dioxide	Low	Low	10548	1.90	7.0
Silicon Dioxide	High	Low	10548	5.77	2.9
Silicon Dioxide	Low	High	31642	10.09	6.2
Silicon Dioxide	High	High	31640	17.15	5.5

Energy values for low pressure and low velocity copper are zero because the scale did not register any change in mass within its set resolution. No apparent trends are shown in the estimated material removal energy with pressure, velocity, or wafer material. Copper at high pressure and low velocity has the highest value due to its relatively small change in waviness. The plate began with an average waviness relatively close to the magnitude that all other copper plates ended with. For this analysis to be accurate, the surfaces have to begin very smooth. Otherwise, the added wear depth is not properly recognized as individual from the original waviness.

Assumptions made in this material removal energy analysis is that the average real worn area does not include any area of the wear track sides. These side areas are small relative to the real worn area since the average depth is on the scale of 0.1 micrometers compared to the area of the wear tracks. The model also assumes that all surface areas created are parallel to the surface plane. These assumptions result in underestimates of the energy. Also, energy values are approximations based on an

average real area worn per pass. This real area is based on less than 10 measurements of waviness across the entire wafer plate.

Comparing values of the modeled energy of material removal to the input frictional energy provides some inconsistencies. There is a clear over estimation of energy of material removal for the copper wafer, high pressure, and low velocity experiment. This is believed to be a result of improper estimates of the depth of wear tracks since the wafer surface began with an average waviness on the same order most other worn copper wafers. There is also an overestimation of material removal energy with the silicon dioxide, low pressure, and low velocity experiment. The remainder of the material removal energies appear reasonable. These approximations are very simplified and prone to significant error due to inconsistencies in measurements. The depth of wear tracks across the entire wafer plate is characterized by five measurements of waviness. Attempting to characterize the average depth of tracks with these few measurements results in large estimation errors. For a more accurate estimation of the average wear track depth, a two-dimensional method of surface topography measurement should be applied to capture a larger representative sample. Additionally, a scale with settings that allow weight measurements of higher resolution is ideal for closer approximations.

Overall, the mass loss and waviness measurements provide quantities that are at least on the order of magnitude of the actual values. The computed energies of material removal are an approximation of the actual order of magnitude. These results provide information that energy of material removal is a significant fraction of the frictional

input energy. The mass flux term of dissipation in terms of wafer material removal in the thermomechanical model is significant, represented as $\frac{1}{\Theta}(\bar{q} \cdot \bar{\nabla}\Theta)$ in Equation 5.

4.3.1.4 Differential Scanning Calorimetry of IC1000 Pad Material

Differential scanning calorimetry (DSC) on IC1000 pad samples is conducted as a method to quantify potential changes in the chemical composition of the pad as a result of the CMP process. The computed enthalpies given from the measured heat flow provide a means to account for internal energy that is stored or released in the pad surface. Heat capacity is also computed and compared between each sample to observe potential clues of changing internal polymer structures. Pad samples that are run in DSC include six new pad trials, as a baseline. Trials are run with pad material collected from all eight planarization experiments. Each experiment has samples collected at the equivalent of 10, 50, 100, and 250 wafers polished. A new pad sample that has been soaked for 14 hours and then dried is tested in the DSC to isolate potential effects of the slurry. These trials are run using the procedure discussed in Section 3.3.3 with a maximum temperature of 225°C. Finally, three separate trials are run up to the higher temperature of 400°C. The pad samples tested at higher temperatures are from a new pad and polishing pad samples from the 250 wafer count, high pressure and high velocity planarization experiments. One sample is from the copper wafer trial and the other is from the silicon dioxide wafer. These two samples are used since they have the most energy input to them through planarization. It is expected these samples should provide the greatest deviation in results compared to the new pad material.

The heat flow contributions from the difference in mass of the aluminum sample and reference pans are removed for each trial. This correction provides a more accurate representation of the magnitude of heat flow into the pad material sample. The pan mass heat flow correction is carried out using Equation 47,

$$\left(\frac{\partial q}{dt}\right)_{Pan\ Corrected} = \left(\frac{\partial q}{dt}\right)_{Measured} + c_{p,Al}(m_s - m_r)\frac{dT}{dt} \qquad \text{Equation 47}$$

In this equation, $c_{p,Al}$ is the specific heat of aluminum, m_s is the sample pan's mass, and m_r is the reference pan mass. Specific heat of aluminum at 25°C, equal to 0.900 J/(g K), is used (Shackelford and Alexander 2001, 375). The specific heat of aluminum changes with temperature, but the change is consistent for each sample relative to the pan mass difference. The magnitude of heat flow measurements are thus comparable considering the pan mass difference. The sample pan mass is the total mass of the sample pan and lid minus the pad sample mass. After the heat flow measurements are corrected for the pan mass difference, the corrected heat flow is normalized with the pad sample mass. This normalization allows for computation of heat flow and enthalpies independent of the amount of material present.

A representative DSC thermogram of a new pad sample is presented in Figure 65. Traces of the mass normalized heat flow with temperature are shown for the first heating, cooling, and second heating. Endothermic reactions are represented with negative heat flow for each thermogram, so that heat going into the sample is identified as negative heat flow. The cooling curve is presented here as negative cooling, or the heat flow multiplied by negative one, to compare the heat flow to the heating curves more easily. This states that when cooling, heat is leaving the sample while in heating

it is entering the sample. For the cooling trace, the temperature range starts at 225°C and cools to -75°C.

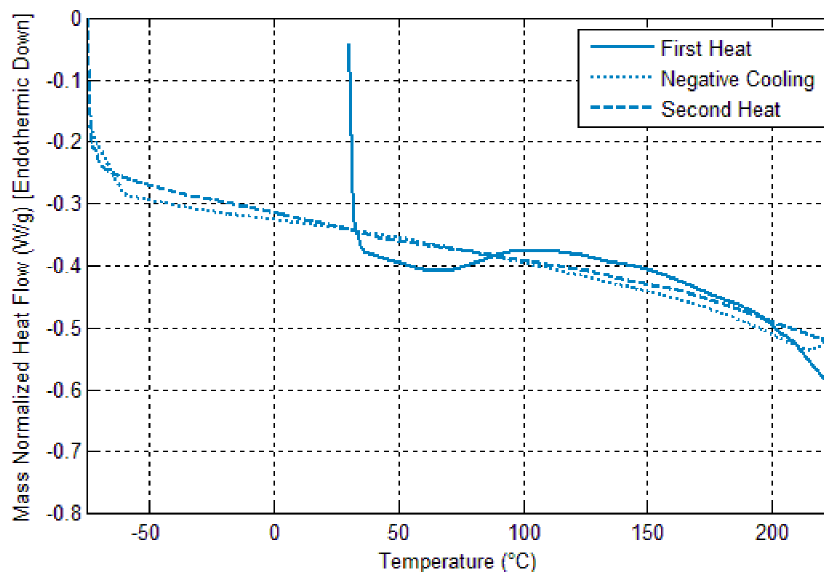

Figure 65: Differential Scanning Calorimetry Thermogram of a New Pad Sample (Trial 3)

At the beginning of each of the first heat, second heat, and negative cooling traces, Figure 65 shows a sharp drop in heat flow. These are start-up transients of the DSC instrument, which is a result of the larger heat capacity of the sample pan compared to the empty reference pan (Brown 1998, 691; Thomas). This is not a result of reactions within the IC1000 pad material. After the sharp transition in slope of the heat flow with temperature is the point where proper thermal analysis data is obtained. The cooling trace shows a second transient as it reaches the -75°C. This is a result of the DSC instrument changing cooling rate just before it reaches its coldest temperature. The DSC

cannot handle such a high cooling rate for these temperatures as the nitrogen gas that cools the DSC cell is only approximately -82°C.

Initial observation of the thermogram shows that the second heating and negative cooling curves coincide. These curves have a nearly flat negatively-sloped line with nearly the same slope. The first heating trace has a much different behavior with two peaks in the heat flow, as opposed to a flat line. These deviations represent thermal reactions which occur in the IC1000 pad material in these temperature ranges. They are irreversible reactions since they do not occur in the cooling or second heating of the sample. A reaction peak is considered a deviation from the baseline. In this case, the second heating peak can be considered as the baseline. The resulting DSC data from the other pad samples appear very similar to that of Figure 65 with minor differences.

It is unknown what irreversible reactions are occurring during the initial heating of the IC1000 polyurethane. With no information on the chemical composition of the specific polyurethane, results from the literature cannot properly be utilized. DSC thermograms of polyurethanes in literature that have been analyzed do not show similar heat flow trends, so results are not comparable. The literature has very little DSC analysis of CMP polishing pads. Published research that has performed DSC on polyurethane polishing pads shows similar DSC trends (Tregub 2003, 101-110). This research suggests that the irreversible reactions are a result of the breakup of crystalline regions from depolymerization, with reference to work done on thermoset polyurethanes (Dickie 1997, 347-352). Further analysis should be performed to be certain of the reaction types taking place.

In nine of the thirty nine low temperature DSC trials performed, the heat flow deviation may or may not cross over the second heating curve. There is no particular trend in which they do or do not overlap with the variables being compared. A potential cause for the upward shift of the baseline is from a loss of material mass. Each pad sample pan is weighed after its DSC trial is completed, and the average mass loss is 0.01 mg, with the largest mass loss of 0.16 mg. This change in mass does not account for the variation in second heat shifting with respect to the first heating. DSC data for all new pad samples tested is given in Figure 66. Thermograms of the four pad samples taken from the copper wafer, high pressure, high velocity experiment are shown in Figure 67. Calorimetry results of the silicon wafer with high pressure and high velocity are presented as well in Figure 68. The results of both figures are shown with the results of a new pad for comparison. These trials are chosen to compare first since the pad samples have the most energy put into them from high velocity and pressure. More changes in these results are expected compared to other pad samples.

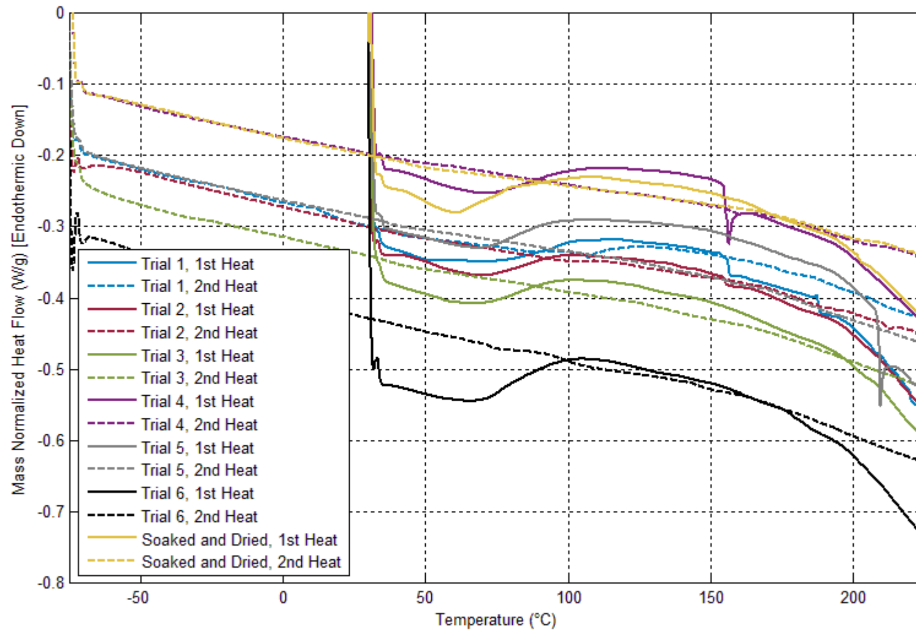

Figure 66: Calorimetry Results from New Pad Samples

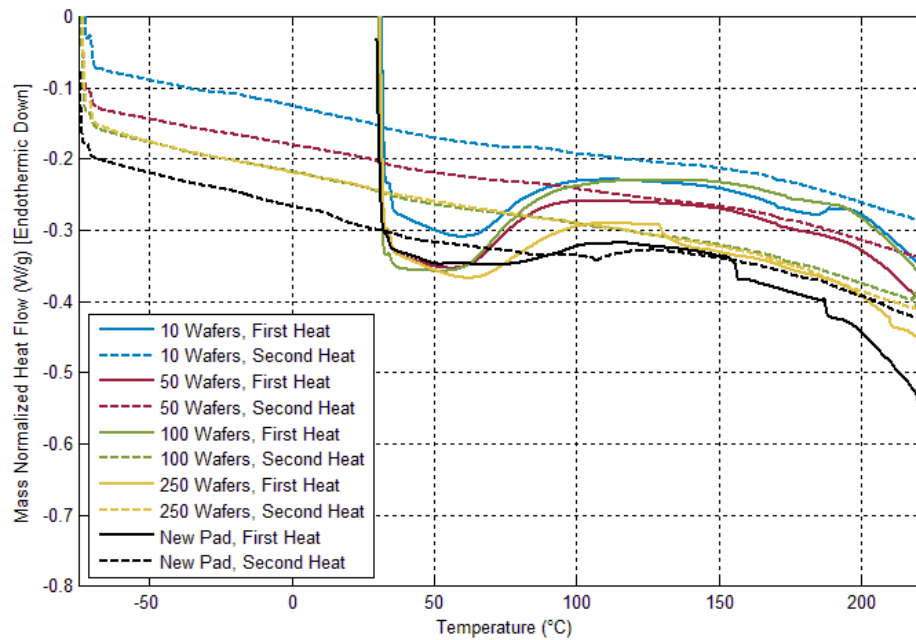

Figure 67: Calorimetry Results from Copper Wafer, High Pressure, High Velocity Pad Samples with New Pad Results of Trial 1

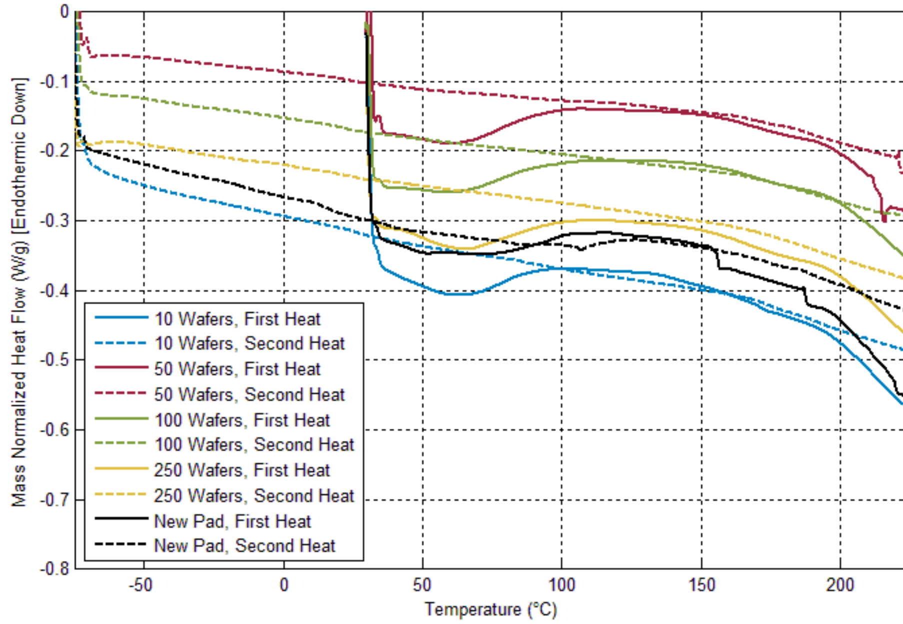

Figure 68: Calorimetry Results from Silicon Dioxide Wafer, High Pressure, High Velocity Pad Samples with New Pad Results of Trial 1

All data from Figure 66 though Figure 68 show the same basic trends as previously discussed in the first and second heating. Cooling curves are not shown here so that the heating curves are the current focus of analysis. The main differences between heat flow versus temperature curves from each trial are the shift in baselines and subtle deviations in the smooth curves of most trials. The small deviations in heat flow are represented as small jumps and peaks along the larger peak curve during the first heat. The only repeating small features is a decreasing jump of heat flow at approximately 160°C, which is seen in the new pad samples of Figure 66. This deviation also occurs in six other trials of worn pads near 160°C. The DSC thermograms of the remaining trials not presented in this section can be seen in Appendix 6.3. There appear to be no trends with this deviation, nor with any variable taken into account with these

experiments. The same is true for any other small deviation in the heating curves. These features may be a result of artifacts in the experiments. Potential artifacts include mechanical shock of the DSC cell or pans, and pieces of the pad sample falling over on to the pan surface from heating. Both occurrences result in sharp transitions in heat flow.

To observe potential trends in the shift of the baseline with variables of importance, the data is presented in a way that allows for viewing results of all trials in one graph. These variables include wafer count, wafer material, pressure, velocity, temperature, and specific heat. This baseline shift is analogous to a change in specific heat of the sample, as described in Equation 29 for total heat capacity. The specific heat of the sample is the negative of the normalized heat flow divided by the rate of temperature change. The negative value of this heat flow is taken as heat going into the sample is negative. Graphs of specific heat versus wafer count at 65°C for the first heat and second heat are presented in Figure 70. Figure 69 show similar information but present values of specific heat at 220°C.

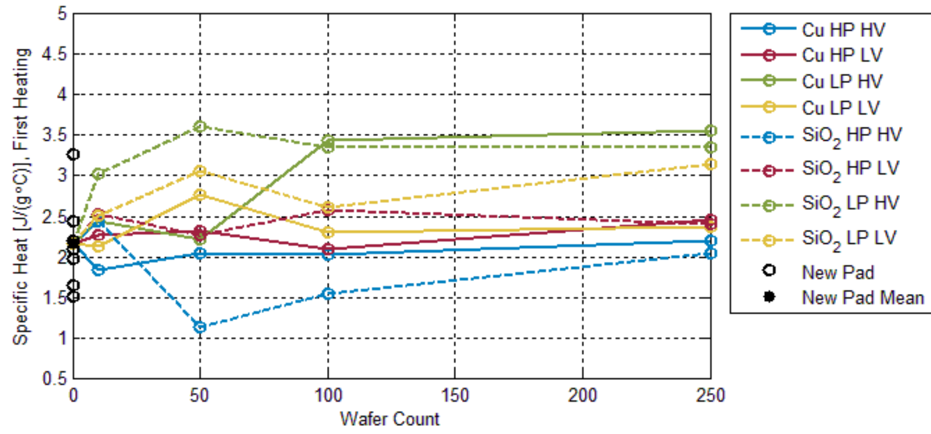

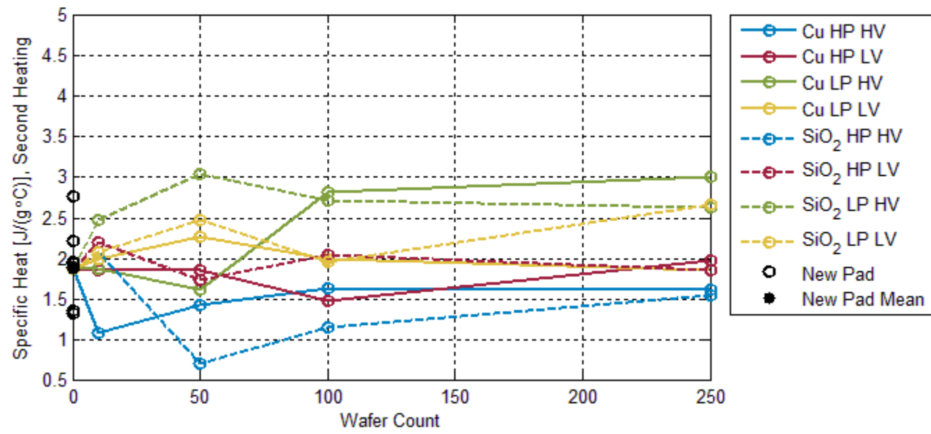

Figure 69: Specific Heat with Wafer Count at 65°C. Top: First Heating. Bottom: Second Heating.

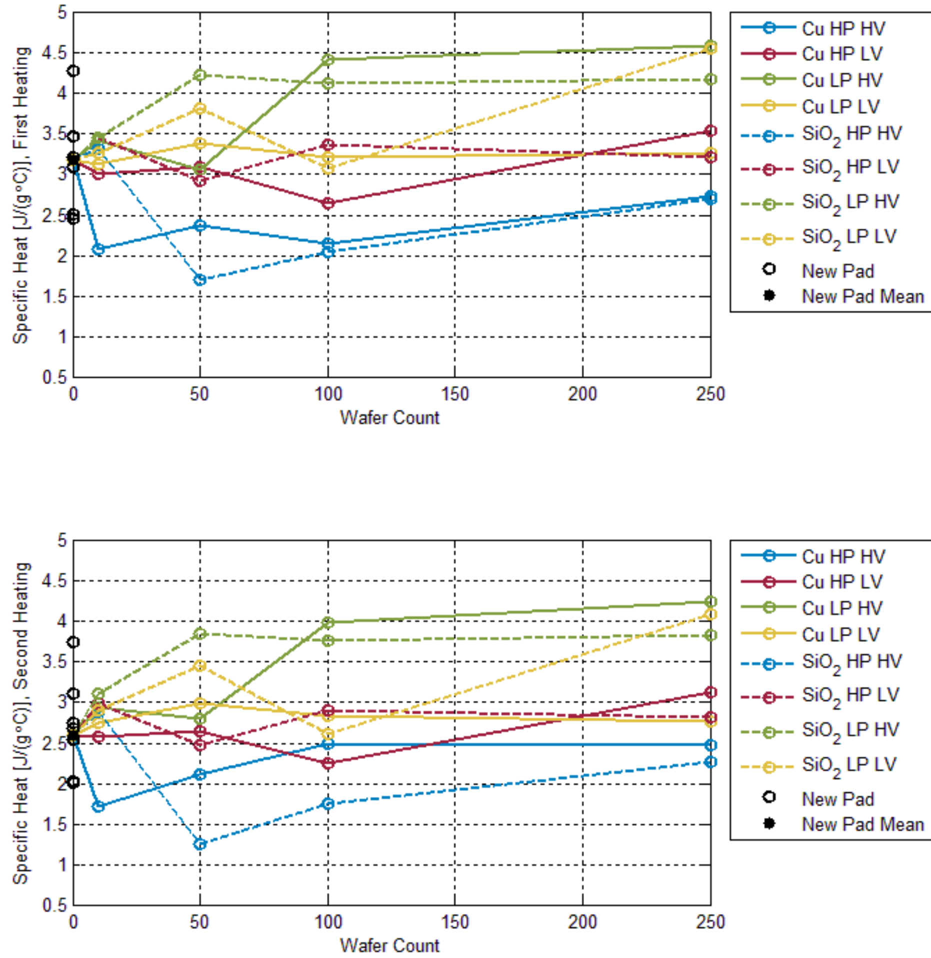

Figure 70: Specific Heat with Wafer Count at 220°C. Top: First Heating. Bottom: Second Heating.

The solid lines represent the copper wafer trials while the dotted lines are for silicon dioxide. The lines are color coded to match the copper and silicon dioxide wafer samples that have the same velocity and pressure. "HP" and "LP" represent high and low pressure, respectively. "HV" and "LV" represent high and low velocity, respectively. The black bar at 0 wafers in Figure 69 and Figure 70 represents the full range of specific heat values that the new pad trials covered. The black dot represents

the average specific heat of the new pad trials. All graphs, regardless of temperature and heating cycle, show similar trends. It appears that pad samples which were performed under the same boundary conditions in the tribometer are lumped together with specific heat. Yet, there appears to be no particular trend with specific heat and increasing velocity or pressure. Also, the majority of specific heat values fall within the range of new pad samples. Observation of the specific heat through various other temperature values and the cooling curves show no particular trends either. From these observations, it appears that the shift in the baseline or change in specific heat between samples is only a variation of the initial pad chemical composition, amount of slurry and wear particles, or experimental equipment errors.

This instrumental error is associated with thermal changes of the DSC heating cell, such as potential oxidation layers that may form when exposed to air. An iridium calibration sample was tested in the DSC six times to check for repeatability of the results. The sample was tested three times in a row while not being disturbed within the DSC cell. This procedure was carried out for a total of two separate times. The baseline shifted a maximum of 0.195 mW between calibration trials at the same heating rate of 10°C/minute. This heat flow is equivalent to a maximum of ±0.26 J/(g °C) of specific heat for the smallest pad sample tested, and does not account for the total heat capacity shown. Yet, these experiments do not account for the total possible extent of thermal changes of the DSC heating cell.

The results of the cooling DSC data show no additional information that the second heating does not show. A small feature in the cooling thermogram that occurred was a small peak at about -30°C. An example of this peak is shown in Figure 71. This

figure shows the actual cooling curve, as opposed to the negative cooling curve. The small peak occurred in five different trials, one of which was an un-soaked new pad sample. A similar peak also occurred during the second heating process of a separate sample as it passed through -30°C. Since the same peak occurs in a new pad sample and during the second heating of a separate sample, it is believed that these peaks are an artifact of the DSC experiment and do not represent a reaction of the pad sample. Artifacts that may produce this behavior can include an abrupt change of the heat transfer between the sample and pan or the pan and DSC cell (Schawe et al. 2000). Pad sample pieces can topple over if they are stacked in a certain way from change in temperature. The sample pan or DSC cell can suffer from a mechanical shock that abruptly changes the heat transfer. If these events were to occur, the DSC would quickly account for the disturbance with its feedback loop to maintain a constant temperature rate.

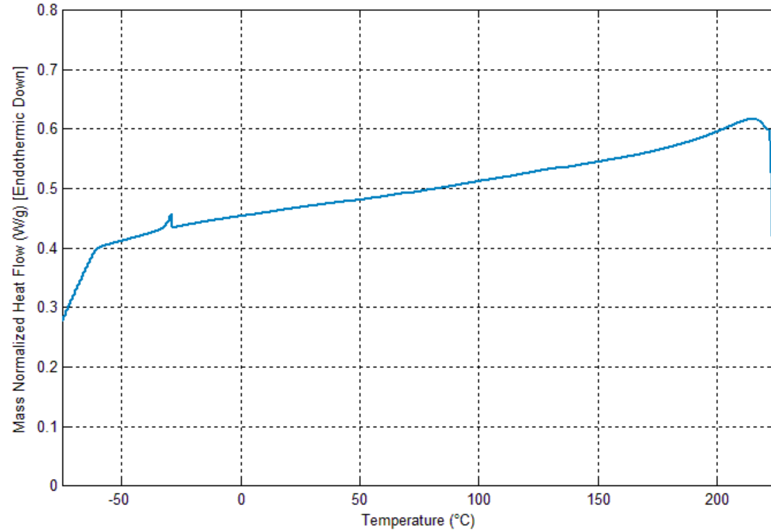

Figure 71: Cooling of Pad Sample from Copper Wafer, High Pressure, High Velocity Pad at 100 Wafer Count

Observations of thermal behavior of the IC1000 pad material is completed through the high temperature DSC trials presented in Figure 72. The heat flow data before 225°C for all three trials is in line with the previous trials, with similar deviations of heat flow for the first heating reactions. All of these reactions are irreversible as well since they do not occur during the cooling or the shown second heating. The large endothermic peak observed beginning at 250°C is a result of the decomposition of the thermoset polyurethane pad material. Thermogravimetric analysis (TGA) results of the same pad material in the literature shows that the material begins to lose mass after 250°C and continues to lose mass until about 500°C (Yang et al. 2010, 338-346). The mass of the pans were weighed after the high temperature trials. The new pad sample lost 63% of its initial mass, while the copper and silicon dioxide wafer polished trials lost 22% and 55% of their initials sample masses, respectively. This can be seen in the

second heating as there is an upward shift of the heat flow that is normalized to the initial pad sample mass. The TGA results of the pad material states that approximately 60% of the sample mass is removed at 400°C. The small mass decrease of 22% in the pad sample polished on copper compared to the other two samples may be a result of significantly more wear and slurry particles that exist in that particular tested pad sample, or from internal changes of the polyurethane structure from polishing.

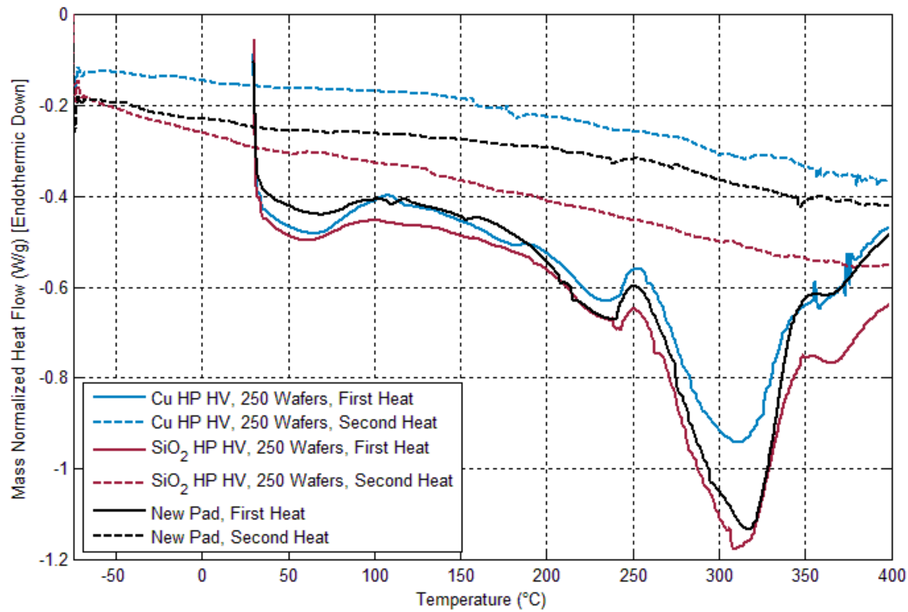

Figure 72: Calorimetry Results of IC1000 Pad Samples to 400°C

To quantify the magnitude of internal energy dissipation into the pad samples from CMP, the enthalpies of irreversible reactions in the first heating are computed. These calculations are based on the areas under the total first heating curve. The area under the curve is mathematically represented as enthalpy by Equation 30 after insertion of heat flow divided by time rate change of temperature. Typically enthalpies of reaction

are measured from the area under reaction peaks relative to the baseline heat flow. The baseline heat flow from these DSC results are challenging to determine between trials as the structure of the heat flow reaction curves vary. Calculating the area under the entire heat flow curve isolates any error that would be associated with defining baselines and the separation of reaction heat peaks. Additionally, the area under the total first heating heat flow curve represents the amount of energy that went into the pad sample when it was heated the first time. This value thus provides a simple measure of energy dissipation into the pad material.

To isolate variations of measurements due to the change in specific heat between trials, the values of second heat flow for a specific temperature are gathered. Then, the second heat flow values at a specific temperature are set equal to a single value by shifting all of the heat flow data evenly though the entire temperature range. The second heating values are used for shifting since these values do not contain variations due to the irreversible reactions during the first heat. With the heat flow shift, the deviations of heat flow data from differences in specific heat are removed. To acquire specific enthalpies of reaction, the area under the mass normalized heat flow curves are computed and divided by the heating rate, which is 10 °C per minute. These calculations are performed using the *trapz* trapezoidal integration function in MATLAB. A temperature of 50°C was chosen as the second heat flow shifting temperature. Trends observed in the results of specific enthalpy do not vary with this chosen shifting temperature.

The values of enthalpy of reaction were statistically tested with the modified Thompson tau technique to identify outliers in the data (Anbarasi et al. 2011, 512-516).

Removal of outliers provides a better observation in trends of the specific enthalpy with the variables of interest. Values of enthalpy of all trials that had polished the same number of wafers were compared. The difference of each data point from the sample mean was compared to the product of the standard deviation of the data set and the corresponding Thompson tau value. If the difference is larger, the data point is statistically considered an outlier. Three outliers were found which include the new pad samples from trial 5 and 6. The remaining outlier was found to be the enthalpy value from the copper wafer, high pressure, and high velocity planarization experiment sample at 100 wafers polished. The remaining results of specific enthalpies are shown in Figure 73.

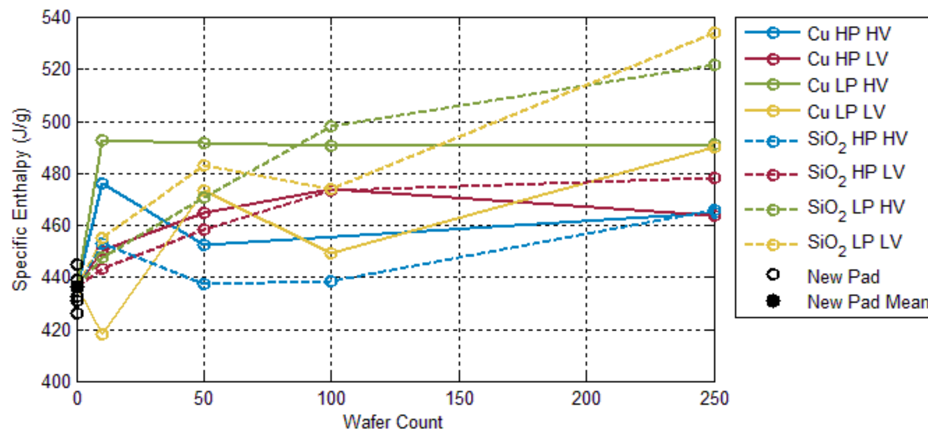

Figure 73: Specific Enthalpy of Reaction from IC1000 Pad Irreversible Reactions

Values of total specific enthalpy for the first heating have a general increasing trend with increasing wafer count. Greater wafer count correlates to a larger amount of energy transferred into the pad material through the planarization experiments. These

results suggest that energy is dissipated into the pad surface's material structure from the process of CMP. A dissipation of energy into the surface proposes that a chemical change within the polyurethane pad occurs from CMP, which may affect its mechanical characteristics and can influence scratch production. The value of $\rho\dot{u}$, in terms of the internal polymer structure associated with these irreversible reactions, may be a significant quantity that influences scratch production. The importance of this energy dissipation on the pad scratching process is to be determined in future experimentation.

4.3.1.1 Dimensional Analysis of CMP Planarization Results

Dimensional analysis of the results from various experiments is performed in an attempt to view trends between data sets. A dimensionless pi group is formed based on parameters related to the planarization experiments, given in Equation 48,

$$\Pi = \frac{\gamma\mu}{\rho R_a h} \qquad \text{Equation 48}$$

This pi group contains variables associated with the tribometer forces with the friction coefficient, pad surface topology, and enthalpy of reaction. In this case the enthalpy of reaction from the peak in DSC between 35°C and 100°C is used. Average roughness and enthalpy of reaction are values that are measured from each pad sample, so the pi group is plotted against wafer count from 0 wafers to 250 wafers. The value for coefficient of friction is taken as the value right before the sample was taken in the tribometer experiments.

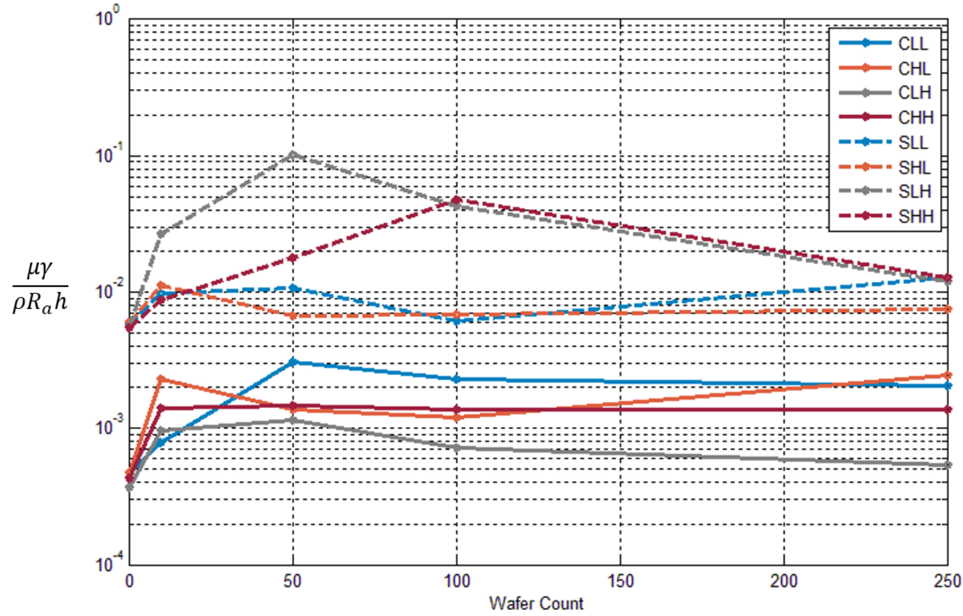

Figure 74: Planarization Experiment Pi Group

Figure 74 shows that there is an initial jump in the value of the planarization pi group from 0 to 10 wafers. It is after this that the values do not have any particular trend with wafer count. The greater overall magnitude of silicon dioxide values is due to the larger magnitude of γ/ρ for silicon dioxide. If the contributions of these constants were removed, the values would fall on top of each other. The main contributors to the initial increase and leveling of the pi group value is the coefficient of friction and average pad roughness. The specific enthalpy of reaction appears to just add variation to the values. These observations reiterate those already stated that the specific enthalpy of reaction shows no trends with the variables tested. Coefficient of friction and pad surface roughness both show an initial drop in magnitude within the equivalent 50 wafers polished. After this initial drop, the values stay relatively constant with some variation. The trends of the pi group reflect these previous findings.

CHAPTER 5

CONCLUSIONS

5.1 Conclusions

A thermomechanical model for chemical-mechanical planarization (CMP) was established. This model provides a means to identify physical processes and behaviors that produce damage on the wafer in the form of scratches. Tracking the processes of energy dissipation and mechanical behaviors of the planarization method supplies the information that is essential in scratch prevention. Numerous experimental and analytical methods were utilized to gather information for observing trends and quantifying various factors of the general model.

Mechanical behavior of a common porous polyurethane polishing pad was characterized through several methods. Kinematic behavior of the polishing pad material under compressive strains was observed and quantified by monitoring the deformation of a pad sample with digitally captured videos. Various measures of the porous pad's compressibility provide information needed to quantify true stresses in the material. Results show that the compressibility of the pad material is significant with its porous structure. Not accounting for this change in Jacobian was shown to underestimate the true stress of the pad material when analyzing stress fields within the sample.

Time dependent mechanical behavior of the polishing pad was also characterized through compression and tension stress relaxation experiments. The literature has experimentally measured mechanical properties of polishing pads mainly in tension or bending, as the experimental equipment is readily available for these type of experiments. Yet, polishing pads are loaded in the compressive mode of deformation in CMP. A compression testing setup was fabricated and utilized to measure stress relaxation of the pad material. Results were compared to tensile stress relaxation experiments. Time constants of relaxation for compression experiments had an inverse relation with applied normal stress, stating that the material relaxed less over time at higher levels of applied normal load. Tensile relaxation experiments had a positive relation between relaxation time and applied stress. Different mechanical behaviors exhibited in compression compared to tension resulted in key information that this polishing pad material should be characterized in compression for CMP modeling.

Additional compression stress relaxation experiments were conducted to observe the mechanical effects of soaking the pad in aqueous materials. Experimental results showed that pad material soaked in distilled water or CMP slurry had a smaller stress relaxation time than new pad material. The pad relaxed more over time if water enters its material structure, even if it has been dried. These results imply that a soaked pad reduces the amount of damage produced on the wafer, as the contact stress analysis suggests. A soaked pad relaxes the stress applied to the wafer more over time. Additionally, it was found that pad samples which were used in planarization experiments that had polished an equivalent of 100 and 250 wafers relaxed more than that of 50 wafers. These results suggest that a pad is “broken-in” more with use and thus

produces less scratches on wafers since it would apply less stress. An important result obtained from the polishing pad relaxation experiments is that the viscoelastic strain energy that is dissipated during CMP is significant and must be accounted for. This viscoelastic strain energy is also a function of soak time in slurry, and may potentially be a function of polishing time of the pad material.

Experiments were conducted to replicate the chemical-mechanical planarization process to gather information about the forces involved with the pad and wafer contact, topographical surface changes, and dissipated energy. Planarization experiments were performed through a range of boundary conditions that are used in CMP to gather complete information about the process. Forces that act between the pad and wafer contact were measured through the planarization process. Coefficients of friction results showed a general decreasing trend over polishing time. The results are in agreement with those in the literature that state scratching is reduced if the pad has been 'broken-in'. With a smaller coefficient of friction, there is less stress on the wafer from the pad material so less damaging scratches are produced. Contact stress analysis showed that the wafer cannot be yielded by a softer pad asperity unless the coefficient of friction of the contact is greater than 0.3. Properties of the pad surface that resulted in this reduction in the coefficient of friction could be manufactured to be in a new pad.

Topographical measurements of the pad surface showed that there is a reduction in roughness of the surface with polishing time. These results suggested that a smoother pad sample had an influence in the smaller coefficient of friction that can reduce killer scratches on integrated circuit wafers. A smoother surface also reduces the load that relatively tall asperities would produce on the wafer surface. This reduces the von Mises

stress on the wafer to produce less damage. Furthermore, smoothing of the pad surface explains that the pad surface was plastically deforming. Energy dissipation associated with this plastic deformation of the pad surface has been shown to be an important aspect of pad scratching.

A model for the estimation of wafer material removal energy was constructed and applied to the results of the planarization experiments. The results showed that the energy put into material removal is a significant portion of the input energy from frictional tractions. Energy dissipation into mass flux is thus an important quantity of the CMP thermomechanical model.

Differential scanning calorimetry (DSC) was conducted on samples of pad material gathered from the planarization experiments. These experiments provided a method to quantify any energy that was dissipated during CMP to alter the chemical structure of the pad material. Calorimetry results showed that enthalpies of reaction computed increased with increasing equivalent wafers polished. This internal energy dissipation may potentially effect the mechanical characteristics of the pad surface. Thus, internal energy dissipated into the pad material may have a significant influence on pad scratching.

The resulting thermomechanical model of CMP makes no assumptions to neglect potential sources of energy dissipation. Acoustic fluxes of the CMP contact, sensible heat generated, and mass flux of the pad material were determined negligible for the planarization experiments performed. This may not be the case for actual CMP processes due to diamond conditioning of the pad surface and the continual rotation of the pad on the wafer. The viscoelastic strain energy in the Clausius-Duhem inequality

has been found to be significant through the pad relaxation experiments. Plastic deformation terms of strain energy are known to be important due to damage that is produced on the wafer as well as plastic deformation from smoothing of the pad surface. The mass flux of wafer material provided a significant amount of energy dissipation that must be accounted for in CMP modeling. Finally, the internal energy dissipated into the pad material was found to increase with polishing time. Thus, the internal energy dissipation may be significant to scratch production processes. The analysis conducted provides the initial framework for CMP thermomechanical modeling. The model provides a means to obtain a complete understanding of wafer damage processes by accounting for all forms of energy dissipation.

5.2 Future Work

The analytical and experimental analysis performed in this work unveiled thermomechanical processes that are important and must be accounted for with CMP modeling. The model and results obtained lay the groundwork for additional construction of the thermomechanical model of CMP. Supplementary work should be conducted to improve upon the data and analysis performed here as well as add other aspects of the process to complete the physical description of the CMP.

Characterization of pad materials in compression should be performed with an improved experimental setup. Ideally, a commercially available mechanical testing device such as a dynamic mechanical analysis (DMA) instrument should be used for compression relaxation and creep experiments. These devices are accurate in the range

of deformations and loads required to characterize the time dependent behavior of polishing pads for CMP. If a DMA instrument is unavailable, a new or modified version of the compression test setup fabricated in this work should be applied. A button style load cell should be used in place of the cantilever style to remove load cell bending that prohibited the measurement of strain with the optical setup. This load cell style will also improve upon the uniformity of displacement applied to the sample being tested. The compression block should be constrained from movement after the desired displacement is set. Such a change will reduce the amount of creep in the system. A final suggestion is to construct the setup of a less compliant material than aluminum, such as steel, to improve upon system rigidity for more accurate strain measurements.

Compression relaxation and creep experiments should be performed on used pad samples of various experimental conditions. These results will provide additional confidence in the relaxation behavior of used pad materials through CMP processes. With strain measurements and these additional trials, a more complete model of the IC1000 stress relaxation is obtained.

The stress analysis can be improved with additional explicit mathematical descriptions of the time dependent stress field that acts on the wafer from the pad. Effects of plastic deformation of the pad asperities should also be included to account for the change in contact pressure distribution. Investigation of adhesive contact forces on the pad asperity and wafer surface should be performed to discern any potential effects. These analyses will also provide a more complete quantification of the strain energy terms including elastic, viscous, and plastic deformations.

Planarization experiments that replicate the CMP process should be performed under more similar conditions as actual CMP using different equipment. A setup that consists of a rotating wafer and pad will wear the material in a closer manner to actual CMP. Measurements of forces, topography, and thermodynamic properties will be more accurate. The use of constantly flowing slurry that is either drained from the system or continually filtered would remove large particles from the system. Such a slurry system is used in CMP to reduce the amount of damage that is produced by large particles in the slurry. With this improvement, damage that is produced on the wafer will be closer to that of an actual CMP process.

For continuation of the thermomechanical modeling of CMP pad scratching, the terms in the resulting dissipation term should be quantified to determine the contributions of each term to the CMP process. Further empirical data needs to be gathered to quantify the strain energy that results in plastic deformation of the wafer and pad materials. A method to quantify the mass loss and energy of material removal for polishing pads during CMP should be produced to account for this dissipation of energy. Further DSC analysis of used pad samples should be conducted through thermal decomposition of the material to quantify additional energy dissipation from other thermal reactions. A two-dimensional roughness measurement system should be applied in measurement of wafer wear track depth. This would provide a better approximation for energy of wafer material removal, which is accounted for with the fluxed energy dissipation.

Finally, mechanical changes to the pad material surface should be measured through the CMP process for better understanding of the mechanical properties that

influence scratch production. These results should be related to those found from polishing pad DSC experiments for internal energy dissipation quantification. Implementation of these aspects of mechanical behavior and energy dissipation will provide a more complete understanding of the CMP pad scratching process. A CMP model that contains more physical information about the process will unveil additional methods to improve wafer manufacturing yields.

APPENDICES

6.1 MATLAB Code for Strain and Stress Analysis of Compression Relaxation

```
%% Compute strain of each step (change in distance between plates)
% Require good contrast between edges and center of plates
close all

name = '0.13_1'
lim = 0.5 % BW limit
NumSq = 6;

Vid=VideoReader([name,'.avi']);
i=1;
 while hasFrame(Vid)
            vidFrame(i).data = readFrame(Vid);
            i=i+1;
 end
FrameCount = round(Vid.FrameRate*Vid.Duration);
Dist = zeros(FrameCount,1);
for f = 1:FrameCount
I = vidFrame(f).data;
BW = im2bw(I,lim);
s = size(BW);
col = s(2)/4;
BW=imfill(BW,'holes');

% Remove 4-connectivity pixels so boundary can be traced properly
CC = bwconncomp(BW,4);
Li = CC.PixelIdxList;
for e = 1:length(Li)
    ind = cell2mat(Li(e));
    s = length(ind);
    if s < 100
    BW(ind)=0;
    end
end

BWI=imcomplement(BW); s=size(BWI);
row=find(BWI(s(1)/2:end,col),1)+s(1)/2-1;
B = bwtraceboundary(BWI,[row col],'S',4,640*4);
n=1;
Bfit = B(1:525-(640/4),:);

% Least Squares Fit of Outline
p = polyfit(Bfit(:,2),Bfit(:,1),1);
x = 1:n; y = p(1).*x+p(2);

% Compute rotation angle and rotate image
AngDeg = atan(p(1)).*(180/pi); % Degrees
BWrot = imrotate(BW,AngDeg);

% Extract center space (assume space between plates is largest)
BWDist_s = bwpropfilt(BWrot,'Area',1,'largest');
```

```
BWDist=imfill(BWDist_s,'holes');

% Compute average distance between plates (center 1/2th of image)
Sz = size(BWDist);
Start = round((1/4)*Sz(2)); End = round((3/4)*Sz(2));
Dist_i = zeros(End-Start+1,1);
for i = Start:End
D = BWDist(:,i);
egi = find(D);
Dist_i(i-Start+1) = max(egi) - min(egi) + 1;
end
Dist(f) = mean(Dist_i);
end
figure(), imshow(BWDist)

%% Initial strain based on first video frame
Strain = -(100*(Dist-Dist(1))./(Dist(1))); % Percent Strain
t_vid = round(0:1/(Vid.FrameRate):(Vid.Duration-(1/(Vid.FrameRate))),2); %
Seconds
figure()
plot(t_vid,Strain), xlabel('Time (sec)'), ylabel('Compressive Strain (%)')

%% Load and Stress
Dat = dlmread([name,'.xls']);
Bridge = Dat(1:2:end,:); % mV/V
Offset = mean(Bridge(1:100));
TimeL = (Dat(2:2:end,:)-Dat(2,1))./1000; % s
t_load = round(0:0.04:(length(Bridge)/25)-0.04,2); % sec, Captured at 25 Hz
F = (Bridge - Offset)/(0.091723); % lbf
Area = NumSq*0.25^2;
Stress = F./(Area); % psi
figure()
plot(t_load,F), xlabel('Time (sec)'), ylabel('Force (lbf)')
figure(), plot(t_load,Stress)
figure(), semilogx(t_load,F)
Da = [t_load',F,Stress];

% Sync times with peak load and held strain
t_vid_hold = input('What is the time of held strain? ');
Ih = find(t_vid == t_vid_hold);
F_peak = max(F);
Ip = find(F == F_peak);
Strain_ = zeros(length(t_load),1);
Strain_sync = [Strain_(1:Ip-Ih,1); Strain; Strain_(length(Strain)+Ip-
Ih+1:end,1)];
Dist_sync = [Strain_(1:Ip-Ih,1); Dist; Strain_(length(Strain)+Ip-
Ih+1:end,1)];
Strain_sync((Ip-Ih):(length(Strain)+Ip-Ih-1)) = Strain';

%% Set zero point for strain in time, based on initial load increase (after
initial slack is taken up)
t_zero = input('What is the zero time for load? ');
It = find(t_load == t_zero);
t_new = round(0:0.04:(((length(Bridge)/25))-0.04-t_zero),2); % at 25 Hz

F_new = F(It:end); % lbf
Stress_new = F_new./(Area); % psi

Strain_zero = -(100*(Dist_sync-Dist_sync(It))./(Dist_sync(It))); % Percent
Strain zeroed
Strain_new = round(Strain_zero(It:end),5);
```

```
t_load_peak = t_load(Ip);
endt = t_load_peak;
endpt = find(t_new == endt)-It;
t_pl = t_new(1:endpt(1)-1)';
Stress_pl = Stress_new(1:endpt(1)-1);
Strain_pl = Strain_new(1:endpt(1)-1);
Force_pl = F_new(1:endpt(1)-1);
Data = [t_pl,Force_pl,Strain_pl,Stress_pl];

%% Stress and Strain
figure()
plot(Strain_pl,Stress_pl)
xlabel('Strain (%)'), ylabel('Stress (psi)')
text(0.1,3,['Load Time: ',num2str(t_load_peak-t_zero),' sec'])
text(0.1,2.5,['Max Load: ',num2str(F_peak),' lb_f'])

%% Strain and Stress with time
figure()
[ax,p1,p2] = plotyy(t_pl,Strain_pl,t_pl,Stress_pl);
ylabel(ax(1),'Strain (%)')
ylabel(ax(2),'Stress (psi)')
xlabel(ax(2),'Time (sec)')
```

6.2 MATLAB Code for Compressibility Measurements of the IC1000 Pad

```
% % Compressibility Image Processing
% % Reads a grayscale video of pad sample as it is compressed.
% % Estimate strain by compression plate edge change in length.
% % Estimate change in volume by change in width and thickness of pad sample.
% % Estimate Poisson's ratio and dilatation
close all
name = 'D8'
limit = 0.4;  % BW limit
flag = 1; % Set flag = 1 to view binary images to check if proper limit is
set

% Read video file
Vid=VideoReader([name,'.avi']);
i=1;
 while hasFrame(Vid)
            vidFrame(i).data = readFrame(Vid);
            i=i+1;
 end
FrameCount = Vid.FrameRate*Vid.Duration;

% Define output variables for loop
Width_pad = zeros(FrameCount,1);
Thick = zeros(FrameCount,1);
Area = zeros(FrameCount,1);
for f = 1:FrameCount
I = vidFrame(f).data;
BW = im2bw(I,limit);
BW = imfill(BW,'holes');
BW = bwpropfilt(BW, 'Area', 1);
% Remove 4-connectivity pixels so boundary can be traced properly
```

```
CC = bwconncomp(BW,4);
Li = CC.PixelIdxList;
for e = 1:length(Li)
    ind = cell2mat(Li(e));
    s = length(ind);
    if s < 100
    BW(ind)=0;
    end
end
%% Rotate image for proper strain and width measurement
s=size(BW);
col = round(s(2)/3);
BWI = flip(imcomplement(BW),1);
row=find(BWI(s(1)/2+1:end,col),1)+s(1)/2;
B = bwtraceboundary(BWI,[row, col],'S',4,640*4);
Bfit = B(1:round(1*s(2)/3),:);
% Least Squares Fit of Outline
p = polyfit(Bfit(:,2),Bfit(:,1),1);
x = 1:s(2); y = p(1).*x+p(2);
% Compute rotation angle and rotate image
AngDeg = atan(p(1)).*(180/pi); % Degrees
BWrot = imrotate(BW,-AngDeg); Irot = imrotate(I,AngDeg);
BWrot = bwpropfilt(BWrot, 'Area', 1);
%% Area of Pad
O =
regionprops(BWrot,Irot,{'Area','Centroid','WeightedCentroid','MinorAxisLength
'});
Area(f) = O.Area(1);

%% Measure average width of sample
Width_i = zeros(s(1),1);
for i = 1:s(1)
    Width = BWrot(i,:);
    W = find(Width);
    if isempty(W) == 1
        W = 0;
    end
    Width_i(i) = max(W) - min(W) + 1;
end
% Take only values above 80% of maximum width, as ends will give errors
indicies = Width_i < (0.80*max(Width_i)); Width_i(indicies) = [];
Width_pad(f) = mean(Width_i); % Pad Width

%% Measure thickness strain of image
% Compute average distance between plates (center 1/4th of image)
Start = round((2/4)*s(2)); En = round((3/4)*s(2));
Thick_i = zeros(En-Start+1,1);
for i = Start:En
D = BWrot(:,i);
egi = find(D);
Thick_i(i-Start+1) = max(egi) - min(egi) + 1;
end
Thick(f) = mean(Thick_i); % Pad thickness

%% Plots
if flag == 1
if f == 1
    figure(), imshow(BWI), hold on
    plot(Bfit(:,2),Bfit(:,1),'r')
    plot(x,y,'g');
        text(530,400,['Image = ', num2str(f)])
```

```
        figure(), plot(Width_i)
end
if f == 150
    figure(), imshow(BWI), hold on
    plot(Bfit(:,2),Bfit(:,1),'r')
    plot(x,y,'g');
        text(530,400,['Image = ', num2str(f)])
        figure(), plot(Width_i)
end
if f == 300
    figure(), imshow(BWI), hold on
    plot(Bfit(:,2),Bfit(:,1),'r')
    plot(x,y,'g');
        text(530,400,['Image = ', num2str(f)])
        figure(), plot(Width_i)
end
end
end
Strain_t = -((Thick-Thick(1))./(Thick(1))); % Compressive Strain Thickness
figure(), plot(Strain_t), xlabel('Data Point'), ylabel('Strain')

%% Remove end points of no movement
St = input('What is the strain start point? ');
En = input('What is the strain end point? ');
Thick_new = Thick(St:En);
Strain_t_new = Strain_t(St:En);
Width_new = Width_pad(St:En);
Width_Strain_new = ((Width_new-Width_new(1))./(Width_new(1))); % Strain Width
Area_new = Area(St:En);

%% Poisson's Ratio Approximation
Poisson = -Strain_t_new./Width_Strain_new;
figure(), plot(Poisson)
figure(),
h=plot(-Strain_t_new,Width_Strain_new,'.');set(h,'markersize',8), hold on
xlabel('Axial Strain'), ylabel('Transverse Strain')
axis([-inf 0 -inf inf])
P = polyfit(-Strain_t_new,Width_Strain_new,1)
Widthfit = P(1).*(-Strain_t_new)+P(2); plot(-Strain_t_new,Widthfit,'r')
    yresid=Width_Strain_new-Widthfit;
    SSresid=sum(yresid.^2);
    SStotal=sum((Width_Strain_new-mean(Width_Strain_new)).^2);
    r_sq=1-(SSresid/SStotal)
text(-18.5/100,2/100,['\bf Linear Regression:']);
text(-18/100,1.75/100,['R^2 = ', num2str(r_sq)]);
text(-18/100,1.4/100,['Slope = ', num2str(P(1))])
text(-18/100,1.1/100,['Intercept = ', num2str(P(2))])
text(-7/100,3/100, ['Limits of Strain: ', num2str(St),' to ',num2str(En)])
text(-6.75/100,3.25/100,['B&W Limit = ', num2str(limit)])
legend('Data','Linear Regression'), grid on

%% Jacobian (width)
figure(), plot(Strain_t_new,Width_new,'*'),
xlabel('Compressive Strain'), ylabel('Average Width of Pad Sample (pixels)')
figure(), plot(Strain_t_new,Area_new,'*')
xlabel('Compressive Strain'), ylabel('Area of Pad (pixels)')

V_ow = Thick_new(1)*Width_new(1)^2; % pixels^3
V_cw = (Thick_new.*(Width_new.^2)); % pixels^3 (with respect to original
volume)
Jw = V_cw/V_ow; % Jacobian
```

```
figure(), h=plot(Strain_t_new,Jw,'.'), set(h,'markersize',8),hold on

xlabel('Compressive Strain'), ylabel('Jacobian')
[Pjw,S] = polyfit(Strain_t_new,Jw,1); Pjw
Jfit = Pjw(1).*Strain_t_new+Pjw(2); plot(Strain_t_new,Jfit,'r')
    yresid=Jw-Jfit;
    SSresid=sum(yresid.^2);
    SStotal=sum((Jw-mean(Jw)).^2);
    r_sq=1-(SSresid/SStotal)
legend('Data','Linear Regression')
ylim=get(gca,'ylim'); xlim=get(gca,'xlim');
text(0.25/100,0.94,['\bf Linear Regression:']);
text(0.5/100,0.93,['R^2 = ', num2str(r_sq)]);
text(0.5/100,0.92,['Slope = ', num2str(Pjw(1))])
text(0.5/100,0.91,['Intercept = ', num2str(Pjw(2))])
text(12.75/100, 0.98, ['Limits of Strain: ', num2str(St),' to ',num2str(En)])
text(15.25/100,0.97,['B&W Limit = ', num2str(limit)]), grid on

%% Dilatation
DetA = (1+(-Strain_t_new)).*((1+Width_Strain_new).^2)-1;
figure(), h=plot(Strain_t_new,DetA,'.'); set(h,'markersize',8), hold on
Dil = (-Strain_t_new)+2*(Width_Strain_new);
h = plot(Strain_t_new,Dil,'.','color',[ 0.4660    0.6740    0.1880]);
set(h,'markersize',8)
grid on

[D,S] = polyfit(Strain_t_new,DetA,1); D
Dfit = D(1).*Strain_t_new+D(2); plot(Strain_t_new,Dfit,'r')
    yresid=DetA-Dfit;
    SSresid=sum(yresid.^2);
    SStotal=sum((DetA-mean(DetA)).^2);
    r_sq=1-(SSresid/SStotal)
ylim=get(gca,'ylim'); xlim=get(gca,'xlim');
text(0.25/100,0.94,['\bf Linear Regression:']);
text(0.5/100,0.93,['R^2 = ', num2str(r_sq)]);
text(0.5/100,0.92,['Slope = ', num2str(D(1))])
text(0.5/100,0.91,['Intercept = ', num2str(D(2))])
text(12.75/100, 0.98, ['Limits of Strain: ', num2str(St),' to ',num2str(En)])
text(15.25/100,0.97,['B&W Limit = ', num2str(limit)])

[D1,S] = polyfit(Strain_t_new,Dil,1); D1
Dfit1 = D1(1).*Strain_t_new+D1(2); plot(Strain_t_new,Dfit1,'r')
    yresid=Dil-Dfit1;
    SSresid=sum(yresid.^2);
    SStotal=sum((Dil-mean(Dil)).^2);
    r_sq=1-(SSresid/SStotal)
ylim=get(gca,'ylim'); xlim=get(gca,'xlim');
text(0.25,0.94,['\bf Linear Regression:']);
text(0.5,0.93,['R^2 = ', num2str(r_sq)]);
text(0.5,0.92,['Slope = ', num2str(D(1))])
text(0.5,0.91,['Intercept = ', num2str(D(2))])
text(12.75, 0.98, ['Limits of Strain: ', num2str(St),' to ',num2str(En)])
text(15.25,0.97,['B&W Limit = ', num2str(limit)])
legend('Higher Order','First Order Approximation','Linear Regression')
xlabel('Compressive Strain'), ylabel('Unit Volume Change')
```

6.3 Differential Scanning Calorimetry Thermograms of IC1000 Pad Samples

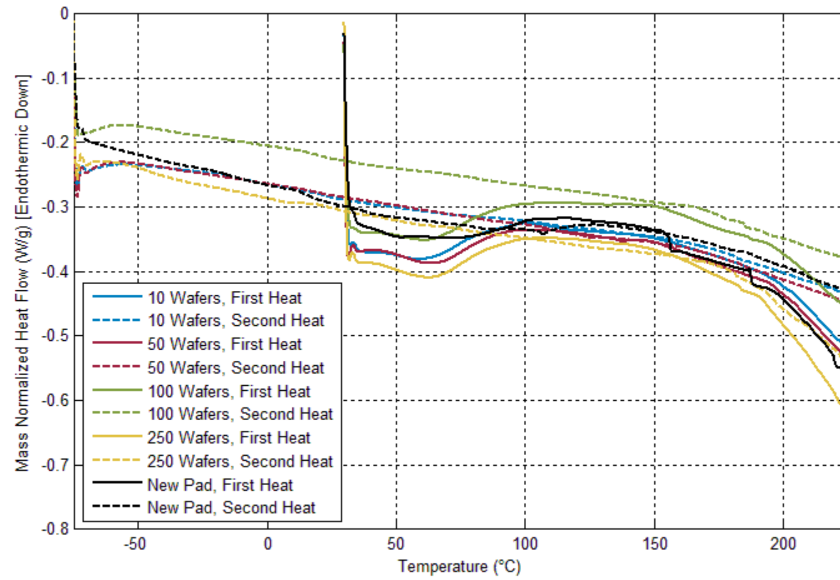

Figure 75: Calorimetry Results from Copper Wafer, High Pressure, Low Velocity Pad Samples with New Pad Results of Trial 1

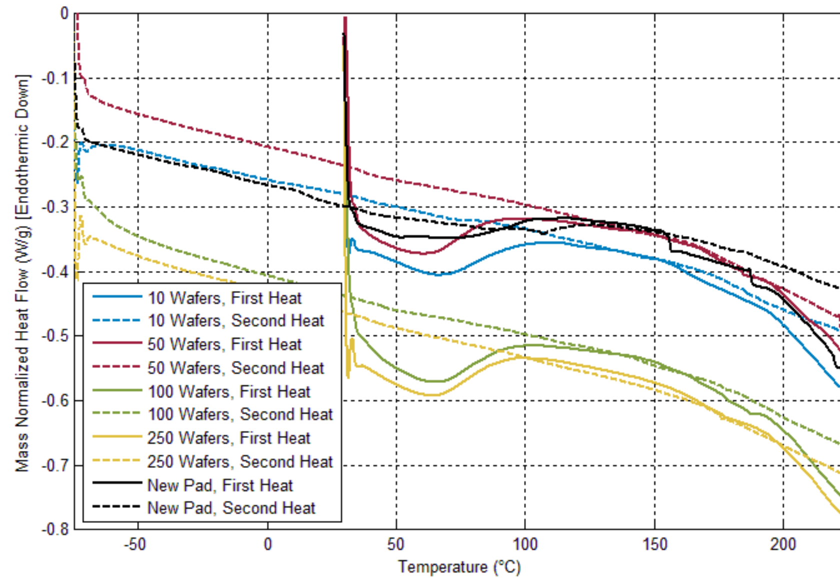

Figure 76: Calorimetry Results from Copper Wafer, Low Pressure, High Velocity Pad Samples with New Pad Results of Trial 1

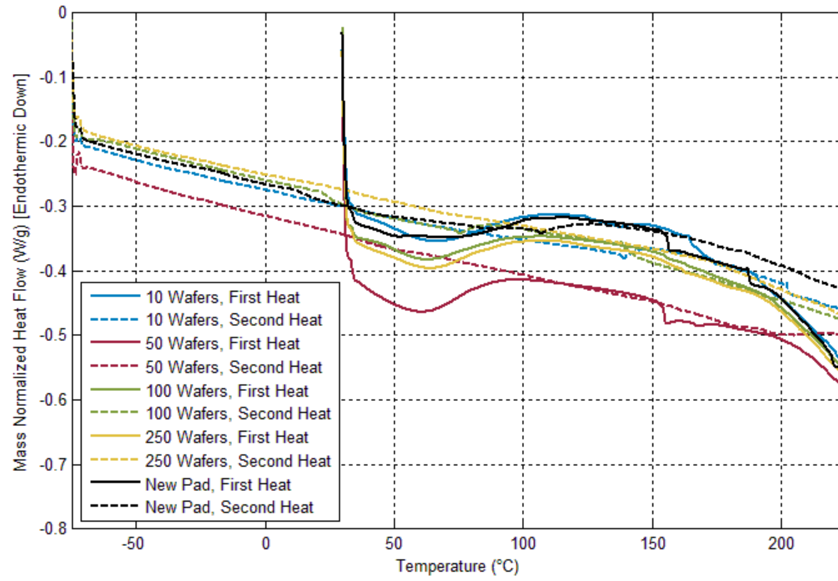

Figure 77: Calorimetry Results from Copper Wafer, Low Pressure, Low Velocity Pad Samples with New Pad Results of Trial 1

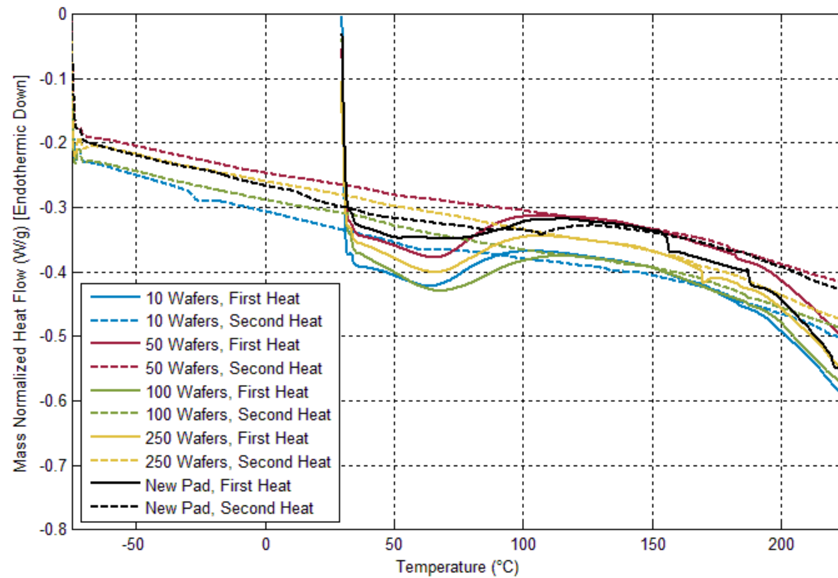

Figure 78: Calorimetry Results from Silicon Dioxide Wafer, High Pressure, Low Velocity Pad Samples with New Pad Results of Trial 1

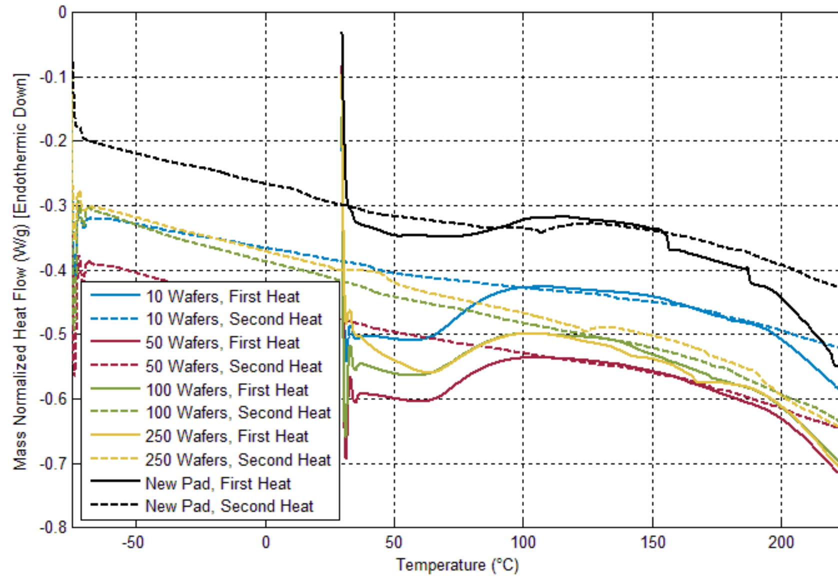

Figure 79: Calorimetry Results from Silicon Dioxide Wafer, Low Pressure, High Velocity Pad Samples with New Pad Results of Trial 1

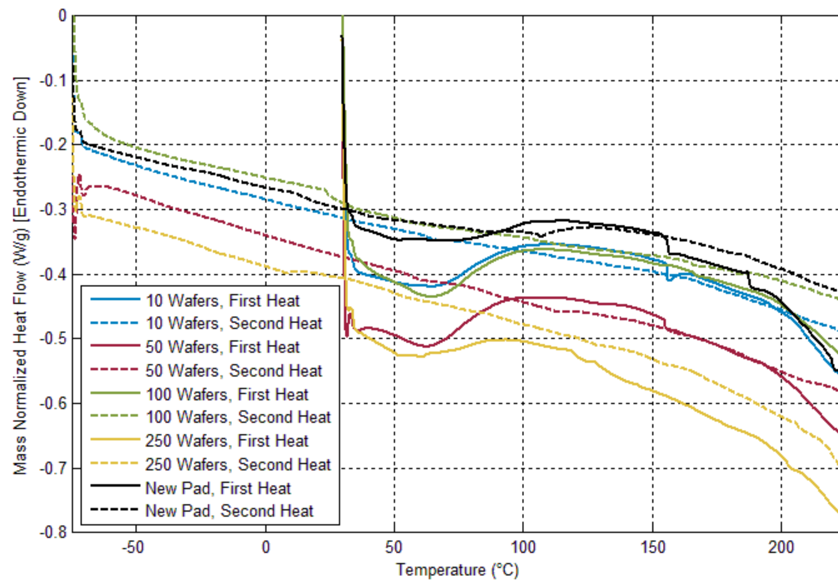

Figure 80: Calorimetry Results from Silicon Dioxide Wafer, Low Pressure, Low Velocity Pad Samples with New Pad Results of Trial 1

BIBLIOGRAPHY

Ahmadi, G. and X. Xia. 2001. "A Model for Mechanical Wear and Abrasive Particle Adhesion during the Chemical Mechanical Polishing Process." *Journal of the Electrochemical Society* 148 (3): G99-G109.

Anbarasi, M. S., S. Ghaayathri, R. Kamaleswari, and I. Abirami. 2011. "Outlier Detection for Multidimensional Medical Data." *International Journal of Computer Science and Information Technologies* 2 (1): 512-516.

Armini, S., C. M. Whelan, K. Maex, J. L. Hernandez, and M. Moinpour. 2007. "Composite Polymer-Core Silica-Shell Abrasive Particles during Oxide CMP." *Journal of the Electrochemical Society* 154 (8): H667-H671.

ASTM. 2001. *Standard Test Methods for Tensile, Compressive, and Flexural Creep and Creep-Rupture of Plastics*. West Conshohocken: ASTM International.

Atanasova, T. A., L. Carbonell, R. Caluwaerts, Zs Tokei, K. Strubbe, and P. M. Vereecken. 2013. "Ultra-Low Copper Baths for Sub-35 Nm Copper Interconnects." *Journal of the Electrochemical Society* 160 (12): D3255-D3259.

Atkins, A. G. and Y. W. Mai. 1985. "Elastic and Plastic Fracture." Chap. A2, In *Elastic and Plastic Fracture*, 798. West Sussex, England: Ellis Horwood Limited.

Bajaj, Rajeev, Rahul Jairath, Matthew Stell, and Robert Tolles. 1994. "Effect of Polishing Pad Material Properties on Chemical Mechanical Polishing (CMP) Processes." *MRS Proceedings* 337: 637-644.

Balakumar, S., T. Haque, A. Kumar, M. Rahman, and R. Kumar. 2005. "Wear Phenomena in Abrasive-Free Copper CMP Process." *Journal of the Electrochemical Society* 152 (11): G867-G874.

Banerjee, Gautam and Robert L. Rhoades. 2008. "Chemical Mechanical Planarization Historical Review and Future Direction." *ECS Transactions* 13 (4): 1-19.

Bastaninejad, M. and G. Ahmadi. 2005. "Modeling the Effects of Abrasive Size Distribution, Adhesion, and Surface Plastic Deformation on Chemical-Mechanical Polishing." *Journal of the Electrochemical Society* 152 (9): G720-G730.

Bastawros, A., A. Chandra, Y. Guo, and B. Yan. 2002. "Pad Effects on Material-Removal Rate in Chemical-Mechanical Planarization." *Journal of Electronic Materials* 31 (10): 1022-1031.

Bhushan, B. 2002. *Introduction to Tribology*. New York: John Wiley & Sons, Inc.

Borucki, L. 2002. "Mathematical Modeling of Polish-Rate Decay in Chemical-Mechanical Polishing." *Journal of Engineering Mathematics* 43 (2): 105-114.

Boyer, H. E., ed. 1987. *Atlas of Stress-Strain Curves*. Metals Park, Ohio: ASM International.

Bozkaya, Diner and Sinan Muftu. 2009. "A Material Removal Model for CMP Based on the Contact Mechanics of Pad, Abrasives, and Wafer." *Journal of the Electrochemical Society* 156 (12): H890-H902.

Brandes, E. A. and G. B. Brook. 1992. "Smithells Metals Reference Book." Chap. 14.4, In *Smithells Metals Reference Book*, 14-6. Oxford, UK: Butterworth-Heinemann.

Brown, M. E., ed. 1998. *Handbook of Thermal Analysis and Calorimetry. Volume 1: Principles and Practice*. Amsterdam, The Netherlands: Elsevier Science B.V.

Buckingham, E. 1916. "Model Experiments and the Forms of Empirical Equations."ASME, .

Budynas, R. and J. Nisbett. 2011. Chap. A-5, In *Shigley's Mechanical Engineering Design*, 1007. New York, NY: McGraw-Hill.

Cao, Z. and X. Zhang. 2008. "Nanoindentation Stress-Strain Curves of Plasma-Enhanced Chemical Vapor Deposited Silicon Oxide Thin Films." *Thin Solid Films* 516 (8): 1941-1951.

Carlotti, G., L. Doucet, and M. Dupeux. 1997. "Elastic Properties of Silicon Dioxide Films Deposited by Chemical Vapour Deposition from Tetraethylorthosilicate." *Thin Solid Films* 296 (1): 102-105.

Castillo-Mejia, D., S. Gold, V. Burrows, and S. Beaudoin. 2003. "The Effect of Interactions between Water and Polishing Pads on Chemical Mechanical Polishing Removal Rates." *Journal of the Electrochemical Society* 150 (2): G76-G82.

Chandra, A., P. Karra, A. Bastawros, R. Biswas, P. Sherman, S. Armini, and D. Lucca. 2008. "Prediction of Scratch Generation in Chemical Mechanical Planarization." *CIRP Annals* 57 (1): 559-562.

Chandra, Abhijit, Pavan K. Karra, and Ashraf F. Bastawros. 2010. "Defectivity Avoidance in Chemical Mechanical Planarization: Role of Multi-Scale and Multi-Physics Interactions." *ECS Transactions* 33 (10): 9-20.

Chandrasekaran, N., S. Ramarajan, W. Lee, G. M. Sabde, and S. Meikle. 2004. "Effects of CMP Process Conditions on Defect Generation in Low-k Materials an Atomic Force Microscopy Study." *Journal of the Electrochemical Society* 151 (12): G882-G889.

Charns, L. 2005. "Mechanical Properties of Chemical Mechanical Polishing Pads Containing Water-Soluble Particles." *Thin Solid Films* 485 (1): 188-193.

Choi, Jae-Gon, Nagendra Prasad, In-Kwon Kim, In-Gon Kim, Woo-Jin Kim, Ahmed Busnaina, and Jin-Goo Park. 2010. "Analysis of Scratches Formed on Oxide Surface during Chemical Mechanical Planarization." *Journal of the Electrochemical Society* 157 (2): H186-H191.

Choi, Jae-Gon, Y. Nagendra Prasad, In-Kwon Kim, Woo-Jin Kim, and Jin-Goo Park. 2010. "The Synergetic Role of Pores and Grooves of the Pad on the Scratch Formation during STI CMP." *Journal of the Electrochemical Society* 157 (8): H806-H809.

Derjaguin, B., V. Muller, and YU Toporov. 1975. *Effect of Contact Deformations on the Adhesion of Particles*. Moscow: Department of Surface Phenomena, Institute of Physical Chemistry, Academy of Sciences.

Deshpande, S., S. Dakshinamurthy, S. C. Kuiry, R. Vaidyanathan, Y. S. Obeng, and S. Seal. 2005. "Surface-Modified Polymeric Pads for Enhanced Performance during Chemical Mechanical Planarization." *Thin Solid Films* 483 (1): 261-9.

Dickie, B. D. 1997. "Investigation of an Engineering Thermoplastic Polyurethane by MDSC." *Thermochimica Acta* 305: 347-352.

Dill, K. and S. Bromberg. 2003. "Molecular Driving Forces: Statistical Thermodynamics in Chemistry and Biology." Chap. 7,8, In *Molecular Driving Forces: Statistical Thermodynamics in Chemistry and Biology*, 105-152. New York, NY: Garland Science.

Dubreuil, O., V. Caubet-Hilloutou, J. Guillan, K. Haxaire, M. Mellier, P. Caubet, P. Vannier, E. Petitprez, D. Bellet, and Ph Normandon. 2010. "Characterization and Impact of Reduced Copper Plating Overburden on 45 Nm Interconnect Performances." *Microelectronic Engineering* 87 (3): 421-425.

Eusner, T., N. Saka, and J-H Chun. 2011. "Breaking-in a Pad for Scratch-Free, Cu Chemical-Mechanical Polishing." *Journal of the Electrochemical Society* 158 (4): H379-H389.

Eusner, T., N. Saka, and J-H Chun. 2010. *Defect Reduction in Cu Chemical-Mechanical Polishing*. Cambridge, MA: Massachusetts Institute of Technology.

Eusner, T., N. Saka, and J-H Chun. 2010. "Tribological Defects in Planar Nanomanufacturing Processes." *International Journal of Nanomanufacturing* 6 (1): 22-37.

Eusner, T., N. Saka, J-H Chun, S. Armini, M. Moinpour, and P. Fischer. 2009. "Controlling Scratching in Cu Chemical Mechanical Planarization." *Journal of the Electrochemical Society* 156 (7): H528-H534.

Fan, W., D. Bonding, L. Charns, H. Miyauchi, H. Tano, and S. Tsuji. 2010. "Study on Stiffness and Conditioning Effects of CMP Pad Based on Physical Die-Level CMP Model." *Journal of the Electrochemical Society* 157 (5): H526-H533.

Fu, G., A. Chandra, S. Guha, and G. Subhash. 2001. "A Plasticity-Based Model of Material Removal in Chemical-Mechanical Polishing (CMP)." *IEEE Transactions on Semiconductor Manufacturing* 14 (4): 406-417.

Ghosh, S. and R. Prakash. 2013. "Study of Damage and Fracture Toughness due to Influence of Creep and Fatigue of Commercially Pure Copper by Monotonic and Cyclic Indentation." *Metallurgical and Materials Transactions.A, Physical Metallurgy and Materials Science* 44 (1): 224-34.

Gianola, D. S. and W. N. Sharpe Jr. 2004. "Techniques for Testing Thin Films in Tension." *Experimental Techniques (Westport, Conn.)* 28 (5): 23-27.

Green, A. E. and P. M. Naghdi. 1965. "A General Theory of an Elastic-Plastic Continuum." *Archive for Rational Mechanics and Analysis* 18 (4): 251.

Hamilton, G. M. 1983. "Explicity Equations for the Stresses Beneath a Sliding Spherical Contact." *Institution of Mechanical Engineers* 197: 53-59.

Hamilton, G. M. and L. E. Goodman. 1966. "The Stress Field Created by a Circular Sliding Contact." *Journal of Applied Mechanics* 33 (2): 371.

Han, Ja-Hyung, Sang-Rok Hah, Young-Jae Kang, and Jin-Goo Park. 2007. "Effect of Polish by-Products on Copper Chemical Mechanical Polishing Behavior." *Journal of the Electrochemical Society* 154 (6): H525-H529.

Hiller, D., R. Zierold, J. Bachmann, M. Alexe, Y. Yang, J. W. Gerlach, A. Stesmans, et al. 2010. "Low Temperature Silicon Dioxide by Thermal Atomic Layer Deposition: Investigation of Material Properties." *Journal of Applied Physics* 107 (6): 064314; 064314.

Huey, S., S. Mear, Y. Wang, R. Jin, J. Ceresi, P. Freeman, D. Johnson, T. Vo, and S. Eppert. 1999. "Technological Breakthrough in Pad Life Improvement and its Impact on CMP CoC." *Advanced Semiconductor Manufacturing Conference and Workshop, 1999 IEEE/SEMI*: 54 - 58.

Ihnfeldt, Robin and Jan B. Talbot. 2006. "The Effects of Copper CMP Slurry Chemistry on the Colloidal Behavior of Alumina Abrasives." *Journal of the Electrochemical Society* 153 (11): G948-G955.

Intel. "Intel®300 mm Wafer with 45 Nm Shuttle Test Chips." Intel.com., last modified 1/25/2006, accessed 1/22, /2015, http://www.intel.com/pressroom/archive/releases/2006/20060125comp.htm.

ITRS. 2013. *International Technology Roadmap for Semiconductors: 2013 Edition, Executive Summary*: International Technology Roadmap for Semiconductors.

Jairath, Rahul, Mukesh Desai, Matt Stell, and Robert Tolles. 1994. "Consumables for the Chemical Mechanical Polishing (CMP) of Dielectrics and Conductors." *MRS Proceedings* 337: 121-131.

Jiao, Y., Y. Sampurno, Y. Zhuang, X. Wei, A. Meled, and A. Philipossian. 2011. "Tribological, Thermal, and Kinetic Characterization of 300-mm Copper Chemical Mechanical Planarization Process." *Japanese Journal of Applied Physics* 50 (5).

Johnson, K., K. Kendall, and D. Roberts. 1971. "Surface Energy and the Contact of Elastic Solids." *Proceedings of the Royal Society of London* 324 (1558): 301-313.

Joo, S. and H. Liang. 2013. "In Situ Characterization of Triboelectrochemical Effects on Topography of Patterned Copper Surfaces." *Journal of Electronic Materials* 42 (6): 979-987.

Ju, Y. S. and K. E. Goodson. 1999. "Process-Dependent Thermal Transport Properties of Silicon-Dioxide Films Deposited using Low-Pressure Chemical Vapor Deposition." *Journal of Applied Physics* 85 (10): 7130-7134.

Kakireddy, Veera Raghava. 2008. "Effect of Temperature on Copper Damascene Chemical Mechanical Polishing Process." *Journal of Vacuum Science & Technology.B, Microelectronics and Nanometer Structures Processing, Measurement and Phenomena* 26 (1): 141-150.

Kim, B. S., M. H. Tucker, J. D. Kelchner, and S. P. Beaudoin. 2008. "Study on the Mechanical Properties of CMP Pads." *IEEE Transactions on Semiconductor Manufacturing* 21 (3): 454-463.

Kim, Ho-youn, Hyoung-jae Kim, and Hae-do Jeong. 2000. "Development of an Abrasive Embedded Pad for Dishing Reduction and Uniformity Enhancement." *Journal of the Korean Physical Society* 37 (6): 945-951.

Kim, Nam-Hoon, Yong-Jin Seo, and Woo-Sun Lee. 2006. "Temperature Effects of Pad Conditioning Process on Oxide CMP: Polishing Pad, Slurry Characteristics, and Surface Reactions." *Microelectronic Engineering* 83 (2): 362-370.

Kim, S., N. Saka, and J-H Chun. 2011. "The Effects of Mechanical and Tribological Properties of Coatings on Scratch Generation in Chemical-Mechanical Polishing." *ECS Transactions* 41 (7): 393-404.

Kim, S., N. Saka, and J-H Chun. 2014. "Pad Scratching in Chemical-Mechanical Polishing: The Effects of Mechanical and Tribological Properties." *ECS Journal of Solid State Science and Technology* 3 (5): P169-P178.

Kim, S., N. Saka, and J-H Chun. 2014. "The Role of Pad Topography in Chemical-Mechanical Polishing." *IEEE Transactions on Semiconductor Manufacturing* 27 (3): 431-442.

Kim, S., N. Saka, J-H Chun, and S. -H Shin. 2013. "Modeling and Mitigation of Pad Scratching in Chemical-Mechanical Polishing." *CIRP Annals* 62 (1): 307-310.

Kinloch, A. J. 1987. Chap. 2, In *Adhesion and Adhesives*, 18. London and New York: Chapman and Hall.

Krishnan, Mahadevaiyer, Jakub Nalaskowski, and Lee Cook. 2010. "Chemical Mechanical Planarization: Slurry Chemistry, Materials, and Mechanisms." *Chemical Reviews* 110 (1): 178-204.

Kwon, Tae-Young, Byoung-Jun Cho, Manivannan Ramachandran, Ahmed Busnaina, and Jin-Goo Park. 2013. "Investigation of Source-Based Scratch Formation during Oxide Chemical Mechanical Planarization." *Tribology Letters* 50 (2): 169-175.

Lai, W. M., D. Rubin, and E. Krempl. 2010. *Introduction to Continuum Mechanics*. Burlington, MA: Elsevier.

Lay, N. and D. J. Duquette. 2006. "The Evolution of Surface Roughness of Copper Electrodeposition Directly on Ultra-Thin Air Exposed TaN Layers."The Electrochemical Society, .

Lee, H., S. Suh, S. Kim, S. Park, and Y. Joo. 2009. "Measurement of Poisson's Ratio of a Thin Film on a Substrate by Combining X-Ray Diffraction with in Situ Substrate Bending." *Electronic Materials Letters* 5 (1): 51-54.

Lee, Jung H., D. S. Kim, and Y. H. Lee. 1996. "Room Temperature Deposition of Silicon Dioxide Films by Ion-Assisted Plasma Enhanced Chemical Vapor Deposition." *Journal of the Electrochemical Society* 143 (4): 1443-1451.

Leonard, I. E., J. E. Lewis, A. C. Liu, and G. W. Tokarsky. 2014. Chap. 5.3, In *Classical Geometry. Euclidean, Transformational, Inversive, and Projective*, 152. Hoboken, New Jersey: John Wiley & Sons, Inc.

Li, I., K. Forsthoefel, K. Richardson, Y. Obeng, W. Easter, and A. Maury. 2000. "Dynamic Mechanical Analysis (DMA) of CMP Pad Materials." *MRS Proceedings* 613: E7-E7.

Li, Weidan, Dong Wook Shin, Minoru Tomozawa, and Shyam P. Murarka. 1995. "Effect of the Polishing Pad Treatments on the Chemical-Mechanical Polishing of SiO2 Films." *Thin Solid Films* 270 (1): 601-606.

Li, Yuzhuo, ed. 2008. *Microelectric Applications of Chemical Mechanical Planarization*, edited by Yuzhuo Li. Hoboken, New Jersey: John Wiley & Sons, Inc.

Lim, J., N. Johari, S. Rustagi, and N. Arora. 2014. "Characterization of Interconnect Process Variation in CMOS using Electrical Measurements and Field Solver." *IEEE Transactions on Electron Devices* 61 (5): 1255-1261.

Lin, Yeou-Yih, Ding-Yeng Chen, and Chuang Ma. 2009. "Simulations of a Stress and Contact Model in a Chemical Mechanical Polishing Process." *Thin Solid Films* 517 (21): 6027-6033.

Lu, H., Y. Obeng, and K. Richardson. 2002. "Applicability of Dynamic Mechanical Analysis for CMP Polyurethane Pad Studies." *Materials Characterization* 49 (2): 177-186.

Lucas, J. P. 1995. "Determining Fracture Toughness of Vitreous Silica Glass." *Scripta Metallurgica Et Materialia* 32 (5): 743-8.

Ludwig, Christian and Humberto Chaves. 2011. "A New Measurement System to Determine Material Properties of Polishing Pads." *Journal of Electronic Materials* 40 (11): 2264-2267.

Luo, J. and D. Dornfeld. 2001. "Material Removal Mechanism in Chemical Mechanical Polishing: Theory and Modeling." *IEEE Transactions on Semiconductor Manufacturing* 14 (2): 112-133.

Luo, J. and D. Dornfeld. 2003. "Material Removal Regions in Chemical Mechanical Planarization for Submicron Integrated Circuit Fabrication: Coupling Effects of Slurry Chemicals, Abrasive Size Distribution, and Wafer-Pad Contact Area." *IEEE Transactions on Semiconductor Manufacturing* 16 (1): 45-56.

Mack, Chris A. 2011. "Fifty Years of Moore's Law." *IEEE Transactions on Semiconductor Manufacturing* 24 (2): 202-207.

Matta, C., L. Massa, A. Gubskaya, and E. Knoll. 2011. "Can One Take the Logarithm Or the Sine of a Dimensioned Quantity Or a Unit? Dimensional Analysis Involving Transcendental Functions." *Journal of Chemical Education* 88 (1): 67-70.

Maugin, G. A. 1992. "The Thermomechanics of Plasticity and Fracture." Chap. 2.3, In *The Thermomechanics of Plasticity and Fracture*, 38. New York: Cambridge University Press.

Moinpour, M., A. Tregub, A. Oehler, and K. Cadien. 2002. *Advances in Characterization of CMP Consumables*. Vol. 27.

Murarka, Shyam P., Joseph M. Steigerwald, and Ronald J. Gutmann . 1993. "Inlaid Copper Multilevel Interconnections using Planarization by Chemical-Mechanical Polishing." *MRS Bulletin* 18 (06): 46.

Nasrullah, J., G. Tyler, and Y. Nishi. 2005. "An Atomic Force Microscope Study of Surface Roughness of Thin Silicon Films Deposited on SiO2." *IEEE Transactions on Nanotechnology* 4 (3): 303-311.

Prasad, Y. Nagendra, Tae-Young Kwon, In-Kwon Kim, In-Gon Kim, and Jin-Goo Park. 2011. "Generation of Pad Debris during Oxide CMP Process and its Role in Scratch Formation." *Journal of the Electrochemical Society* 158 (4): H394-H400.

Qin, Kuide, Brij Moudgil, and Chang-Won Park. 2004. "A Chemical Mechanical Polishing Model Incorporating both the Chemical and Mechanical Effects." *Thin Solid Films* 446 (2): 277-286.

Ring, Terry A., Paul Feeney, David Boldridge, Jaishankar Kasthurirangan, Shoutian Li, and James A. Dirksen. 2007. "Brittle and Ductile Fracture Mechanics Analysis of Surface Damage Caused during CMP." *Journal of the Electrochemical Society* 154 (3): H239-H248.

Rittel, D., G. Ravichandran, and S. Lee. 2002. "Large Strain Constitutive Behavior of OFHC Copper Over a Wide Range of Strain Rates using the Shear Compression Specimen." *Mechanics of Materials* 34 (10): 627-642.

Runnels, S. R., F. Miceli, and I. Kim. 1999. "Validation of a Large Area Three-Dimensional Erosion Simulator for Chemical Mechanical Polishing." *Journal of the Electrochemical Society* 146 (12): 4619-4625.

Sadd, M. H. 2009. *Elasticity: Theory, Applications, and Numerics*. Burlington, MA: Academic Press.

Saka, N. 2001. "Mechanisms of the Chemical Mechanical Polishing (CMP) Process in Integrated Circuit Fabrication." *CIRP Annals* 50 (1): 233-238.

Saka, N., T. Eusner, and J-H Chun. 2008. "Nano-Scale Scratching in Chemical-Mechanical Polishing." *CIRP Annals* 57 (1): 341-344.

Saka, N., T. Eusner, and J-H Chun. 2010. "Scratching by Pad Asperities in Chemical-Mechanical Polishing." *CIRP Annals* 59 (1): 329-332.

Schawe, J., Riesen, R., Widmann, J., M. Schubnell, and U. Jorimann. 2000. *Interpreting DSC Curves*. Schwerzenbach: Mettler Toledo.

Seok, Jongwon, Cyriaque Sukam, Andrew T. Kim, John Tichy, and Timothy Cale. 2004. "Material Removal Model for Chemical-Mechanical Polishing Considering Wafer Flexibility and Edge Effects." *Wear* 257 (5): 496-508.

Seok, Jongwon, Cyriaque Sukam, Andrew T. Kim, John Tichy, and Timothy Cale. 2003. "Multiscale Material Removal Modeling of Chemical Mechanical Polishing." *Wear* 254 (3): 307-320.

Shackelford, J. and W. Alexander. 2001. Chap. 5, In *Materials Science and Engineering Handbook*, 375. Boca Raton: CRC Press LLC.

Shan, Lei, Joseph Levert, Lorne Meade, John Tichy, and Steven Danyluk. 2000. "Interfacial Fluid Mechanics and Pressure Prediction in Chemical Mechanical Polishing." *Journal of Tribology* 122 (3): 539-543.

Sharpe Jr., W. N., J. Pulskamp, D. S. Gianola, C. Eberl, R. G. Polcawich, and R. J. Thompson. 2007. "Strain Measurements of Silicon Dioxide Microspecimens by Digital Imaging Processing." *Experimental Mechanics* 47 (5): 649-658.

Srinivasa-Murthy, C., D. Wang, S. Beaudoin, T. Bibby, K. Holland, and T. Cale. 1997. "Stress Distribution in Chemical Mechanical Polishing." *Thin Solid Films* 308: 533-537.

Steigerwald, J. M., S. P. Murarka, R. J. Gutmann, and D. J. Duquette. 1995. "Chemical Processes in the Chemical Mechanical Polishing of Copper." *Materials Chemistry and Physics* 41 (3): 217-217.

Steigerwald, Joseph M., Shyam P. Murarka, and Ronald J. Gutmann . 1997. *Chemical-Mechanical Planarization of Microelectronic Materials*. Canada: John Wiley & Sons, Inc.

Stroud, K. A. and D. J. Booth. 2001. *Engineering Mathematics*. 5th ed. New York, NY: Industrial Press, Inc.

Sumigawa, T., T. Shishido, T. Murakami, T. Iwasaki, and T. Kitamura. 2010. "Evaluation on Plastic Deformation Property of Copper Nano-Film by Nano-Scale Cantilever Specimen." *Thin Solid Films* 518 (21): 6040-6047.

Sung, In-Ha, Hong Jim Kim, and Chang Dong Yeo. 2012. "First Observation on the Feasibility of Scratch Formation by Pad-Particle Mixture in CMP Process." *Applied Surface Science* 258 (20): 8298-8306.

Teo, T. Y., W. L. Goh, V. Lim, L. S. Leong, T. Y. Tse, and L. Chan. 2004. "Characterization of Scratches Generated by a Multiplaten Copper Chemical-Mechanical Polishing Process." *Journal of Vacuum Science & Technology.B, Microelectronics and Nanometer Structures Processing, Measurement and Phenomena* 22 (1): 65-69.

Thagella, Swetha. 2004. "Tribological Issues and Modeling of Removal Rate of Low-k Films in CMP." *Journal of the Electrochemical Society* 151 (3): G205-G215.

Thomas, L. *Interpreting Unexpected Events and Transitions in DSC Results*. New Castle, Deleware: TA Instruments.

Tichy, John, Joseph A. Levert, Lei Shan, and Steven Danyluk. 1999. "Contact Mechanics and Lubrication Hydrodynamics of Chemical Mechanical Polishing." *Journal of the Electrochemical Society* 146 (4): 1523-1528.

Timoney, Pádraig, Eamonn Ahearne, and Gerald Byrne. 2010. "Contact Pressure Distribution in the Chemical Mechanical Planarization of 450mm Wafers." *MRS Proceedings* 1249: 155-160.

Tregub, A. 2003. "Pad Degradation during CMP Pr.6ocess: Effect of Soak in Slurry and Water on Thermal and Mechanical Properties of the CMP Pads." *MRS Proceedings* 767: 101-110.

Tsai, H. and W. Fang. 2003. "Determining the Poisson's Ratio of Thin Film Materials using Resonant Method." *Sensors and Actuators.A.Physical.* 103 (3): 377-383.

Tseng, Wei-Tsu, Yiao-Hsien Wang, and Jyh-Hwa Chin. 1999. "Effects of Film Stress on the Chemical Mechanical Polishing Process." *Journal of the Electrochemical Society* 146 (11): 4273-4280.

Volinsky, A. A., J. Vella, I. S. Adhihetty, V. Sarihan, L. Mercado, B. H. Yeung, and W. W. Gerberich. 2001. "Microstructure and Mechanical Properties of Electroplated Cu Thin Films." *MRS Proceedings* 649 (Fundamentals of Nanoindentation and Nanotribology II. Symposium): Q5.

Wang, C., P. Sherman, A. Chandra, and D. Dornfeld. 2005. "Pad Surface Roughness and Slurry Particle Size Distribution Effects on Material Removal Rate in Chemical Mechanical Planarization." *CIRP Annals* 54 (1): 309-312.

Wang, D., J. Lee, K. Holland, T. Bibby, S. Beaudoin, and T. Cale. 1997. "Von Mises Stress in Chemical-Mechanical Polishing Processes." *Journal of the Electrochemical Society* 144 (3): 1121-1127.

Wang, T., L. Xinchun, Z. Dewen, and H. Yongyong. 2013. "Contact Stress Non-Uniformity of Wafer Surface for Multi-Zone Chemical Mechanical Polishing Process." *Science China: Technological Sciences* 56 (8): 1974-1979.

Webb, E., C. Gack, and J. Reid. 2004. "Surface Roughness Evolution during the Initial Stages of Electroplating for Copper Interconnect Metallization." *Electrochemical Society Proceedings* PV 2004-17: 82-95.

Wei, X., D. Lee, S. Shim, X. Chen, and J. Kysar. 2007. "Plane-Strain Bulge Test for Nanocrystalline Copper Thin Films." *Scripta Materialia* 57 (6): 541-544.

White, F. 2011. Chap. A, In *Fluid Mechanics*, 826. New York, NY: McGraw-Hill.

Wu, Lixiao. 2009. "Effects of Wafer Curvature Caused by Film Stress on the Chemical Mechanical Polishing Process." *International Journal of Advanced Manufacturing Technology* 40 (9): 929-939.

Xiang, Y., T. Y. Tsui, and J. J. Vlassak. 2006. "The Mechanical Properties of Freestanding Electroplated Cu Thin Films." *Journal of Materials Research* 21 (6): 1607-1618.

Yanda, Richard, Michael Heynes, and Anne Miller. 2005. "Demystifying Chipmaking." .

Yang, J. C., Oh. D. W., H. J. Kim, and T. Kim. 2010. "Investigation on Surface Hardening of Polyurethane Pads during Chemical Mechanical Polishing (CMP)." *Journal of Electronic Materials* 39 (3): 338-346.

Zantye, P., A. K. Sikder, A. Kumar, A. Belyaev, and I. Tarasov. 2003. "Evaluation of Mechanical Quality of CMP Pads using Acoustic Techniques." *Proceedings - Electrochemical Society* 21: 183-190.

Zhang, S., M. Sakane, T. Nagasawa, and K. Kobayashi. 2011. "Mechanical Properties of Copper Thin Films used in Electronic Devices."Elsevier, .

Zhang, Zefang, Weili Liu, and Zhitang Song. 2010. "Particle Size and Surfactant Effects on Chemical Mechanical Polishing of Glass using Silica-Based Slurry." *Applied Optics (2004)* 49 (28): 5480-5485.